Universidade de São Paulo
Instituto de Física

Detector de nêutrons térmicos baseado em GEM com deposição de $^{10}B_4C$ sobre cátodo de alumínio

Lucas de Arruda Serra Filho

Orientador: Prof. Dr. Marco Bregant
Coorientador: Dr. Francisco de Assis Souza

Dissertação de mestrado apresentada ao Instituto de Física da Universidade de São Paulo, como requisito parcial para a obtenção do título de Mestre em Ciências.

Banca Examinadora:
Prof. Dr. Marco Bregant (Orientador) - IFUSP
Prof. Dr. Frederico Antonio Genezini - IPEN
Prof. Dr. Herman Pessoa Lima Junior - CBPF

São Paulo
2021

FICHA CATALOGRÁFICA
Preparada pelo Serviço de Biblioteca e Informação
do Instituto de Física da Universidade de São Paulo

Serra Filho, Lucas de Arruda

Detector de nêutrons térmicos baseado em GEM com deposição de $^{10}B_4C$ sobre cátodo de alumínio. São Paulo, 2022.

Dissertação (Mestrado) – Universidade de São Paulo. Instituto de Física. Depto. de Física Nuclear.

Orientador: Prof. Dr. Marcos Bregant

Área de Concentração: Instrumentação em Física Nuclear

Unitermos: 1. Nêutrons; 2. Física nuclear; 3. Instrumentação (Física); 4. Física experimental.

USP/IF/SBI-017/2022

University of São Paulo
Institute of Physics

GEM-based thermal neutron detector with $^{10}B_4C$ deposition on aluminum cathode

Lucas de Arruda Serra Filho

Supervisor: Prof. Dr. Marco Bregant
Co-supervisor: Dr. Francisco de Assis Souza

Dissertation submitted to the Physics Institute of the University of São Paulo in partial fulfillment of the requirements for the degree of Master of Science.

Examining Committee:
Prof. Dr. Marco Bregant (Supervisor) - IFUSP
Prof. Dr. Frederico Antonio Genezini - IPEN
Prof. Dr. Herman Pessoa Lima Junior - CBPF

São Paulo
2021

Às minhas avós Maria Elza e Suely Maria

Agradecimentos

Várias pessoas e entidades deram essenciais contribuições para a realização deste trabalho. Gostaria de agradecer:

À minha família, meu pai Lucas, minha mãe Luciana, meu irmão Vítor e especialmente às minhas avós Maria Elza e Suely, pelo apoio incondicional em todos os momentos, sem o qual eu jamais teria conseguido.

À Ana Fontenelle pelo apoio incondicional, pelas contribuições valiosas relacionadas à vida acadêmica e à vida em si, e pela amizade e paciência sem as quais eu jamais teria chegado até aqui.

Ao meu grande amigo Caíke, também membro do grupo de café mais seleto do Brasil, exímio programador e colecionador de canetas e carimbos, que esteve comigo por todo esse percurso desde as remotas épocas do bacharelado.

Ao meu amigo Hugo Natal da Luz, também por várias sugestões valiosas, pelas conversas musicais e pela boa companhia.

À Renata Schneider pela amizade, pelos conselhos, pela paciência e pela companhia sem as quais eu não conseguiria manter a calma e o foco necessários.

Aos meus colegas Geovane Grossi e Renan Felix, pela intensa troca de informações e ótimas sugestões durante o trabalho, além da amizade e companhia.

Ao meu orientador Marco Bregant, pelos ensinamentos, pela paciência nas correções, pelas discussões ricas, construtivas, e pela amizade e companheirismo durante todo esse trabalho.

Ao Francisco Souza, meu coorientador, e ao Maurício Moralles, pelas ricas e longas discussões, por acompanharem a realização das medições e serem sempre super solícitos.

Aos meus colegas de grupo que me aguentaram nas reuniões semanais, Chiara, Thaís e Carlo, e também à Monalisa, Luana e Luis, por além da amizade, proporcionarem um ambiente de trabalho leve e harmonioso.

Aos professores do grupo, Marcelo Munhoz, Tiago Fiorini, Nelson Carlin, Mauro Cosentino e Alexandre Suaide, por todo apoio em diferentes estágios do projeto.

À European Spallation Source (ESS), ao Chung-Chuan Lai e à Carina Höglund pela realização da deposição e todo apoio e solicitude.

À Mariana Marques, pela amizade, constante motivação e ajuda com o inglês, essencial para a composição deste trabalho.

Às pessoas incríveis que conheci na USP, dentre elas o Marcos, Walter, Maurício, Renato e Victor.

Aos colaboradores do Instituto, Néia, Marcos, Gilda, Zenaide, Otávio, Victório, Wellington e Ricardo por serem sempre super solícitos e também viabilizarem as condições necessárias para realização deste trabalho.

Por fim, ao Conselho Nacional de Desenvolvimento Científico e Tecnológico (CNPq), pela financiamento através da bolsa de mestrado (processo: 156767/2019-8).

Resumo

Desde sua descoberta em 1932, nêutrons tiveram um papel essencial no entendimento da física nuclear. Como não interagem por meio de forças elétricas, eles constituem partículas desafiadoras para detecção. Desenvolvimentos cruciais como os realizados por Shull e Brockhouse [1] permitiram usar nêutrons para, além da geração de energia, o estudo de propriedades estáticas e dinâmicas da matéria.

Com a escassez de ^{3}He, o isótopo mais utilizado para detecção de nêutrons, a comunidade científica iniciou a busca por métodos viáveis de detecção de nêutrons, utilizando isótopos alternativos como ^{157}Gd, ^{10}B, e ^{6}Li, que também apresentam alta seção de choque de captura para nêutrons térmicos. Paralelamente, o interesse em ciência de nêutrons tem crescido devido aos diversos avanços nas técnicas de espalhamento, amplamente utilizadas em várias áreas como Química, Física, Biologia e Engenharia. Tais avanços dependem do desenvolvimento de detectores, que também cresceu nos últimos anos, juntamente com a capacidade de se obter feixes de nêutrons monocromáticos tanto em pequenas como grandes instalações.

Para aplicações que requerem grandes áreas e volumes de detecção, os detectores a gás ainda são uma escolha importante. A nova geração de detectores gasosos, os detectores gasosos microestruturados (MPGDs) como o multiplicador gasoso de elétrons (GEM), introduziu novas características, apresentando melhor resolução espacial e de energia, capacidade de operação sob altas taxas de radiação, melhor performance ao longo do tempo e preço competitivo, os tornando amplamente utilizados em vários experimentos.

Este trabalho consistiu em projetar, construir e caracterizar um detector de nêutrons a gás, sensível à posição, que utiliza GEMs. Utilizamos $^{10}B_4C$ como conversor de nêutrons térmicos, depositado sobre o cátodo de alumínio do detector. O protótipo apresentou resolução espacial de pelo menos $3\,\mathrm{mm}$ e $2.66(30)\,\%$ de eficiência de detecção, como calculado pelos modelos teóricos adotados neste trabalho. Também se demonstrou estável para longas aquisições sendo uma alternativa versátil para várias aplicações futuras.

PALAVRAS-CHAVE: detecção de nêutrons, detectores gasosos microestruturados, Gas Electron Multiplier, alternativas ao ^{3}He

Abstract

Since its discovery in 1932, neutrons have had a central role in the understanding of nuclear physics. As they do not interact via electric forces, they constitute a challenging particle to detect. Crucial developments such as the ones by Shull and Brockhouse [1] allowed using neutrons beyond energy generation to study matter's static and dynamic properties.

With the shortage of ^{3}He, the most common isotope used in neutron detection, the scientific community started to pursue viable neutron detection methods using alternative isotopes such as ^{157}Gd, ^{10}B, and ^{6}Li, which also have high neutron capture cross-section. At the same time, the interest in neutron science increased due to the several advances in scattering techniques, widely used in many areas such as chemistry, physics, biology, medicine, and engineering research. These advances depend on detector development which has grown in the last years, together with the ability to obtain bright monochromatic neutron sources, whether in large or small facilities.

For applications that demand high volumes or areas, gaseous detectors are still an important choice. The new generation of the gaseous detectors, the micropattern gaseous detectors (MPGDs), such as the gas electron multiplier (GEM), introduced new features: presenting better spatial and energy resolution, capacity to operate at higher rates, better performance stability over time, and competitive cost making them widely used nowadays in several experiments.

This work consisted of projecting, building, and characterizing a position-sensitive gaseous neutron detector prototype made of GEMs. We used $^{10}B_4C$ as a thermal neutron converter deposited over the aluminum cathode of the detector. It presented at least $3\,\mathrm{mm}$ spatial resolution and $2.66(30)\,\%$ neutron detection efficiency, agreeing with the values evaluated from the theory used in this work. It is also stable for long runs and consists of a versatile alternative for several further applications.

KEYWORDS: neutron detectors, micropattern gaseous detectors, Gas Electron Multiplier, ^{3}He alternative

Contents

Chapter 1

Introduction

The discovery of the neutron by Chadwick in 1932 [2] was central to the development of science in the first half of twenty century. Since neutrons have no electric charge, they do not ionize the medium they travel through, making them complicated to detect. Further significant advancements achieved by Shull and Brockhouse used neutrons for studying the matter and provided the possibility of measuring static or dynamic properties of a given sample that interacts with a neutron beam [3, 4]. Nowadays, modern techniques are being used in an extensive range of applications in different areas such as Physics, Biology, Chemistry, and industry [5–8].

Neutron detectors are key components of neutron scattering instruments, such as diffractometers and spectrometers used in the mentioned applications. Good spatial resolution, high thermal neutron detection efficiency, and low gamma rays sensitivity are among the standard requirements for these detectors. Because of the nature of neutron interaction, several materials are used as neutron converters in those detectors, for instance ^{3}He, ^{10}B, ^{6}Li , ^{157}Gd, and ^{113}Cd. Each of them has its specificity regarding its interaction with the neutrons and the detectable products of this interaction.

Historically, ^{3}He is the most common element for these applications because of its insensitivity to gammas, high neutron capture cross-section, and non-reactivity with other elements. This gas is a subproduct of tritium decay, whose leading suppliers are the United States and Russia [9]. The intense use for scientific research and border security [10] resulted in a shortage of this element [9]. Therefore, the development of new ^{3}He free alternative detectors remains essential for neutron science [11–13].

In the last decades, neutrons have become available on a large scale, with facilities offering higher intensities and different energies from ultra-cold to fast neutrons [14–16]. The growing interest in neutron science has driven the development of different detectors with varying requirements for several applications [17, 18] resulting in the emergence of several kinds of detectors in the last few years [19–23], many of them that still requires

large investments in materials and electronics. However, viable alternatives can be developed to update existing experiments, resulting in better outcomes with a fair investment.

Besides its lower cost compared with solid-state detectors, gaseous detectors are reliable alternatives for several applications, and particularly interesting for large volumes. George Charpak developed a milestone for this kind of detector, being awarded the Nobel prize [24] for the invention of the multiwire proportional chamber [25]. This position-sensitive gaseous detector could cover large areas with a spatial resolution of about one millimeter.

The micropattern gaseous detectors (MPGDs), for instance the Gas electron multiplier (GEM) [26], the Thick-GEM [27], the MICROMEGAS [28], and the MHSP [29], are considered to be the new generation of gaseous detectors. They use modern techniques, including the techniques used on printed circuit boards, to produce small patterned structures that offer the possibility of better controlling the avalanche process as they drift and collection of charges inside the gaseous volume. They present several advantages compared with the classic MWPCs, for example good spatial resolution and energy resolution, the possibility to operate at higher hates, robustness, and effective cost-benefit.

This work aimed to project, build, and characterize a position-sensitive detector using GEMs and $^{10}B_4C$ deposition as a thermal neutron converter. It was necessary to design all the geometric aspects of the prototype based on the physical mechanisms involved in detecting the neutrons and also provide and fine-tune the operational conditions in terms of electrical fields and electronic setup. This project is divided into chapters organized as it follows:

Chapter 2 describes some essential aspects regarding the interaction of radiation with matter, discussing the main effects we expect to observe for different radiations. For this work, charged particles and neutrons are discussed in more detail because of the nature of our detector.

Chapter 3 introduces some concepts about charges transport in the gaseous medium. Here, we also provide an overview of the working principles of the gaseous detectors and the main kind of detectors.

Chapter 4 presents the theoretical framework used to extract results from the measurements. There are three topics discussed: spatial resolution, detection efficiency and geometric calibration. We present the main definitions of the concepts we use to characterize our prototype and some expected values for each of them.

Chapter 5 describes in detail the prototype. We present its physical specifications and discuss signal acquirement, the electronic system, the reactor, and the measurements setup.

Chapter 6 presents an initial set of considerations and expected results from simula-

tions, followed by the experimental results obtained and their discussion. Here, all of the previous chapters are used as fundamental elements.

Finally, Chapter 7 presents the final considerations of this work, discussing its findings and offering a collection of other additional applications.

Chapter 2

Radiation interaction with matter

The first step in developing this work was to understand how radiation interacts with matter. The foundations of radiation detectors are the interaction between matter and radiation since it is just measurable due to these interactions. We can divide all the possible interactions into three groups: by charged particles, by photons, and by neutrons.

A global aspect of the interaction between radiation and matter is that the phenomena are usually energy-dependent, which means that the main way of interaction, the most common process taking place in the detector, varies with the energy of the radiation. Quantifying these processes regarding their importance is an essential requirement for constructing any radiation detecting device.

2.1 Photon interactions

Photons interact with matter with a very particular way, since they have no electric charge. Several process can take place when interacting with matter but the main three are the photoelectric effect, the Comptom scaterring and the pair production. It is important to note that the interaction process is stochastic, thus in different situations is vital the statistical approach. Another remarkable fact about photons is that the interaction is always punctual, which means that the photon needs to die in order to interact. The scattering of a photon, or even its reemission consists on the creation of another photon with same or different energy. It is a very different process regarding what happens with charged particles, which brakes throughout their path, as we will further discuss.

As we mentioned, the probability of a given interaction occuring depends on the incoming radiation energy, as we can see in Fig. 2.1, where the cross sections of different processes of photon interaction in lead are presented. In the further sections we will discuss in more detail these interaction mechanisms.

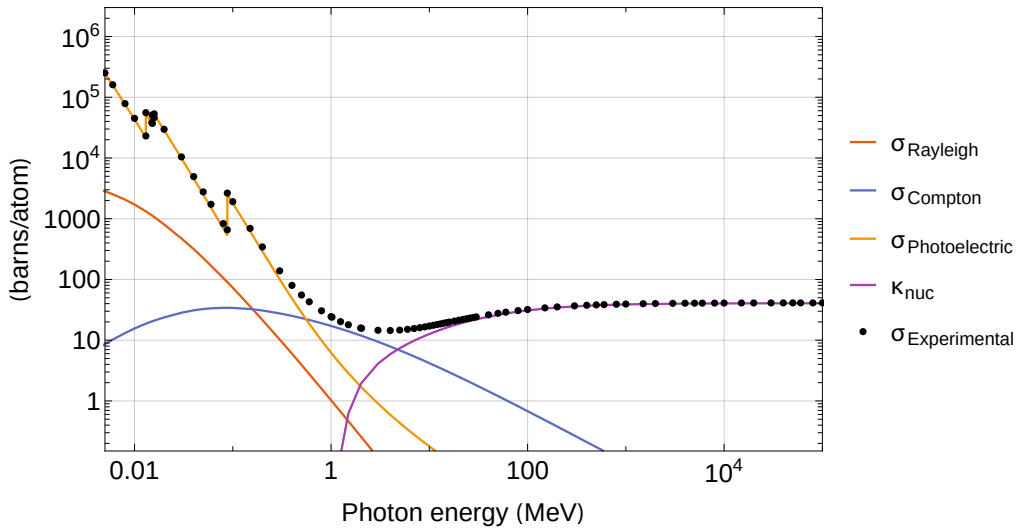

Figure 2.1: Photon interaction cross-sections for lead (Z=82) for different mechanisms and the experimental total cross-section. Data from the XCOM database [30].

2.1.1 Photoelectric effect

The photoelectric interaction is the absorption of a photon by an atom in the medium and consequent emission of a photoelectron: an electron that is kicked from its place by the photon, as shown in Fig. 2.2a. For this process to happen, it is necessary the photon to have equal or more energy that the binding energy of the electron. One can write

$$E_e = h\nu - E_b, \tag{2.1}$$

where E_e in the kinect energy of the outcoming photoelectron, h the Plank's constant, ν the frequency of the incoming photon and E_b the binding energy of the electron.

After removing the electron from an inner shell, an electron from the outer shell fills the vacancy, emitting a photon whose energy corresponds to the energy difference between the two levels. This photon is a characteristic X-ray of the element, shown in Fig. 2.2b. As there are several possible transitions, different characteristic X-rays can be produced.

Historically, they were named using Siagbahn notation: the first capital letter of the transition represents the end layer of the transition, as the second greek letter, the shell from where the electron comes, as shown in Fig. 2.3. However, due to some inconsistencies with Siegbahn notation, the IUPAC notation [31] was developed to substitute it, encompassing more information about the transition's initial and final energy levels.

There is also the possibility of a radiationless transition where an electron is emitted instead of a photon. This electron is called the Auger electron, shown in Fig. 2.2c.

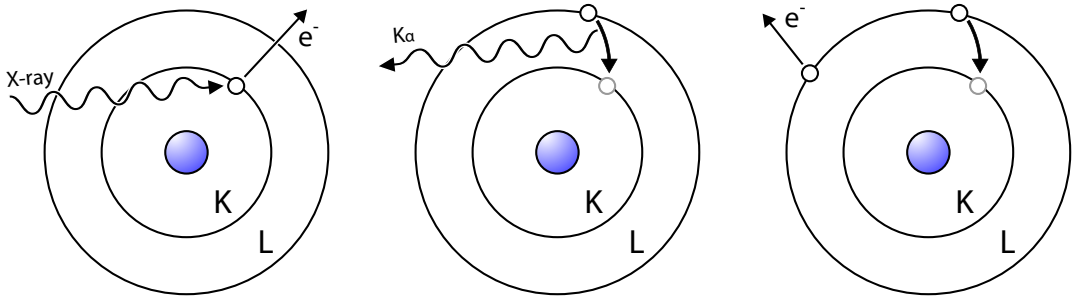

(a) (b) (c)

Figure 2.2: A photon can remove one electron of a given atom, expelling it from its place (a). The vacancy can be occupied by an electron from another level that emits a characteristic X-ray (b). There is the possibility that the system emitts another electron from the same atom, the Auger electron (c).

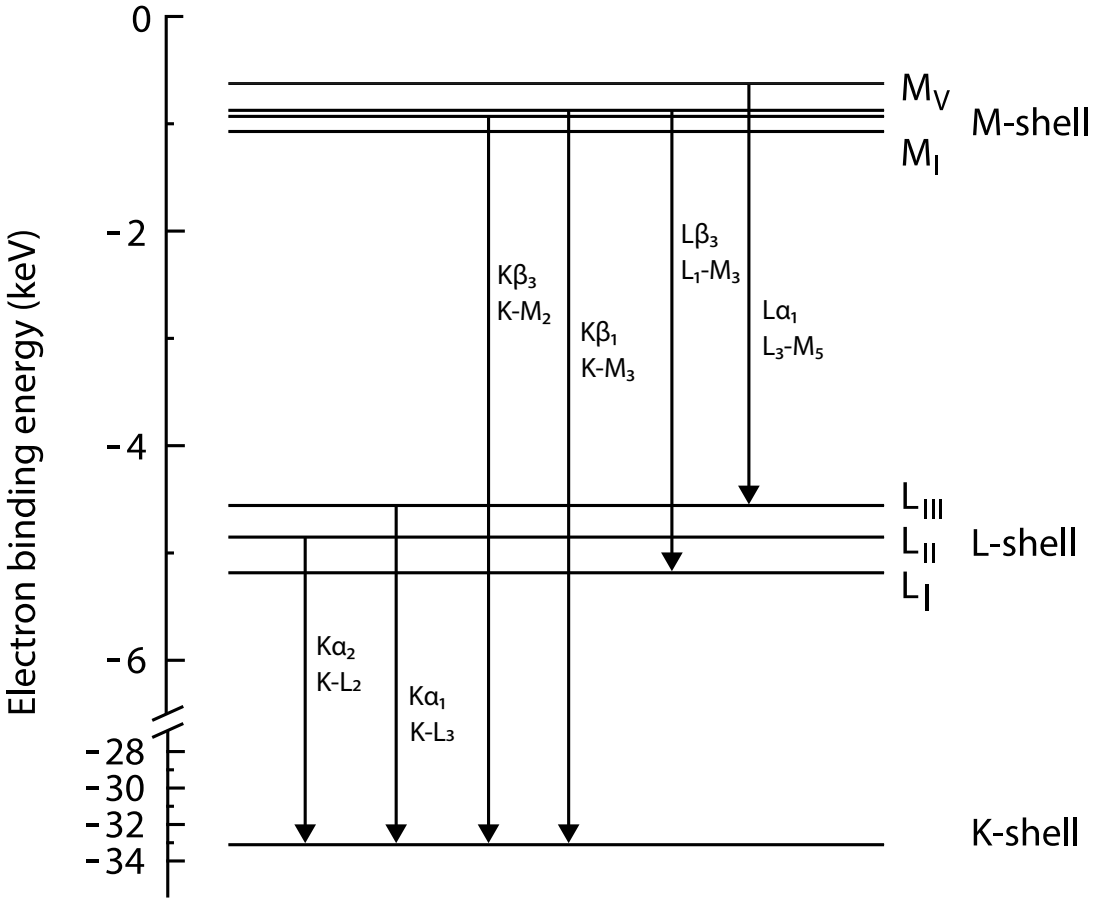

Figure 2.3: Series of the first allowed electronic transitions of Iodine using the Siagbahn (upper) and IUPAC (lower) notations and the respective binding energy for the first shells. Adapted from [32].

2.1.2 Compton Scattering

The Compton Scattering refers to the inelastic scattering of a photon by an outer electron in the target atom. The result of this scattering is a lower energy photon and a scattered electron, as it is called the electron removed from the atom because of the scattering. From the energy and momenta conservation laws, the energy difference between the incident and scattered photons depends on the angles involved. The Fig. 2.4 depics a diagram that illustrates the Compton Scattering.

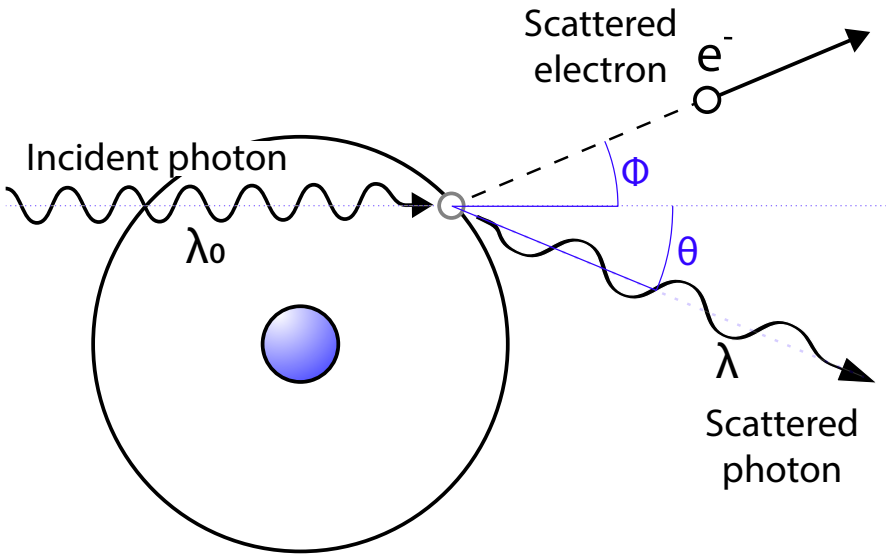

Figure 2.4: Diagram illustrating the Compton scattering of a photon with a wavelength λ_0 with an outer electron. The wavelength of the scattered photon is λ, and the difference of energy converts into the kinetic energy of the scattered electron. Figure from [33].

From the conservation laws, one can derive the dependency between the wavelengths of the incoming and scattered photons, given by

$$\lambda = \lambda_0 + \frac{h}{m_0 c}[1 - cos\theta], \tag{2.2}$$

where λ_0 is the incoming photon wavelength, λ is the scattered photon wavelenght, θ the scattering angle (see Fig. 2.4), h is the Planck's constant, m_0 the mass of the electron, and c the velocity of light. The assumptions to obtain this dependency are two: the first is to consider the electron at rest, and the second is to consider this electron almost free, which means with very low binding energy compared to the incoming radiation.

2.1.3 Pair production

The pair-production consists in the creation of electron-positron pair from an energetic photon in the Coulomb field of a given charged particle. It occurs typically in the vicinity of heavy nuclei but can also occur within the electronic cloud of a heavy atom. The minimum amount of energy necessary to incoming photon is [33]:

$$E \geq 2m_e c^2 \left(1 + \frac{m_e}{m_{nuc}}\right), \tag{2.3}$$

where c is the velocity of light, m_e the mass os the electron and m_{nuc} the mass of the nucleus in the vicinity where the production happens. As $m_e << m_{nuc}$, we can consider that the threshold energy is $1.022\,\mathrm{MeV}$, the sum of the energy given by the mass of the electrons. The cross-section κ_{nuc} for this effect is presented in Fig.2.1.

2.1.4 Rayleigh Scattering

The theory of the Rayleigh scattering was proposed by Lord Rayleigh in 1871 and considered the radius of the target smaller than the wavelength of photon [33]. There is virtually no energy exchange in this scattering, and it takes place for small energy photons, just changing the direction of the photon. This interaction mechanism is more important for low energies (see Fig. 2.1), but as it does not produce ionization, it is not important in our case. Nevertheless, it can be a problem for photon detectors since they can degrade the spatial resolution.

2.2 Charged particles

We can divide the charged particle interactions into heavy charged particles and the electrons or positrons interactions. The main differences between these groups lie in their energy deposition and their trajectories.

2.2.1 Heavy charged particles

There are several mechanisms by which heavy charged particles such as protons, alpha-particle, and ions can interact with matter. The most important one is the interaction between the charged particle and the electrons in the atoms of the target material via Coulomb forces. There is also the possibility of interacting electromagnetically with the nucleus (Rutherford scattering).

Since the electrons are bonded to the nucleus of a given atom in the target material, they need to gain an energy amount from the incoming radiation in order to be removed

(ionization), or to leap for a higher energy level (excitation). However, because of their small mass (compared with the heavy particles we mentioned), this energy transfer is limited to about 1/500 of the particle energy by nucleon[34].

Because of the several interactions (in all directions) and the small amount of energy exchange by interaction, the track traveled by the heavy charged particle is linear by most part until near its end, where the probability of changing its original direction is more prominent since it has little energy. A simulation of α particles in $^{10}B_4C$ is shown in Fig 2.5.

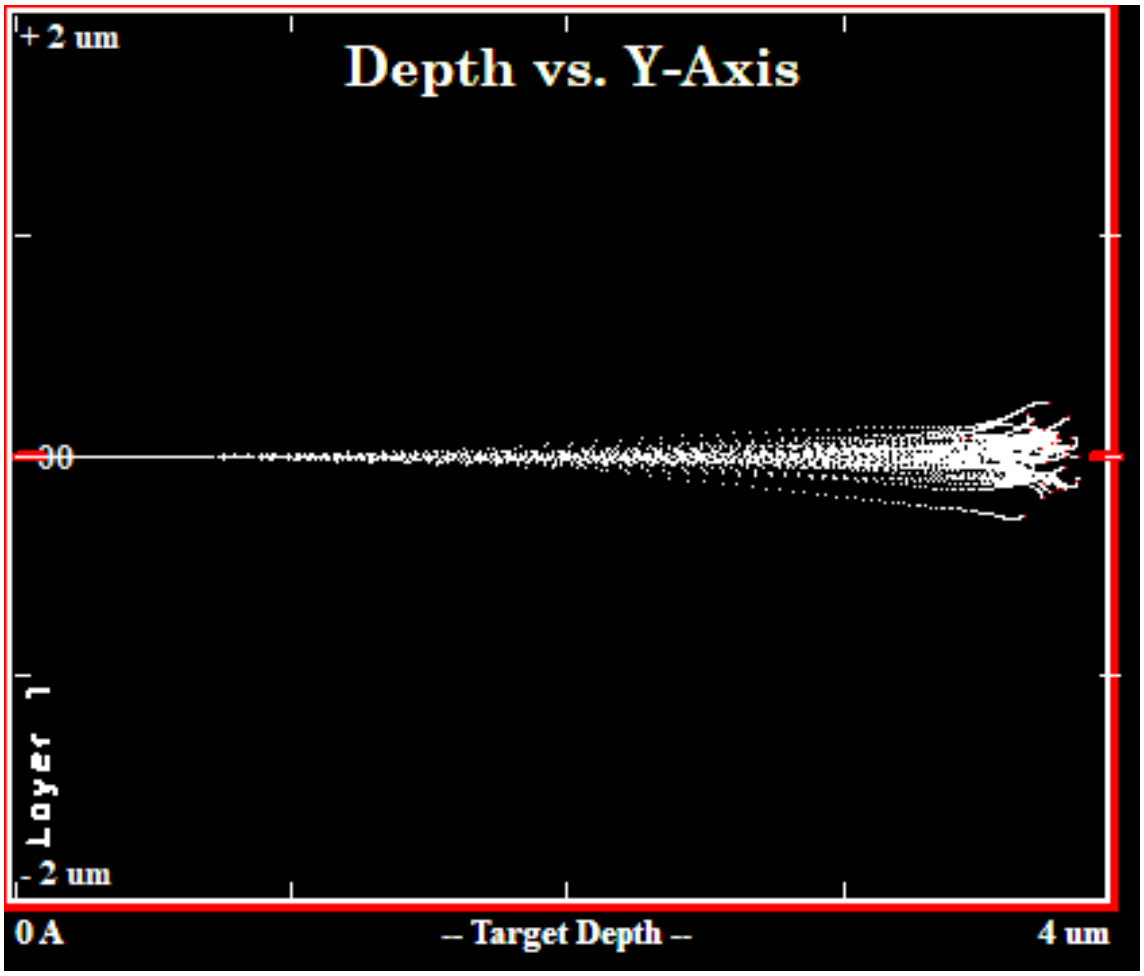

Figure 2.5: SRIM [35] simulation for 50 α particles with $1470\,\mathrm{keV}$ in $^{10}B_4C$. The tracks as calculated step by step, so each white point represents a position for some step.

Given the presented characteristics for the heavy charged particles interactions, we can define the stopping power, that represents the energy loss by the particle for a given medium for a infinitesimal path length [34]:

$$S = -\frac{dE}{dx}. \tag{2.4}$$

The stopping power can be divided into the nuclear and electronic components, where its sum is called total stopping power. Classically, S is well described by the Bethe-Bloch formula [33]:

$$-\frac{dE}{dx} = \frac{4\pi N_A r_e^2 m_e c^2 \rho Z q^2}{A\beta^2}\left[ln\left(\frac{W_{max}}{I}\right) - \beta^2 - \frac{\delta}{2} - \frac{C}{Z}\right], \tag{2.5}$$

where ρ, A, and I are the density, atomic number, and ionization potencial of the medium, respectively, q the electrical charge of the incoming particle, W_{max} the maximum energy that can be transferred in one interaction, and β a correction factor. The expression also depends on the constants N_A, m_e and r_e that represents the Avogadro's number, the rest mass of the electron and the classical radius of the electron, respectively. The δ is the correction regarding the shielding of distant electrons and C the correction for lower energies, that depends on the orbital velocities of the electrons. For compound materials we use the Bragg-Kleeman rule [33]:

$$\frac{dE}{dx} = \sum_{i=1}^{n} w_i \left(\frac{dE}{dx}\right)_i, \tag{2.6}$$

where w_i is the mass fraction of the i-th element of the mixture. It is also important to note that these processes are probabilistic, since they are probabilities of interaction and any real beam has an energy distribution, albeit a narrow one. Therefore, the Bethe-Bloch formula has to be tought as the mean energy loss for a particle in the medium.

Another important quantity to consider is the range, which can take different definitions. The main idea is to quantify the maximum length the particle can cross for a given material. Nevertheless, as we can see in Fig. 2.5, even though the tracks are rather straight, they are scatterings that impose statistical fluctuations to this quantity. One possible definition to the range is given by Fig. 2.6. It consists in plotting the relative intensity of the particle beam, regarding its original intensity as a function of the thickness of material crossed by the beam, and measuring the value in which this intensity decays to half. In the example case presented in Fig. 2.6 the range is 4 arbitrary units.

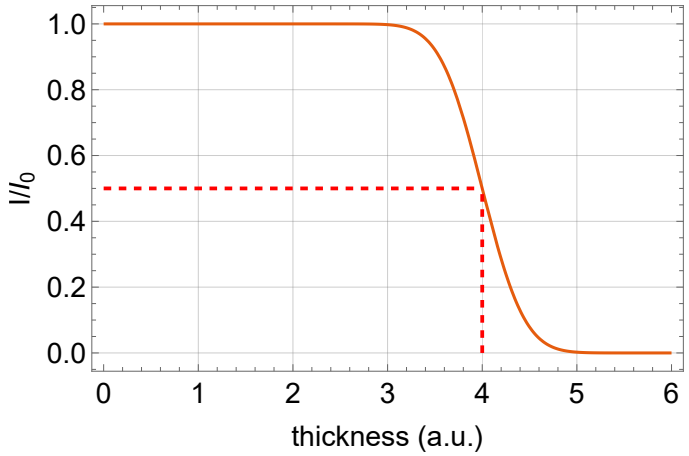

Figure 2.6: Example to assess the range of a hypothetical heavy charged particles beam. Image adapted from [34].

2.2.2 Rutherford Scattering

The Rutherford (or Coulomb) scattering was first described by Ernest Rutherford [36] and consists of the elastic scattering of the incoming particle by the nucleus of the atom purely for electromagnetic forces, as shown in Fig. 2.7. For the non-relativistic domain, the cross-section for Rutherford scattering is given by

$$\frac{d\sigma}{d\Omega} = \left[\frac{Z_1 Z_2 e^2}{16\pi\epsilon_0 E}\right] \frac{1}{sin^4(\theta/2)}, \tag{2.7}$$

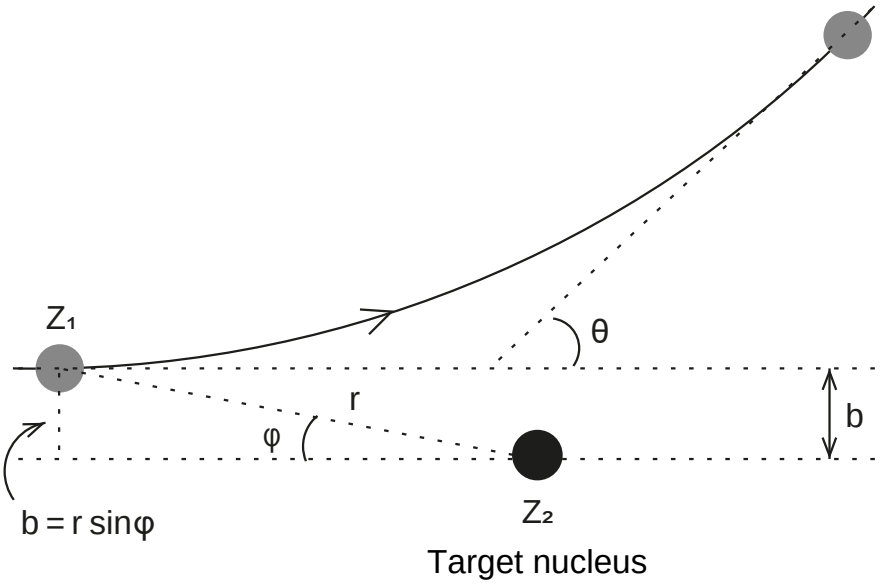

Figure 2.7: Rutherford scattering diagram. Image adapted from [33].

where Z_1 and Z_2 are the atomic number of the incoming and target particles, E is the

kinect energy of the incoming particle, e the charge of the electron and θ the scattering angle.

2.2.3 Electrons and positrons

Electrons and positrons interact with matter following different mechanisms. Since they present a small mass, they suffer substantial deviation in their trajectories, which turns out to be greatly tortuous, as seen in Fig. 2.8. The fractional energy loss of electrons and positrons per radiation length is shown in Fig. 2.9 as a function of the energy.

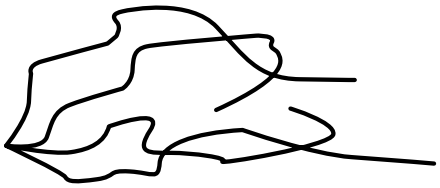

Figure 2.8: Example of trajectories for electrons with same energy. Image adapted from [34].

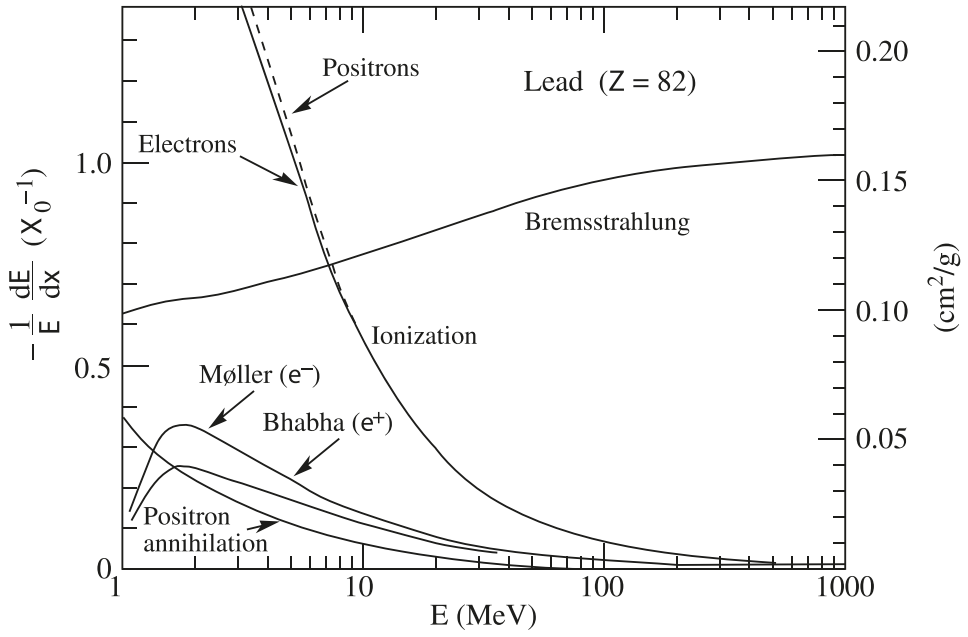

Figure 2.9: Fractional energy loss for different interaction mechanisms, as a function of the energy. Image from [33].

As shown in Fig. 2.9, the ionization process (already discussed) plays a significant part in the energy loss for electrons and positrons for lower energies. Moller and Bhabha scattering refer to electron-electron scattering and electron-positron scattering, respec-

tively, via photons exchange. The Bremsstrahlung mechanism is a radiative process that will be discussed later. Electron-positron annihilation will also be discussed later.

The energy loss can also be divided into collisional and radiative. Usually, for heavy charged particles the radiative component is negligible, since the particle does not change its path too much. For electrons and positrons this effect is much pronounced.

The definition of the range follows the same reasoning discussed for heavy particles, but some changes are needed. The beam's intensity decreases in a slower rate. Therefore we must evaluate the range by extrapolating the end of the dependence using a linear function. An example of the process is shown in Fig. 2.10.

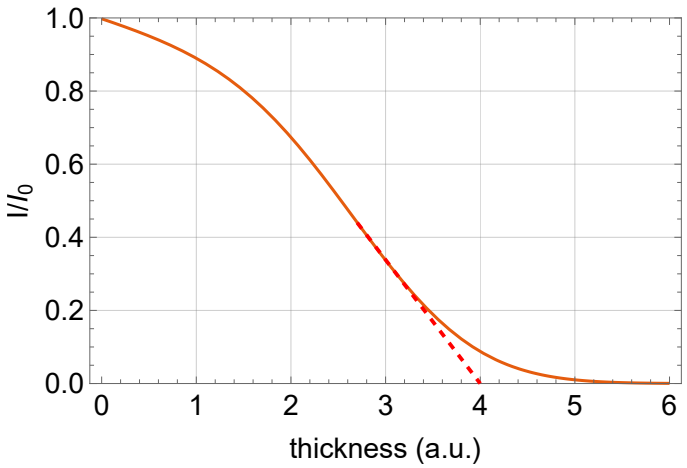

Figure 2.10: Method for estimating the range for electrons and positrons. In this example, the range is around 4 arbitrary units. Image from [34].

2.2.4 Bremsstrahlung

As the german name[1] suggests, this radiation is due to the deceleration of a charged particle. It is a radioative way of energy loss. There is a cutoff wavelength, above which Bremsstrahlung can happen, given by

$$\lambda_{min} = \frac{hc}{Ve}, \tag{2.8}$$

Where h is Planck's constant, c is the velocity of light, V is the potential under which the electron was accelerated, and e is the electron's charge. Typically, when an electron beam interacts with a heavy atoms target, several interactions occur, as depicted in Fig. 2.11.

[1] bremsstrahlung means "braking radiation" in german.

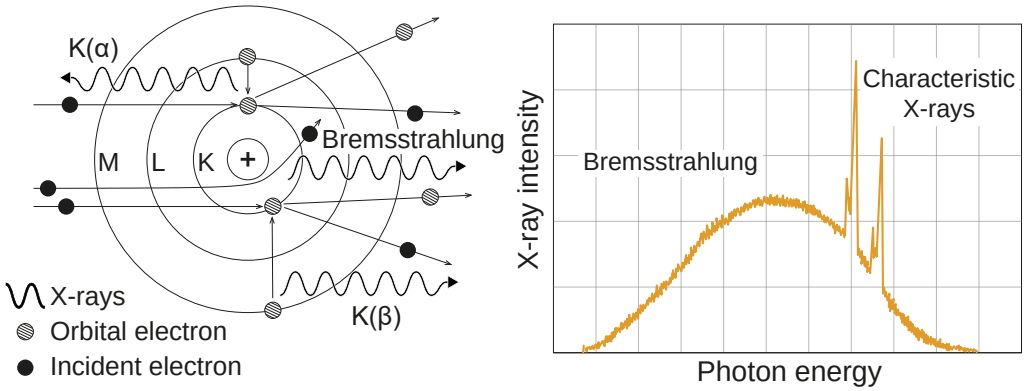

(a) (b)

Figure 2.11: Possible interactions between an electrons beam and the atom of a given target (a). The energy spectrum produced by Bremstrahlung (b) is continuous and above determined energy level characteristic X-rays are also emitted from the material. Figures adapted from [33].

2.2.5 Electron-positron annihilation

The electron-positron annihilation process happens when these two particles encounter each other, resulting in at least two photons with $511\,\mathrm{keV}$ energy. Because of the linear momentum conservation, it is impossible to produce just one photon. The photons energies comes from the electron rest mass ($511\,\mathrm{keV/c^2}$), direct implication of the concept of equivalence between mass and energy described by the relativity theory.

2.3 Neutron interaction

Discovered by James Chadwick in 1932, by bombarding berylium with alpha particles [37], the neutron is a fundamental component of atomic nuclei. Its understanding provided humankind the ability to use controlled nuclear reactions to generate energy, produce radiopharmaceuticals, treat cancer, study matter, and many other applications.

Since the neutron has no electrical charge, its interactions with matter are only nuclear or magnetic (with the electron's spin) and strongly depend on the target nucleus composition and the neutron energy. Two processes can take place in the neutron interaction: scattering or absorption. They can be subdivided as shown in Fig. 2.12, where each interaction has its own cross-section. All cross-sections summed up results in the total cross-section.

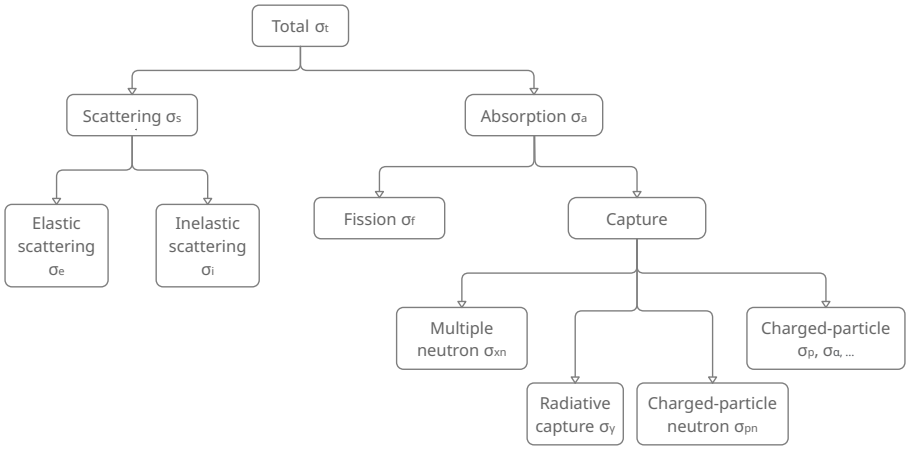

Figure 2.12: Diagram illustrating the different kinds of neutron interactions. Each of them has its own cross-section. Figure adapted from [38].

The names of these interactions can vary from different authors (see [33], for instance), but they are essentially categorized regarding the products of the neutron interaction. In scattering interactions, there is no transmutation of the target element, opposite to what happens to absorption events.

Neutron scattering

The scattering process is the most common interaction mechanism for fast neutrons and is subdivided into elastic or inelastic scattering.

In the elastic scattering, the energy of the system is the same both before and after the interaction. In the inelastic case, part of the energy lost by the neutron is absorbed by the target nucleus that reaches an excited state and eventually emits radiation [38]. The average energy loss of the inelastic scattering is $2EA/(A+1)^2$ [39], which means that using lighter targets quickly reduces the number of collisions needed to make the neutron loose a higher amount of energy. This is useful for neutron moderation when we want to thermalize neutrons. Common materials used for this purpose are water, paraffin, and other hydrogenated compounds since each inelastic scattering with hydrogen will reduce the neutron energy by half.

Neutron absorption

Unlike scattering, the absorption processes change the target nucleus and its possible outcomes vary from gamma rays to several fragments.

The radiative capture, brings the target nucleus to an A+1 excited state that returns to the ground state through gamma-ray emission. The process can be written as A(n,γ)A+1

and has important applications such as neutron flux measurement, using the reaction ^{197}Au(n,γ)^{198}Au, and radioisotopes production, like ^{59}Co(n,γ)^{60}Co [33].

The charged and neutral captures, pictured in Fig. 2.12 as the "charged-particle neutron", "charged-particle", and "multiple neutron", differ regarding the products of the reactions. While neutral capture behaves similarly to an inelastic collision concerning the reaction income and outcome, the charged capture releases charged particles at the end of the process. Examples of neutral and charged captures are ^{9}Be(n, 2n)^{8}Be and ^{10}B(n,α)^{7}Li, respectively.

Finally, fission is one of the most important kinds of reaction. It happens with heavy nuclei that split into large fragments plus the emission of neutrons and gammas. This reaction capture a neutron and forms the basic working principle of nuclear reactors, in the case where the emitted neutrons are able to trigger other reaction, forming a *chain reaction*, as depictured in Fig. 2.13. A possible fission reaction for the ^{235}U is [33]:

$$\mathrm{n} + \mathrm{U}_{92}^{235} \rightarrow \mathrm{I}_{39}^{139} + \mathrm{Y}_{53}^{95} + 2\mathrm{n} + \gamma. \tag{2.9}$$

In this case, ^{95}Y and ^{139}I represent the most probable elements, but other elements are also produced.

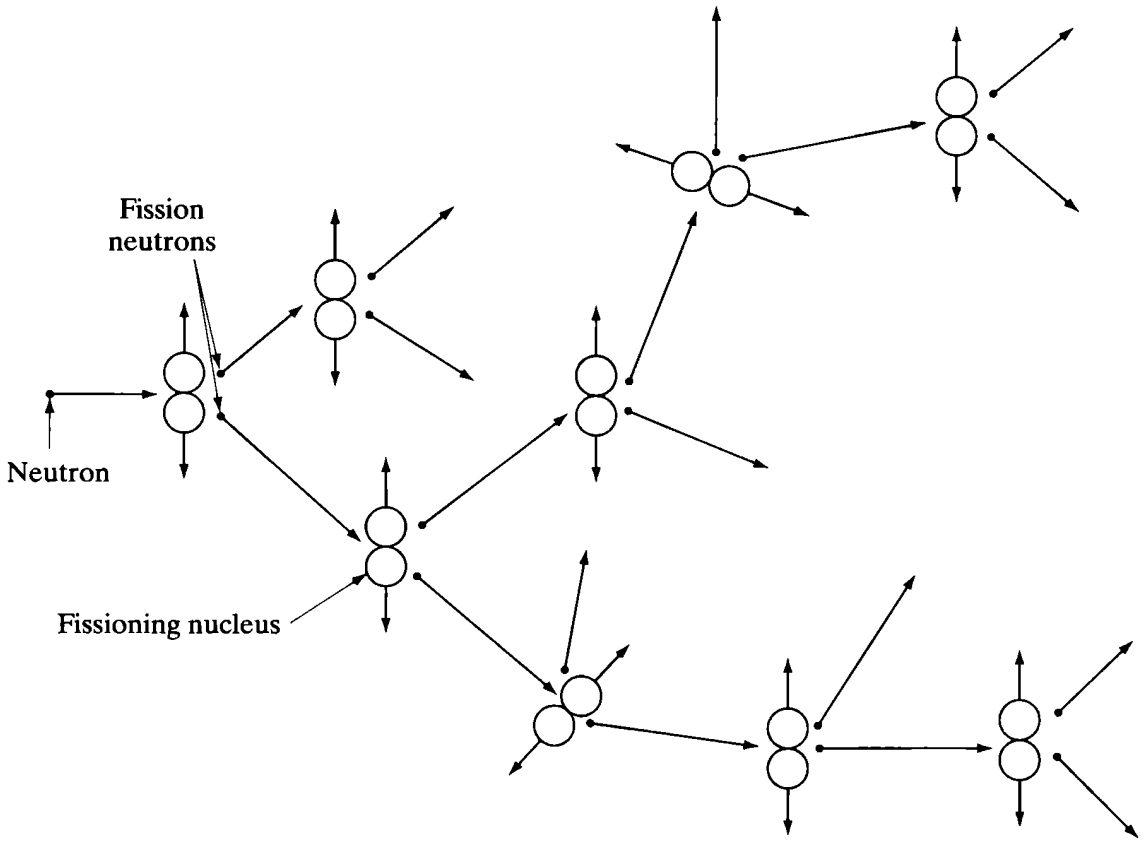

Figure 2.13: Diagram illustrating a fission chain reaction. Figure from [40].

The probability of a neutron undergoing a certain kind of nuclear reaction is given by its cross-section. Each of these processes has its own microscopic cross-section, where the total microscopic cross-section defined as the sum of all:

$$\sigma_t = \sigma_e + \sigma_i + \sigma_{el} + \sigma_c + \sigma_n + \sigma_f \tag{2.10}$$

The *absorption cross-section* (σ_a) is defined [40] as the sum of the cross-sections of the right branch of Fig. 2.12, last four terms of Eq. 2.10, and the *scattering cross-section* (σ_s) as the sum of the cross-sections of the left branch of Fig. 2.12, first two terms of Eq. 2.10. As these probabilities are functions of the neutron energy, all cross-sections are energy-dependent and a clever way to classify neutrons is using their energy.

From the de Broglie's equation for wavelength [41] and the kinect energy relation, it is possible to express the neutron energy in terms of its wavelength as well:

$$\lambda = \frac{h}{p} = \frac{h}{m_n v} \quad \text{and} \quad E = \frac{1}{2} m_n v^2 \Rightarrow \boxed{\lambda = \frac{h}{\sqrt{2 m_n E}}}, \tag{2.11}$$

where we considered the non-relativistic regime. Figure 2.14 depicts the dependency expressed in Equation 2.11 for some neutron energy values (see Table 2.1).

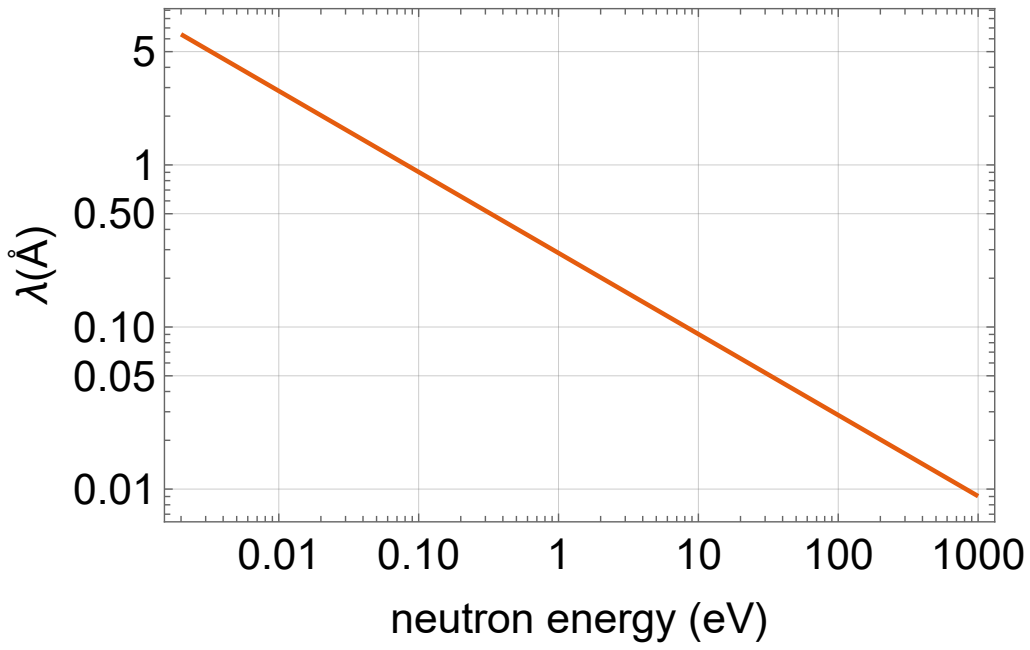

Figure 2.14: Relation between wavelength and energy, described in Eq. 2.11.

As mentioned, the neutrons are often classified according to its energy, as shown in Table 2.1, even tough the classification is more related to the kind of predominant process than a real intrinsec difference [42].

Table 2.1: Neutron energy ranges classification. Table from [43].

	kinectic energy (eV)	wavelenght (Å)	velocity (m/s)
ultra cold (UCN)	smaller than 3×10^{-7}	bigger tham 520	smaller than 7.5
very cold (VCN)	3×10^{-7} to 5×10^{-5}	520 to 40	7.5 to 99
cold	5×10^{-5} to 5×10^{-3}	40 to 4	99 to 990
thermal	5×10^{-3} to 0.5	4 to 0.4	990 to 9900
epithermal	0.5 to 1×10^{3}	0.4 to 0.01	9900 to 4.4×10^{5}
intermediate	1×10^{3} to 1×10^{5}	0.01 to 0.001	4.4×10^{5} to 4.4×10^{6}
fast	1×10^{5} to 1×10^{10}	1×10^{-3} to 3×10^{-6}	4.4×10^{6} to 1.3×10^{9}

Thermal neutrons are particularly useful in neutrongraphy and neutron diffraction. In addition to the reasonable cross-section of many isotopes within this energy range, the wavelength of thermal neutrons is generally compatible with the interplanar distance of the condensed matter samples studied with these techniques. The most used element for neutron detection is ^{3}He , which can be considered unavailable nowadays, as we will discuss later. Other commons isotopes applied to neutron detection are ^{10}B , ^{6}Li , ^{157}Gd , ^{113}Cd , etc. Figure 2.15 shows the cross-sections for some of these elements.

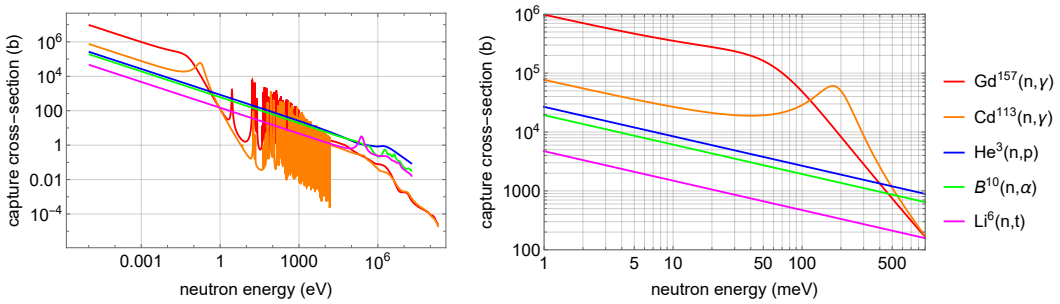

Figure 2.15: Main capture cross-section for different elements (left) and its zoom to the thermal/epithermal region (right). Data from [44].

In this work, we use ^{10}B as a thermal neutron converter through $^{10}B_4C$ deposition on aluminum. The thermal neutron capture reaction ^{10}B (n,α)^{7}Li has two possible outcomes [45], shown below:

$$\mathrm{n} + {}^{10}\mathrm{B} \longrightarrow \begin{cases} {}^{7}\mathrm{Li}(840\,\mathrm{keV}) + {}^{2}\mathrm{He}(1470\,\mathrm{keV}) + \gamma(480\,\mathrm{keV})\ (94\%) \\ {}^{7}\mathrm{Li}(1015\,\mathrm{keV}) + {}^{2}\mathrm{He}(1775\,\mathrm{keV})\ (6\%) \end{cases} \tag{2.12}$$

It is essential to notice that the products of Eq. 2.12 are expelled through antiparallel trajectories, which means that detectors projected to collect these outcomes from just one side of the deposition will detect only one of the products at a time. Antiparallelism is a direct consequence of momentum conservation because the kinetic energy of the

incoming thermal neutron is negligible compared to the energy of the products of the reaction.

2.3.1 Thermal neutron capture

Given a monochromatic neutron beam of energy E and considering a target with σ neutron capture cross-section for this energy, the capture rate is given by [37]:

$$r = N_t \Phi \sigma \tag{2.13}$$

where N_t is the total number of capture nucleus in the target and Φ is the neutron flux. For a thin layer of the target material, the number N_c of captured neutrons per unit time is then:

$$N_c = NA\Phi\sigma dx \tag{2.14}$$

where N is capture nucleus density (N_t/V), A the area of material illuminated by the beam, and dx the thickness of the layer under consideration. Note that $A \cdot \Phi$ is the number of neutrons hitting the target every second. So, the capture probability $\mathcal{C}(dx)$ for this target can be calculated by dividing the number of captured neutrons (N_c) by the total number of neutrons hitting the target ($A \cdot \Phi$), which results

$$\mathcal{C}(dx) = N\sigma dx = \Sigma dx, \tag{2.15}$$

where Σ is the macroscopic cross-section, by definition [38]. Consequently, the survival probability for a given neutron is the probability of no capture, $P(dx) = 1 - \Sigma dx$, for the thin target we defined. This analysis can be extended to the bulk of material shown in Fig. 2.16.

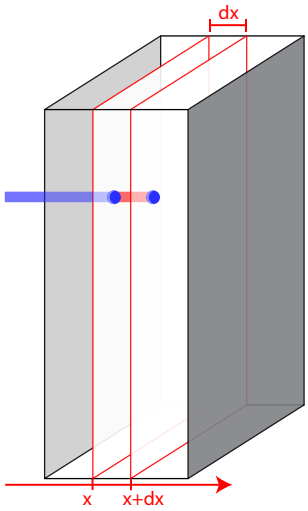

Figure 2.16: Representation of neutron traveling through thin layer of thickness dx inside a bulk of converter material.

The probability of the neutron surviving until $x + dx$ is given by:

$$P(x + dx) = P(x)(1 - \Sigma dx) \tag{2.16}$$

which corresponds to the probability of survival after x distance *and* the probability of survival after the layer of thickness dx. The survival probability $P(x)$ can be evaluated from Equation 2.16, as follows:

$$\begin{aligned} \frac{dP}{dx} &= \lim_{dx \to 0} \frac{P(x + dx) - P(x)}{dx} = \lim_{dx \to 0} \frac{P(x)(1 - \Sigma dx) - P(x)}{dx} \\ \frac{dP}{dx} &= -\Sigma P(x) \Rightarrow P(x) = Ae^{-\Sigma x} \Rightarrow \boxed{P(x) = e^{-\Sigma x}} \end{aligned} \tag{2.17}$$

Note that the the constant A is calculated from the boundary condition $P(0) = 1$. One can evaluate also the mean free path mfp following the definition:

$$mfp = \frac{\int_0^{+\infty} xP(x)dx}{\int_0^{+\infty} P(x)dx} = \frac{1}{\Sigma} \tag{2.18}$$

By definition, the *mfp* is the required distance to attenuate the beam by $1/e$. This happens because the particles are independent of each other and the beam can be interpreted as a set of many particles that follow the same interaction probability. For that reason, the beam flux after pass through thickness x of the target can be modelled by [34]

$$\Phi(x) = \Phi_0 e^{-\Sigma x}. \tag{2.19}$$

Chapter 3

Gaseous detectors

In Chapter 2 we discussed how the passage of ionizing radiation through matter produce ionizations by different mechanisms. The charges produced by the ionizations may be separated by an external electric field and drifted toward readout electrodes. This is the basic working principle of several detectors, such as gaseous detectors, that we will discuss more in this chapter. The charges collected allow to determine information about the nature of this radiation such as intensity and type of radiation.

3.1 Interactions with gases

It is also helpful to distinguish between primary and secondary ionization. By definition, the primary ionizations are produced directly by the incoming radiation. Meanwhile, the secondary ionizations are due to the interaction of the products of the primary ionization. The W-value already takes into account these two types of interaction, therefore, we can evaluate the average number N of ion-pairs created by a source of radiation that deposits an energy ΔE inside a given volume of interest in the following way:

$$N = \frac{\Delta E}{W} \tag{3.1}$$

For charged particles, it is particularly useful to consider the average number of ion-pairs by length, which is related to the stopping power:

$$n = \frac{1}{W}\frac{dE}{dx} \tag{3.2}$$

It is meaningful to remember that n and N are statistical quantities since the interaction processes are stochastic. Nevertheless, they represent appropriately the global behavior in which radiation interacts with matter.

In several cases, it is necessary to use mixtures of gases, and therefore the quantities

Table 3.1: Density (ρ), ionization potentials (I_e), W-values, stopping powers (dE/dx) for minimum ionizing particles, primary ionization yield (n_p) and total ionization yield (n_t) for different gases. The ionization yields consider atmospheric pressure. Table from [46].

Gas	Z	ρ ($\times 10^{-4}$ g/cm^3)	I_e (eV)	W (eV/pair)	dE/dx (keV cm^{-1})	n_p (ip/cm)	n_t (ip/cm)
H_2	2	0.8	15.4	37	0.34	5.2	9.2
He	2	1.6	24.6	41	0.32	5.9	7.8
N_2	14	11.7	15.5	35	1.96	10	56
O_2	16	13.3	1.2	31	2.26	22	73
Ne	10	8.4	21.6	36	1.41	12	39
Ar	18	17.8	15.8	26	2.44	29	94
Kr	36	34.9	14	24	4.60	22	192
Xe	54	54.9	12.1	22	6.76	44	307
CO_2	22	18.6	13.7	33	3.01	34	91
CH_4	10	6.7	10.8	28	1.48	46	53

discussed have to be evaluated for the resulting combination of gases. As these quantities are averages, the resulting value for the mixture equals the weighted average of the same quantity for all the gases that compound the mix. Therefore, the weight we use encompasses the information about the amount of each gas in the mixture. The easiest way to do that is to consider the fractional volume as weight since for the same conditions of pressure and temperature, the volume is proportional to the quantity of matter.

For instance, we can evaluate the number of ions-pairs generated by an $ArCO_2$ (90/10) gaseous mixture, weighing the number n of pairs produced, given in Eq. 3.2, by the volumetric fraction of the gases in the mixture [33]:

$$n_t = \sum_i x_i \frac{(dE/dx)_i}{W_i} = 0.9\frac{2.44 \times 10^3}{26} + 0.1\frac{3.01 \times 10^3}{33} \approx 94\,\text{pairs/cm} \tag{3.3}$$

3.1.1 Diffusion and drift

Considering the simplest case of a gaseous volume without an external electric field applied, the free charges created by radiation follow the thermal motion of the gas. As a consequence, the kinetic energy distribution for the charge carriers is described by Boltzmann's law, given by:

$$p(E) = 2\sqrt{\frac{E}{\pi(kT)^3}}e^{-E/(kT)} \tag{3.4}$$

where T is the temperature of the gas and k the Boltzmann's constant. The mean

energy can be evaluated by integrating the probability distribution, which results in

$$\bar{E} = \frac{\int_0^\infty Ep(E)dE}{\int_0^\infty p(E)dE} = \frac{3}{2}kT \tag{3.5}$$

corresponding to aproximately $25\,\mathrm{meV}$ considering common ambient conditions ($300\,\mathrm{K}$). The distribution of velocities is given by the Maxwell-Boltzmann distribution:

$$f(v) = 4\pi\left(\frac{m}{2\pi kT}\right)^{\frac{3}{2}} v^2 e^{-\frac{mv^2}{2kT}}, \tag{3.6}$$

plotted for some gases in Fig. 3.1.

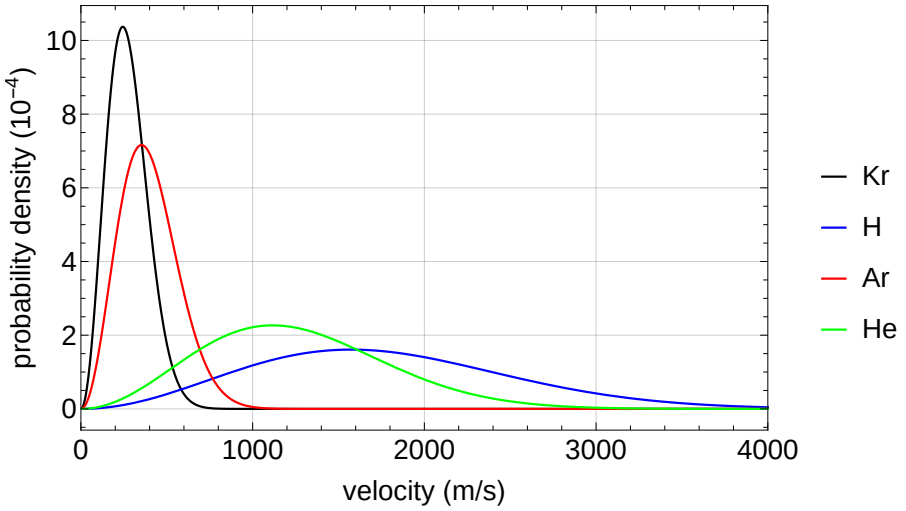

Figure 3.1: Velocity distributions of the molecules in the gas for different gases given by Eq. 3.6, for $300\,\mathrm{K}$.

In the absence of an external electrical field, the ionizations generated in a particular region of the gas will diffuse isotropically, given that they follow the thermal motion of the gas. Therefore, the distribution of their position for any direction will spread over time. For example, considering the X direction, this diffusion can be described by the following Gaussian distribution [47]:

$$\frac{dN}{N} = \frac{1}{\sqrt{4\pi Dt}} e^{-x^2/(4Dt)} dx \tag{3.7}$$

where N is the total number of charges produced by the ionizations, dN is the number of charges that can be found between x and $x + dx$ coordinates from the original spot where the diffusion began, and t is the time passed after the beginning of the diffusion. This distribution also depends on the diffusion coeficient D, generally given in $\mathrm{cm^2\,s^{-1}}$. This is an important quantity that is used to determine the standard deviation of the linear and volumetric distributions:

$$\sigma_x = \sqrt{2Dt} \qquad \text{and} \qquad \sigma_V = \sqrt{6Dt}. \tag{3.8}$$

When in presence of an external electric field, the charged particles obtain a drift velocity v_d and the distribution of Equation 3.7 becomes:

$$\frac{dN}{N} = \frac{1}{\sqrt{4\pi Dt}} e^{-(x-tv_d)^2/(4Dt)} dx \tag{3.9}$$

For ions, the drift velocity is given by

$$v_d = \mu_+ \frac{E_l}{P}, \tag{3.10}$$

where E_l is the external electric field, P is the gas pressure and μ_+ is the ion mobility, that is related with the diffusion coefficient for ions D_+ by the Nerst-Einstein relation [33]:

$$\mu_+ = \frac{e}{kT} D_+, \tag{3.11}$$

where k is the Boltzmann's constant, e the charge of the electron and T is the temperature. The diffusion coefficient is important because it defines the time needed by the charges to be collected. Some values of diffusion coefficient are shown in Table 3.2, for ions in their own gases.

Table 3.2: Diffusion coeficient D and mobility μ of ions in their own gas in the abscence of external electric field at $300\,\mathrm{K}$. Mobilities from [47, 48] and D calculated from Eq. 3.11.

Gas	D ($\mathrm{cm^2\,s^{-1}}$)	μ ($\mathrm{cm^2\,s^{-1}\,V^{-1}}$)
CO_2	0.03	1.09
Ar	0.04	1.52
N_2	0.05	1.90
O_2	0.06	2.23
Ne	0.10	4.08
He	0.27	10.3

The drift velocities for some ions are shown in Fig. 3.2.

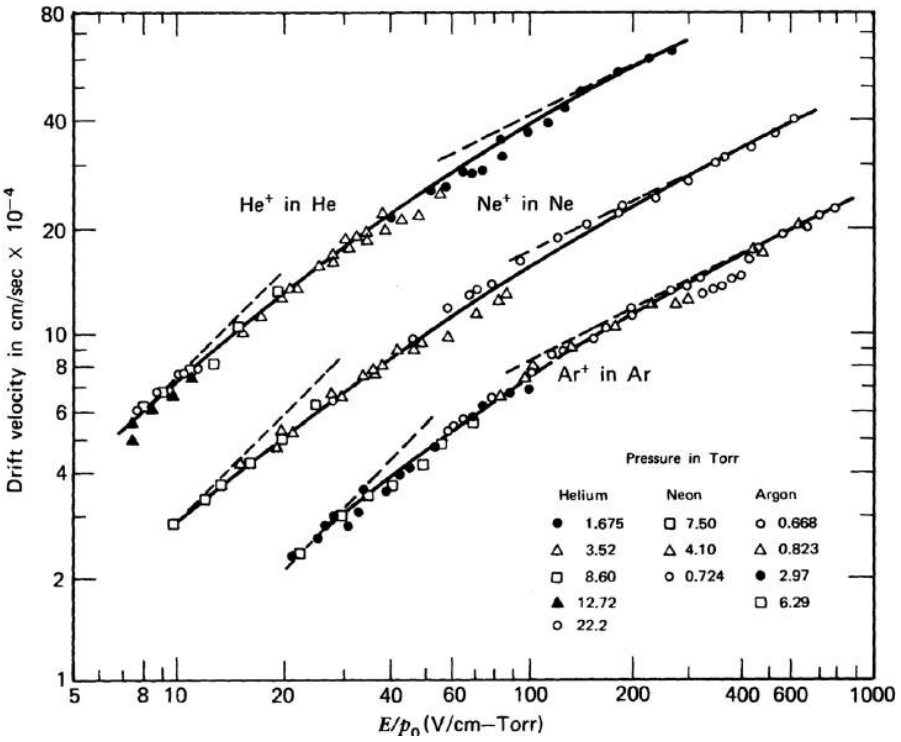

Figure 3.2: Drift velocities for ion in its own gases. Figure from [47] (originally from [49]).

For a gaseous mixture, the mobility is given by the Blanc's law:

$$\frac{1}{\mu_i} = \sum_{j=1}^{n} \frac{p_j}{\mu_{ij}} \tag{3.12}$$

where μ_i is the mobility of a given ion in the gaseous mixture, μ_{ij} the mobility of the ion in the gas j and p_j the volume concentration of gas j in the mixture.

For instance, considering the $ArCO_2$ (90/10) mixture, the mobility of the CO_2^+ ion can be easely evaluated:

$$\frac{1}{\mu_{CO2}} = 0.9\frac{1}{1.72} + 0.1\frac{1}{1.09} \Longrightarrow \mu_{CO2} \approx 1.63\,\mathrm{cm^2 s^{-1} V^{-1}} \tag{3.13}$$

where we use the mobility for the CO_2^+ ion in its own gas, from the Table 3.2, and the CO_2^+ mobility in Ar ($1.72\,\mathrm{cm^2\,V^{-1}\,s^{-1}}$), taken from [50].

For electrons, the above relations are not valid. Because of their very small mass and consequently their fast energy gain, their velocity distribution does not follow the Maxwell-Boltzmann statistic. Their drift velocity can be estimated by [51]:

$$v_d = \frac{2eE_l d_{mt}}{3m_e \bar{v}_e} \tag{3.14}$$

where d_{mt} is the mean free path of the electron, v_e is its thermal velocity inside the

gas, m_e its mass, e its charge and E_l the external electric field. The typical values of drift velocity for electrons are a few[1] centimeters per microsecond, as shown in Fig. 3.3.

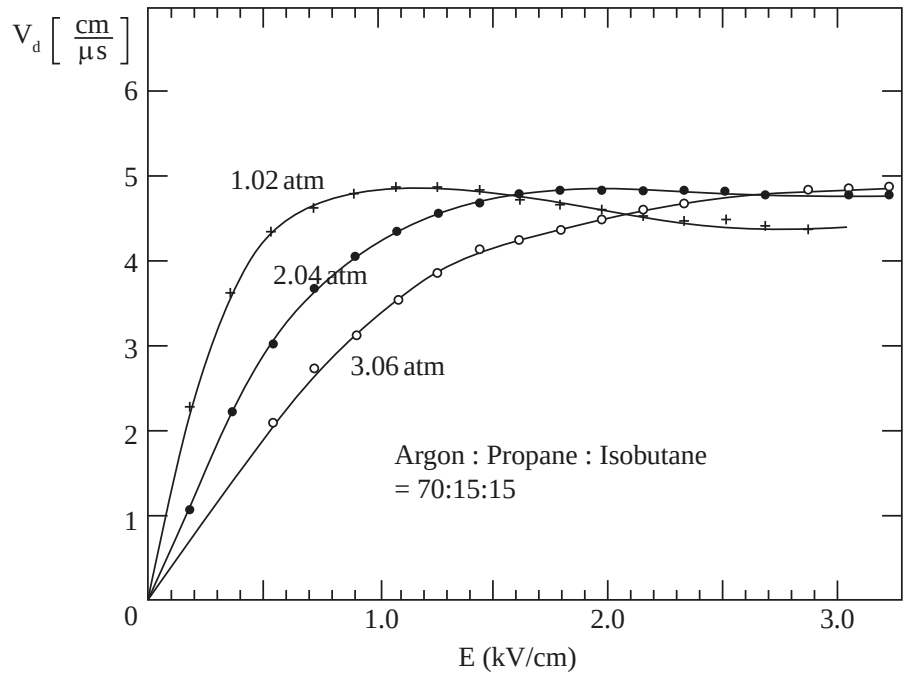

Figure 3.3: Drift velocity of electrons for different pressures in a gaseous mixture of argon, propane and isobutane, as a function of the external electric field. Adapted from [33].

From Eq. 3.14, the drift velocity depends on the electron's mean free path, which has a dependency on the pressure (and as a consequence of the temperature). It also depends on the species of gas used. The result of this fact is that these detectors are sensitive to pressure and temperature. These considerations are also extended to the avalanche multiplication process that will be discussed afterward.

3.1.2 Other mechanisms

During the drift, the charges undergo a large number of collisions, other interactions can happen, such as electron attachment, charge transfer, and recombination.

The electron attachment mechanism is particularly important when dealing with different gaseous species and one of them has tendency to form negative ions, capturing free electrons from the ionizations. The charge transfer, on the other hand, happens in collisions between positive ions and gas molecules. In this case, the ion receives one electron from the neutral gas molecule, which now becomes the ion. This phenomenon commonly

[1] tipically between $1\,\mathrm{cm\,\mu s^{-1}}$ and $6\,\mathrm{cm\,\mu s^{-1}}$ for most gases.

appears when there is a difference in ionization energy of the species involved, so the collision's energy takes part in the process.

The recombination happens in collisions between positive ions and the free electron, which is captured, turning the ion into a neutral atom/molecule. It can happen also in a collision between positive and negative ions where the products are two neutral species. This effect is important because it degrades the signal, i.e., the recombined charges are no longer counted, therefore is desirable to minimize this effect the maximum as possible. It is possible to write the recombination rate as [34]:

$$\frac{dn^+}{dt} = \frac{dn^-}{dt} = -\alpha n^+ n^- \tag{3.15}$$

where α is the recombination coefficient, n^+ the number density of positive species and n^- the number density of negative species. We expect that the recombination depends on several factors such as gas pressure and temperature. It is important to mention that there are two types of recombination, denominated *columnar recombination* and *volume recombination*. The first one refers to the recombinations generated by highly ionization particles because near their track, the density of both positive and negative charges is very high. This kind of recombination depends on the nature of the radiation rather than its rate. The second is particularly interesting because is the recombination generated by the interaction of this charges during the drift. The strategy to minimize recombinations is to promote a quick drift and separation of the ionizated charges, which can be achieve using intense electric fields.

3.2 Operation of gaseous detectors

3.2.1 Operation regimes

In this section, we briefly discuss the different operation regimes for gaseous detectors. These regimes depends on the voltage applied to the detector, as shown in Figure 3.4, and are related to its working mode (e.g. pulsed or continuous).

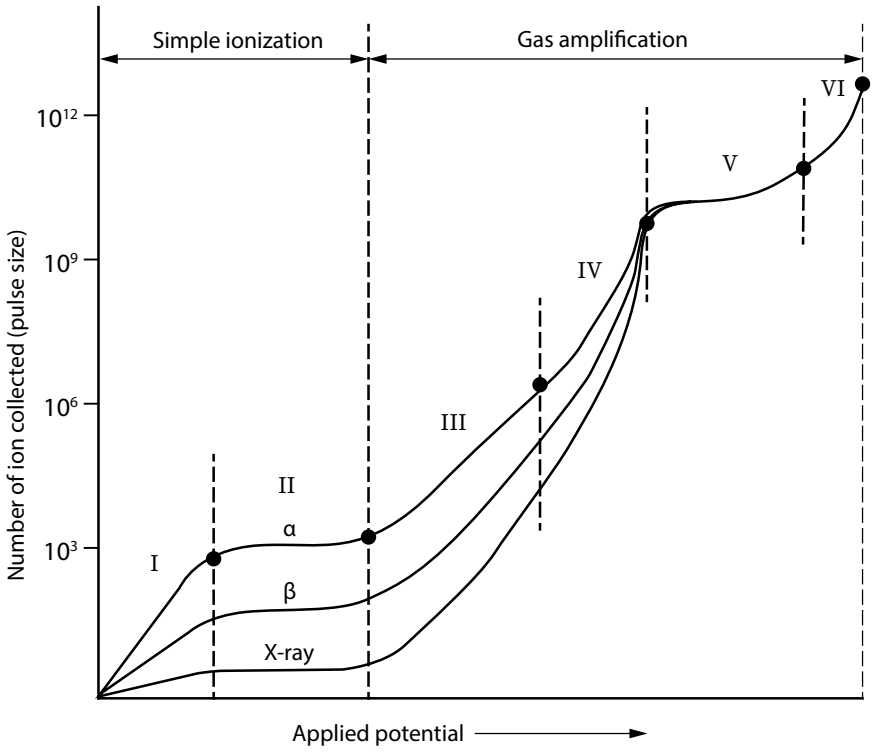

Figure 3.4: Collected charge in the function of applied voltage for different incident radiation. The differences of these curves are related to the capacity that each radiation has to produce charges in the gas. From the six distinct regions, three of them are used. Figure adapted from [52].

In the recombination region (I of Fig. 3.4), the recombination rate (see Eq.3.15) is significant to prevent any reasonable measurements since the charges measured have no proportional dependence on the energy deposited by the incoming radiation. Therefore, this is an unused region.

As rising the voltage, one gets to the ionization chamber region (II of Fig. 3.4), in which the recombination is negligible, or at least exists a proportional relation between the energy deposited by the radiation and the collected charge. It is interesting to note that this region forms a plateau, which reflects the fact that there is a range of voltages that are equivalent in terms of the collected charges because within this range they are all being efficiently collected. The drift zone of our detector, which will be detailed further, operates at this regime.

Going further on the voltage scale, one comes to the proportional region (III of Fig. 3.4), where the multiplication part of the detector prototype build in this work operates. In this region, the charges produced by the incoming radiation are smaller than the collected charges. Therefore, this region presupposes a proportional multiplication of charges (see section 3.4.1). There are some techniques to assure this proportionality of the multiplication, usually making use of geometrically delimited regions within the detector where

this multiplication occurs. This is the case of the Multi-Wire Proportional Chambers (MWPCs) [25], the Micro-Strip Gas Chamber (MSGC) [53], the Gas Electron Multipliers (GEMs) [26], the Micro-Mesh Gaseous Structures (MicroMegas) [28], and similar detectors.

For even higher voltages, the produced ions start limiting the efficiency of the detector due to the high amount of multiplications (IV of Fig. 3.4). Ions are very slow compared with the electrons and when produced in a high amount they start to shield the electric fields responsible for causing the multiplication. In this case, by consequence, the recombination rate also rises. It leads to a loss of linearity regarding the multiplication process, where the charges collected are no longer proportional to the deposited energy by the incident radiation, which results in a not so useful regime.

By applying even more voltage, one gets to the Geiger-Muller region (V of Fig. 3.4). In this region, every ionization generated in the gas is enough to start an avalanche multiplication, thus it is not possible to collect information about the nature of the incoming radiation. Nevertheless, the Geiger-Muller detectors are essential in monitoring the activity of a radioactive source. They usually have a thin ceramic/polymer window at one end of the tube to allow the passage of charged radiation below a specific range of energy (that could not pass through the metal walls of the tube), which consists of a preliminary way to distinguish radiation.

For last, rising even more the voltage, one enters in the continuous discharge region (VI of Fig. 3.4), where a single ionization starts an avalanche that induces electric arcs in the gas (breaking its dielectric rigidity), which means that the detector is clearly inoperable (and commonly damaged) in this regime.

3.2.2 Operation modes

There are essentially three modes of operation regarding radiation detectors: current mode, pulse mode and mean square voltage mode [34], where the first two are the most common.

The current mode consists of directly measuring the current generated by the radiation. The response time used in these measurements should be intentionally long in order that the average current measured can be expressed in terms of the radiation rate and the average charge generated by the radiation, minimizing random fluctuations. It is possible to write, in this case:

$$\bar{I} = rQ \tag{3.16}$$

with Q representing the average charge produced by each event. This kind of opera-

tion is particularly useful when the event rates are high.

The most used operation mode is the pulse mode (the one used in this work), which provides information about the timing and intensity of the incoming radiation. It is common to use a preamplifier to collect the incoming signal and generate a voltage pulse with fast-rising and exponential decay (we discuss in more detail this process in section 5.3), whose timing characteristics are defined by the time constant RC of its circuitry.

3.3 Ionization Chambers

Ionization chambers are among the oldest and most common radiation detectors. They are the simplest kind of detector (see Fig. 3.5) and can be thought of as a polarized capacitor that drifts the ionization charges created by incoming radiation to the electrodes, where they are collected and the signal is read, as shown in Fig. 3.5a.

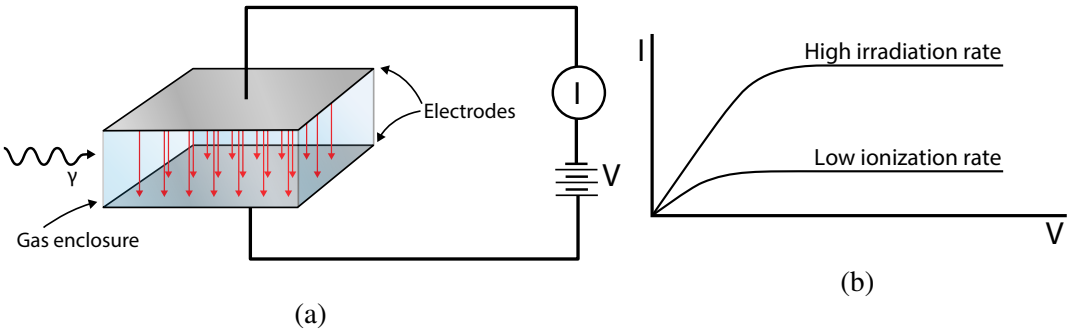

(a) (b)

Figure 3.5: Main components of a ionization chamber (a) and its response for different radiation fluxes (b). Figures adapted from [34].

The plateau shown in Fig. 3.5b represents the saturation current, where the electric field in the chamber is strong enough to separate the electron from their ions and therefore avoiding recombination. The saturation voltage depends on different factors, and the volume recombination is the most important for higher radiation intensity, demanding stronger electric fields, which means higher voltages, as shown in Fig. 3.6. Factors like temperature and pressure are also essential since the thermal diffusion and the mean free path depend on them.

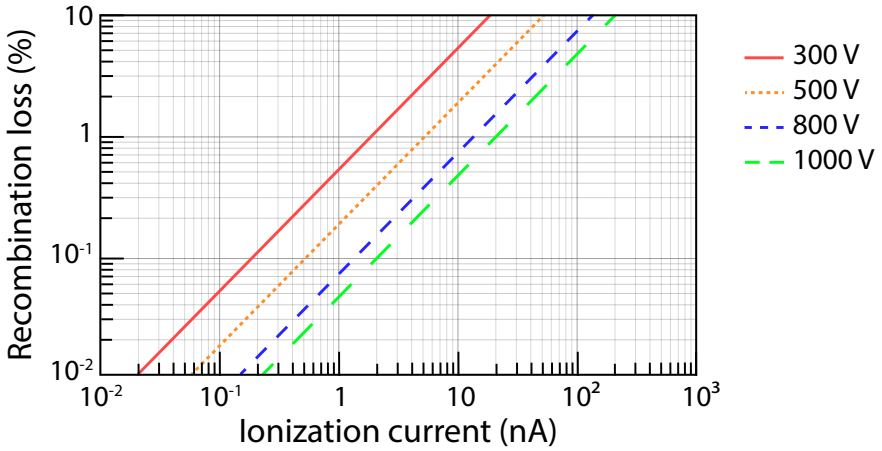

Figure 3.6: Recombination loss for different voltages applied to a given ionization chamber. Adapted from [34] (data from [54]).

There are several different applications for ionization chambers such as diagnostic measurements, radiation survey instruments, portable dose monitoring, smoke detectors, etc. Since it is an extremely simple and inexpensive detector to build, it can be applied essentially to almost any application, respecting its limitations, for example: the low current, which demands a reliable (and low-noise) current measurement system, the necessity of a stable high voltage supply, and its vulnerability to atmospheric conditions [33].

3.4 Proportional Counters

Proportional counters are detectors where the signal collected are boosted by means of the avalanche multiplication process. The challenge regarding these detectors is to provide a multiplication that is proportional to the initial charge, so the charge information of the incoming radiation is not lost, as in the case of the Geiger-Muller counters. It is normally obtained through formatting the electrical field so that the avalanche process happens in a well-defined geometric region, thus, the incoming ions are multiplied by the same amount every time.

3.4.1 Avalanche multiplication

As discussed before (see section 3.1.1), the external electric field promotes the drift of the charges. Because of the difference in mass, the electrons gain much more kinetic energy than the ions, becoming much faster. When the external electric field is intense enough, the electron acquires the energy necessary to provoke another ionization, transferring virtually all its energy, a cascade effect takes place, known as *Townsend avalanche*. The

Townsend equation, below, gives the increase in the number of electrons per unit path length:

$$\frac{dn}{n} = \alpha dx \tag{3.17}$$

The α coefficient, called *first Townsend coefficient*, depends on the electric field strength. It worths noting that $\alpha = 1/\lambda$, which is, the inverse of the mean free path of the electron in the gas, being therefore proportional to the gas density. Integrating the equation 3.17 over a path, one obtains that

$$n = n_0 e^{\alpha x} \tag{3.18}$$

which highlights the importance of limiting the geometric area within which the avalanche occurs, for the case of proportional detectors, otherwise the amplification boost in the signal is dependent on the position of the initial ionization. The easiest way to produce the mentioned controlled avalanche is using a tubular geometry with an anode wire, as shown in Figure 3.7a.

As known from classical electromagnetism, the electric field for a charged wire decays with $1/r$, which means that it quickly rises approaching to smaller radius. Depending on the voltage bias applied, it can be enough to allow avalanche (see Figure 3.8), as in the case represented in Figure 3.7b and 3.7c, otherwise, the detector behaves as an ionization chamber.

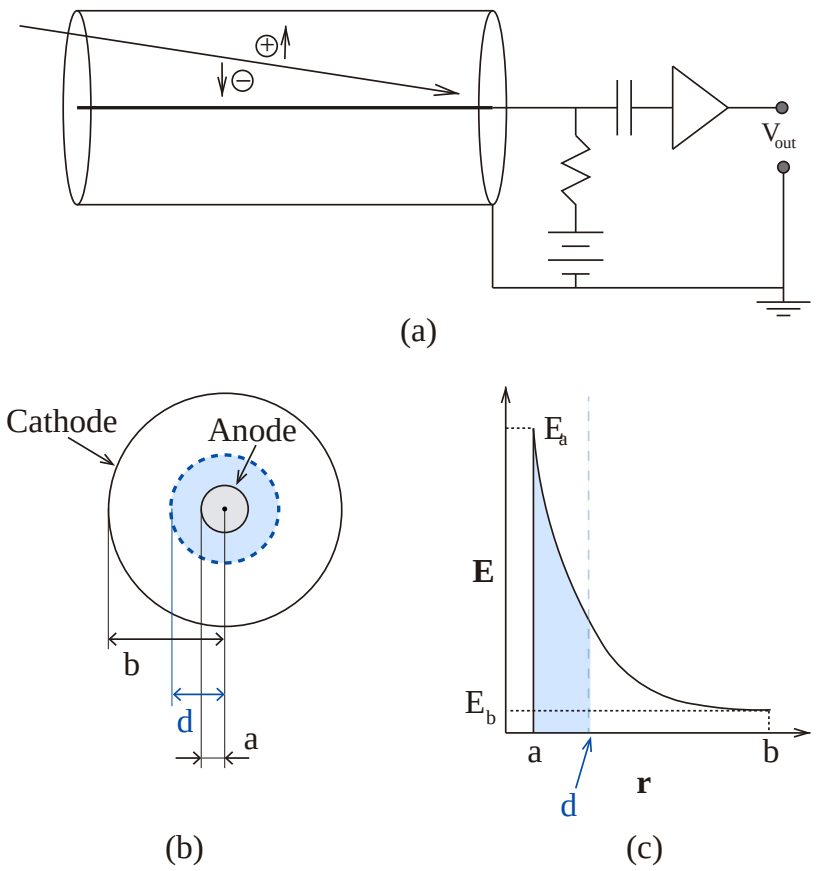

Figure 3.7: Scheme of a simple tube proportional detector (a), and its front view (b). There is a maximum diameter d below which the electric field is intense enough to produce Townsend avalanche, as we can see plotting the Eletric field strength as function of the radius r (c). Adapted from [33].

The avalanche process can be better visualized in Fig. 3.8, that shows a simulation of the avalanche cause by one single electron near the anode wire.

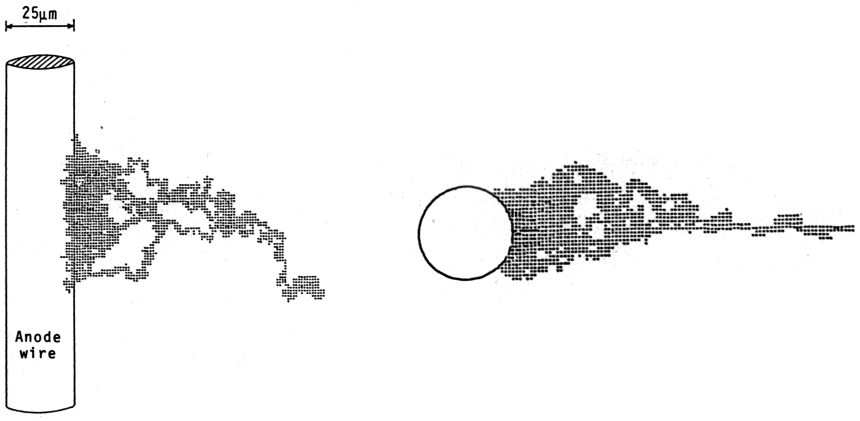

Figure 3.8: Monte Carlo simulation of Townsend avalanche produced nearby anode wire. Figure from [55].

3.4.2 Quenching

As presented before (see Figs. 3.2 and 3.3), the drift velocity for ions is around two orders of magnitude smaller than the drift velocity of the electron. It means that the electron's signal is already collected by the time the ion arrives at the cathode. When arriving, the ion charge can attract one extra electron from it if the difference between the ionization energy of the ion and the energy required to extract an electron for the cathode is enough. One possible consequence of this electron pulled out to the gas is generating a new undesirable signal in the detector. To solve this problem there are two types of quenching applied: external and internal.

The external quenching consists of varying the external electric field subsequently to the avalanche, avoiding the formation of new avalanches. In the cases where the detector is polarized with a positive voltage, such as Geiger tubes, one can carry it out by adding a significant resistance between the voltage supply and the anode in order to require a reasonable amount of time until the detector comes back to its default settings. The disadvantage of this method is the rise of the dead time of the detector.

The internal quenching consists in promoting the transfer of the positive charge to a molecule by adding a molecular gas in the detector, called quench gas, in a proportion usually between $5\,\%$ and $10\,\%$. By choosing an adequate molecule, the extraction of this extra electron is suppressed. This happens because the extra energy that would be used to extract the electron from the cathode is divided into different forms of excitation that a molecule presents, avoiding subsequent avalanches.

3.4.3 Multi Wire Proportional Chamber (MWPC)

The multiwire proportional chamber is a planar detector with several anodes, introduced by George Charpak in the late 60's [25], illustrated in Fig. 3.9. The anodes deforms the original parallel eletric field between the cathodes at the top and bottom of the structure, as shown in Fig. 3.10, starting an Townsend avalanche when electrons reach the near region around the wires, same process already discussed for the tube proportional detector.

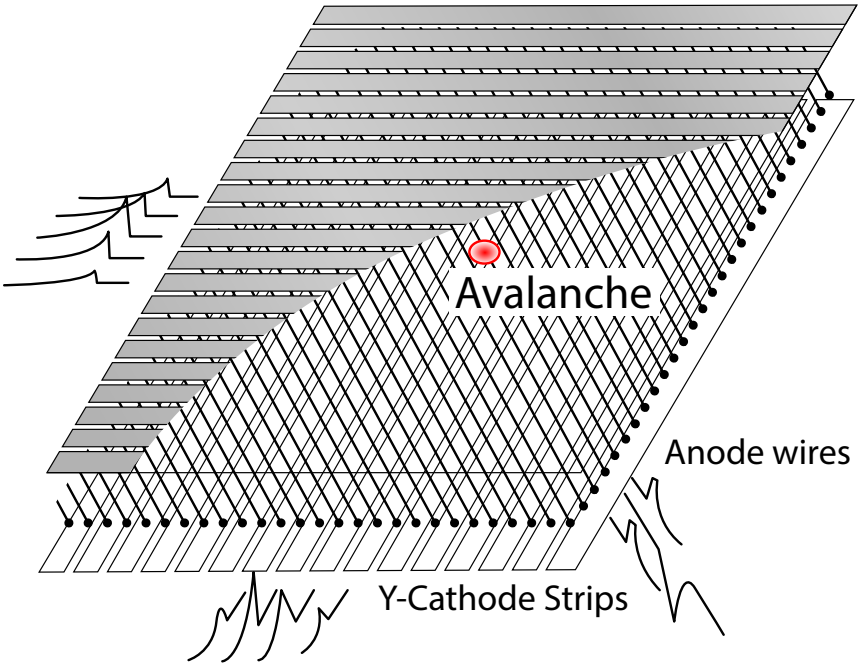

Figure 3.9: Skecth of a MWPC detector, showing the signals in the anode wires, and cathode strips given by an avalanche. Adapted from [56].

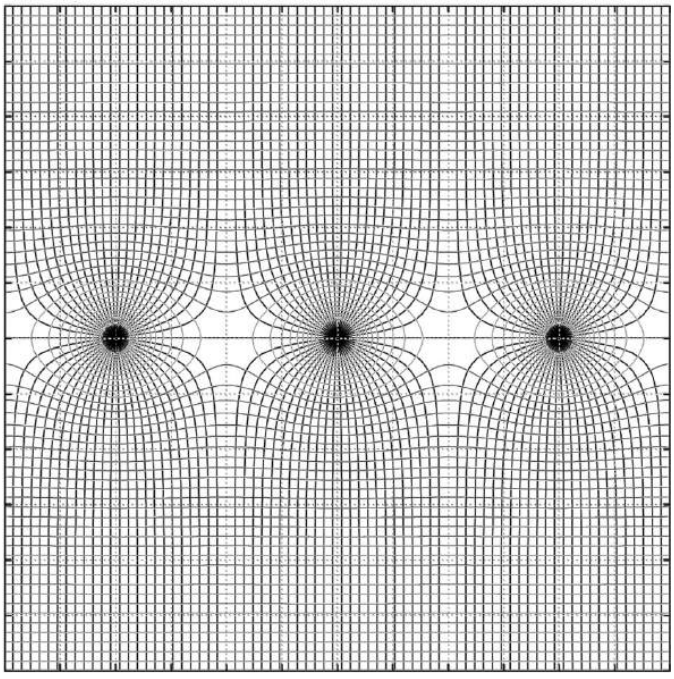

Figure 3.10: Electric field lines and equipotential lines (dashed) in a MWPC. Figure from [47].

The main advantage of this kind of detector is the better position sensitivity with fair resolution, since the position of the avalanche can be recovered by using center of gravity

algorithms with the signals from the X and Y direction cathodes and the anode wires. The pitch limitation for the wires is about $1\,\mathrm{mm}$ and their diameter about $20\,\mu\mathrm{m}$. Using multiple anodes wire allows, besides its application over large areas, a faster response for this detector (in some cases smaller than $1\,\mathrm{ns}$ [57]) and the indenpendent reading of the wires. Georges Charpak won the Nobel Prize for developing this detector, which was responsible for major advances in accelerator physics.

3.5 Micropattern Gaseous Detectors

The micropattern gaseous detectors (MPGDs) are fabricated using detailed small structures that demand precision techniques such as photolithography, laser machining, and etching of specific well-determined areas. They emerged at the beginning of the 1990s and became well-known and robust over the years. In this section, we will briefly discuss the most common micropattern gaseous detectors.

3.5.1 Micro Strip Gas Chambers (MSGC)

The first micropattern gaseous detector was the Micro-strip gas counter (MSGC) introduced by Anton Oed in 1988 [53] who transposes the MWPC idea for a substrate. Instead of the wires, it uses etched metallic trails to form the electric field near the bottom of the detector, provoking the avalanche. A sketch of the geometry and the electric field lines can be seen in Fig. 3.11.

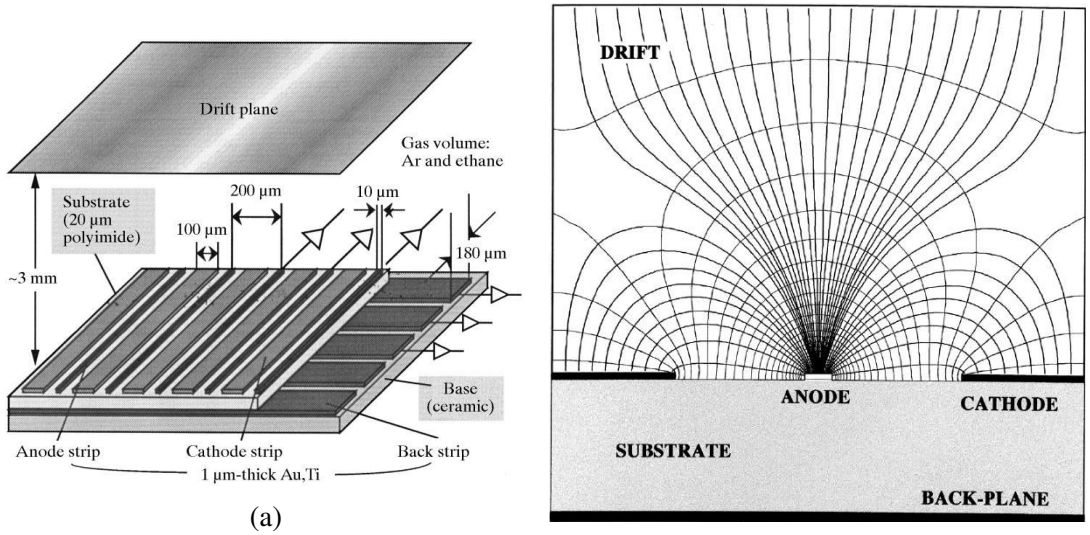

(a) (b)

Figure 3.11: Sketch of a MSGC, highlighting some of its structures (a), Figure from [58]. The resultant electrif field and equipotencial lines produced by the trails (b), Figure from [47].

The anodes have $10\,\mu m$ wide and are distributed with $200\,\mu m$ pitch, alternated with wider cathodes. These trails are etched and fixed on top of a $20\,\mu m$ polyimide film, which separates them from the back strips, positioned perpendicularly. With the signal from both strips, one can reconstruct the position. The typical range of gain[2] is around 10^3 to 10^4 [47].

3.5.2 Micro Mesh Gaseous Structure (MICROMEGAS)

The Micromesh gaseous structure (MICROMEGAS) is another widely used MPGD introduced by Yannis Giomataris in 1996 [28], consisting of a metallic mesh suspended near over the anode strips. The mesh structure is strongly biased, creating an electric field around the holes that trigger the avalanche mechanism. A sketch of the MICROMEGAS working principle is pictured in Fig. 3.12a.

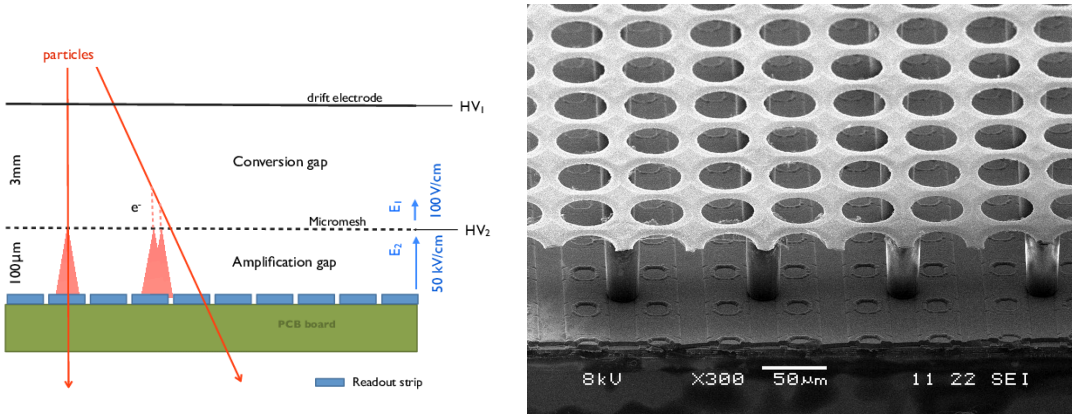

(a) (b)

Figure 3.12: Example of MSGC, with some geometrical and electric specifications (a), Figure from [59]. Scanning Electron Microscope (SEM) image highlighting the mesh. In this case, the structure is being used on a Timepix readout and the mesh is covered with a photocathode layer (b), Figure from [60].

Some applications require limitations regarding the ion-backflow (IBF), defined as the ions current from the avalanche that drifts towards the cathode. These detectors present relatively low ion-backflow since most of the ions are collected in the mesh, and the maximum gain reachable is bigger than 10^5 [47]. It is also possible to obtain position resolutions between $10\,\mu m$ and $15\,\mu m$, given the proper conditions [34].

[2]by definition, the gain of a given detector is the amount of charge collected divided by the amount of charge generated by the radiation within the sensitive area of the detector.

3.5.3 Gas Electron Multiplier (GEM)

The Gas Electron Multiplier was introduced by Fabio Sauli in 1997 [26]. This microstructure consists of a $50\,\mu\mathrm{m}$ polyimide foil copper-coated on both sides, double etched with a pattern of holes. The final result of this process is shown in Fig. 3.13a. The holes are double conical (that is also helpful to avoid discharges) and have $50\,\mu\mathrm{m}$ inner diameter and $70\,\mu\mathrm{m}$ outer diameter. They are equally spaced by $90\,\mu\mathrm{m}$ (small pitch), $140\,\mu\mathrm{m}$ (standard pitch), or $280\,\mu\mathrm{m}$ (large pitch).

By applying a voltage between the bottom and top layers of the GEM, electric fields are produced in space so that the resulting field (sum of the external electric field with the electric field generated by the GEM) becomes highly intense inside the hole (see Fig. 3.13b), inducing the avalanche process.

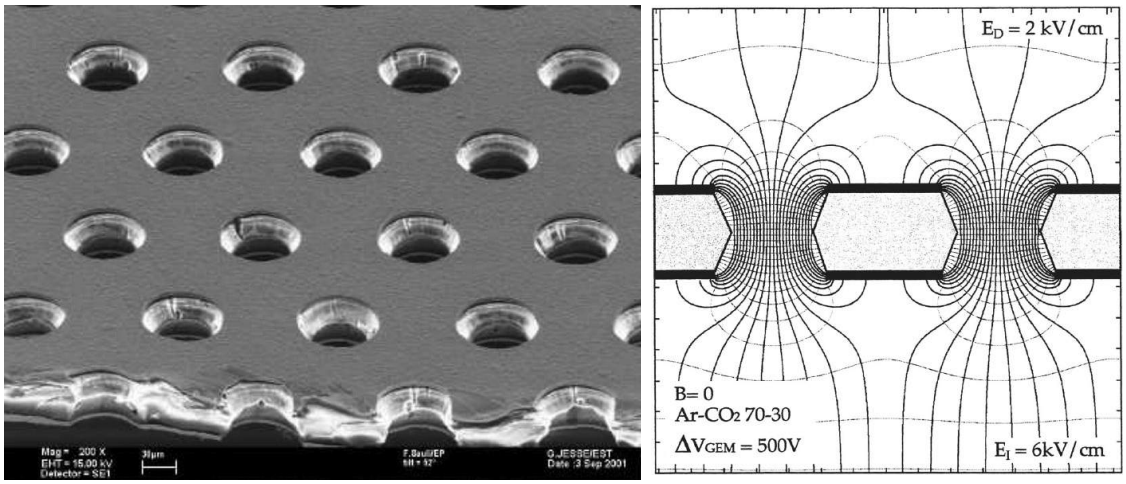

(a) (b)

Figure 3.13: SEM image of a GEM foil (a) and the produced electric fields with its respective equipotential lines. Figures from [47].

This kind of microstructure is interesting because it can work in cascade mode, making it possible to reach very high gains using more than one layer. The detector's gain is the number of electrons collected in the anode divided by the number of primary electrons generated by incoming radiation and depends on several factors, such as the geometry of the detector, the gas composition and its temperature and pressure, as shown in Fig. 3.14.

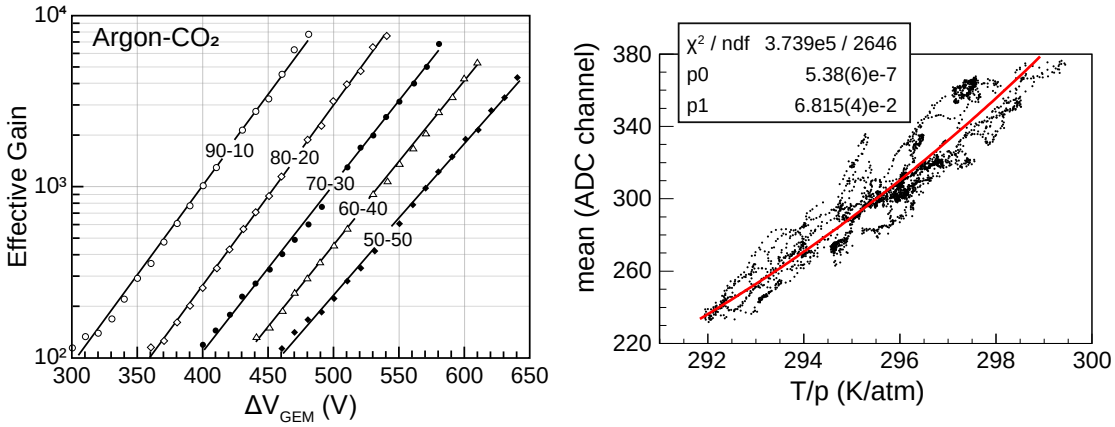

(a) (b)

Figure 3.14: Single GEM effective gain for different gaseous mixtures of $ArCO_2$ (a) and the gain dependance on the ratio between temperature and pressure (b). Figures adapted from [61] and [62], respectively.

These detectors are also suitable for large areas applications and have been used in several experiments such as ALICE [63], CMS [64], COMPASS [65], neutron detection [66, 67], muon tomography [68], medical dosimetry [69], etc, and present several advantages regarding the MWPC, considered their predecessors. Some advantages are the low IBF, which is the number of ions from the amplification that enters the drift zone, better energy resolution, and higher operational stability [63].

Chapter 4

Detector characterization

The previous chapters discussed how radiation interacts with matter and the key concepts regarding gaseous detectors. When designing and building a position-sensitive gaseous neutron detector it is necessary to understand some concepts to characterize it. For this work, three essential concepts are discussed: spatial resolution, which quantifies the ability of the detector to produce detailed images; efficiency, which characterizes its sensitivity to neutrons; and geometric calibration, to provides a length scale for the obtained neutron images.

4.1 Spatial resolution

The spatial resolution is related to the capacity that a system has to distinguish between different points, generally near each other. The higher this capacity, the better one can discriminate closer points. We can also state this definition as the ability of the system to resolve image details [70]. Therefore, spatial resolution is an essential characteristic for any position sensitive detector since different applications demand different spatial resolutions of the system.

We use the called *spread functions* to characterize and quantify this property. There are three spread functions used to this intent that will be discussed in detail: the point spread function (PSF), used with the image of points, the line spread functions (LSF), used with the image of slits, and the edge spread function (ESF), used with the image of edges.

4.1.1 Point spread function (PSF)

The *point spread function* is the mathematical function that describes the detector response to a point-like source of radiation. For most detectors, this function has a Gaussian-

like shape. Even in the case it is not perfectly Gaussian, one can assign to this curve a gaussian-equivalent in order to extract its full width at half maximum (FWHM), the fundamental quantity from which we obtain the spatial resolution.

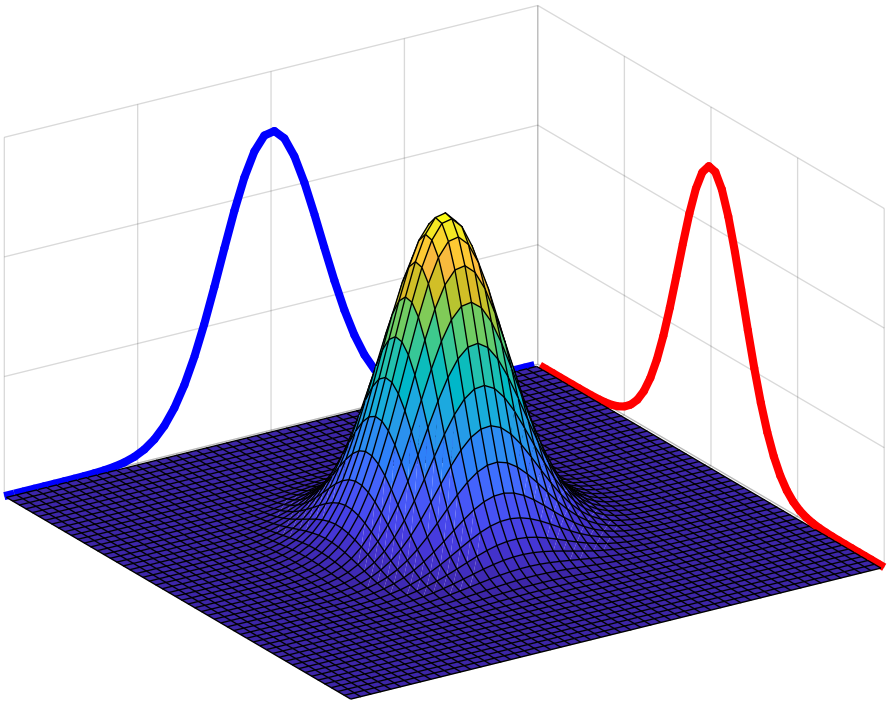

Figure 4.1: The plot of a typical PSF function, a 2D Gaussian, with its projections in both X and Y directions. The Z-axis represents signal intensity collected by the detector. The sharper this peak, the better is the detector's spatial resolution. To enhance the projections visualization (blue and red curves), they were plotted using a different vertical scale from the surface plot.

The PSF is related to the spatial resolution because when approaching two point-like sources (the geometrical simplest possible source shape), the tails of these curves superimpose, affecting one's ability to distinguish between the two. If the approximation is smaller than the spatial resolution, they become indistinguishable. This effect is shown in Figure 4.2.

For the reason described above, the FWHM commonly quantifies the spatial resolution since two gaussian PSFs separated by one FWHM between each other are still distinguishable, as shown in Figures 4.2c and 4.3b. This consideration is still valid if the PSF is not a gaussian. In this case, we consider the gaussian-equivalent response, and the same reasoning applies: the spatial resolution equals the FWHM of the gaussian-equivalent response of the detector.

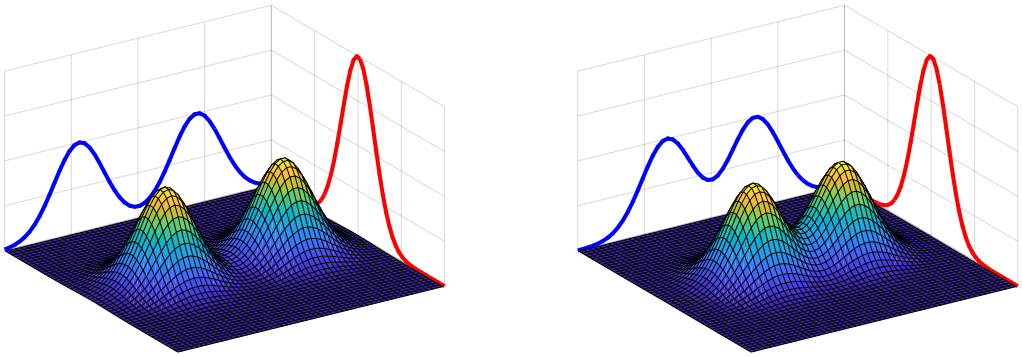

(a) (b)

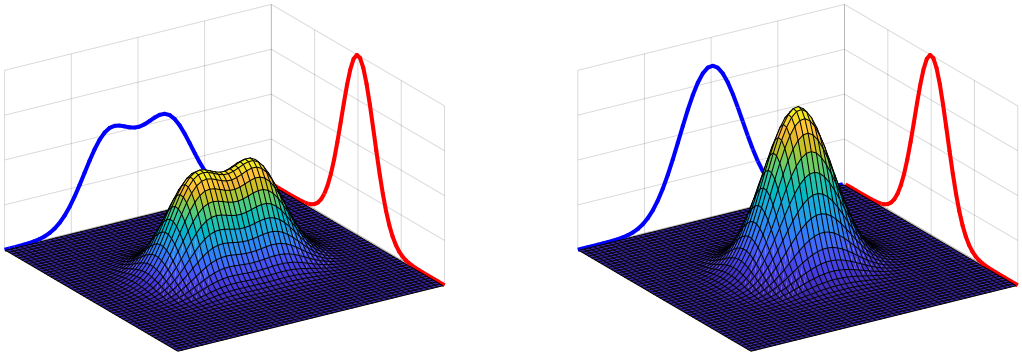

(c) (d)

Figure 4.2: Two gaussian PSFs with respective (rescaled) projections in X and Y separated between each other by 2.0 FWHM (a), 1.5 FWHM (b), 1.0 FWHM (c) and 0.5 FWHM (d).

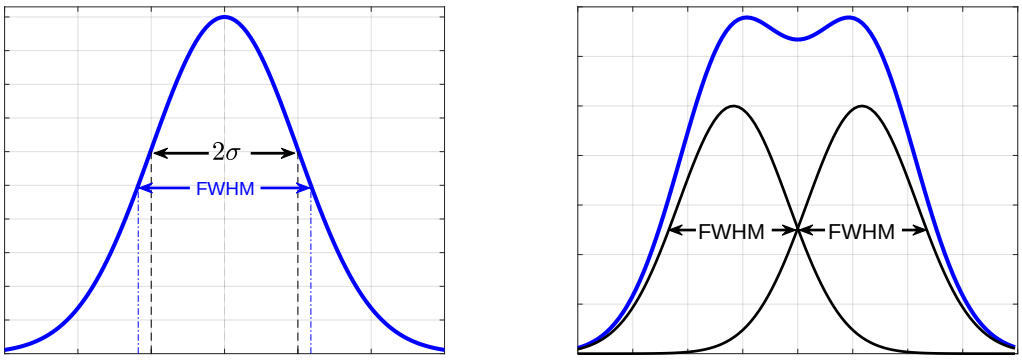

(a) (b)

Figure 4.3: Profile of gaussian PSF showing the relationship between σ and FWHM (a). Two Gaussian PSFs (black) spaced between each other by 1 FWHM and its response (blue, rescaled for easy visualization)(b).

The Gaussian PSF can be described as

$$f(x) = \frac{1}{\sqrt{2\pi\sigma^2}}\exp\left(\frac{-(x-x_0)^2}{2\sigma^2}\right). \tag{4.1}$$

By construction, the FWHM is the distance between the points that satisfies

$$f(x) = \frac{1}{2}f(x_0),$$

which means that

$$\text{FWHM} = 2\sqrt{2\ln(2)\sigma^2} \approx 2.355\sigma. \tag{4.2}$$

One can use the PSF to measure the resolution of the detector. Rigorously, it is impossible to generate an ideal point-like radiation source. Still, it is commonly possible to produce a near-ideal point-like radiation source which response can be considered the PSF itself. For this project, we applied this method by illuminating the detector through small diameter holes. The PSF also has theoretical importance since we start with points to construct other shapes. The following sections will discuss this idea in more detail.

4.1.2 Line spread function (LSF)

Analogously to the PSF, the line spread function (LSF) is the mathematical function that describes de detector's response to a linear source. This function can be obtained by combining infinite PSFs, the same way that to generate a line, we combine infinite points. This idea, despite simple, is illustrated in Figure 4.4.

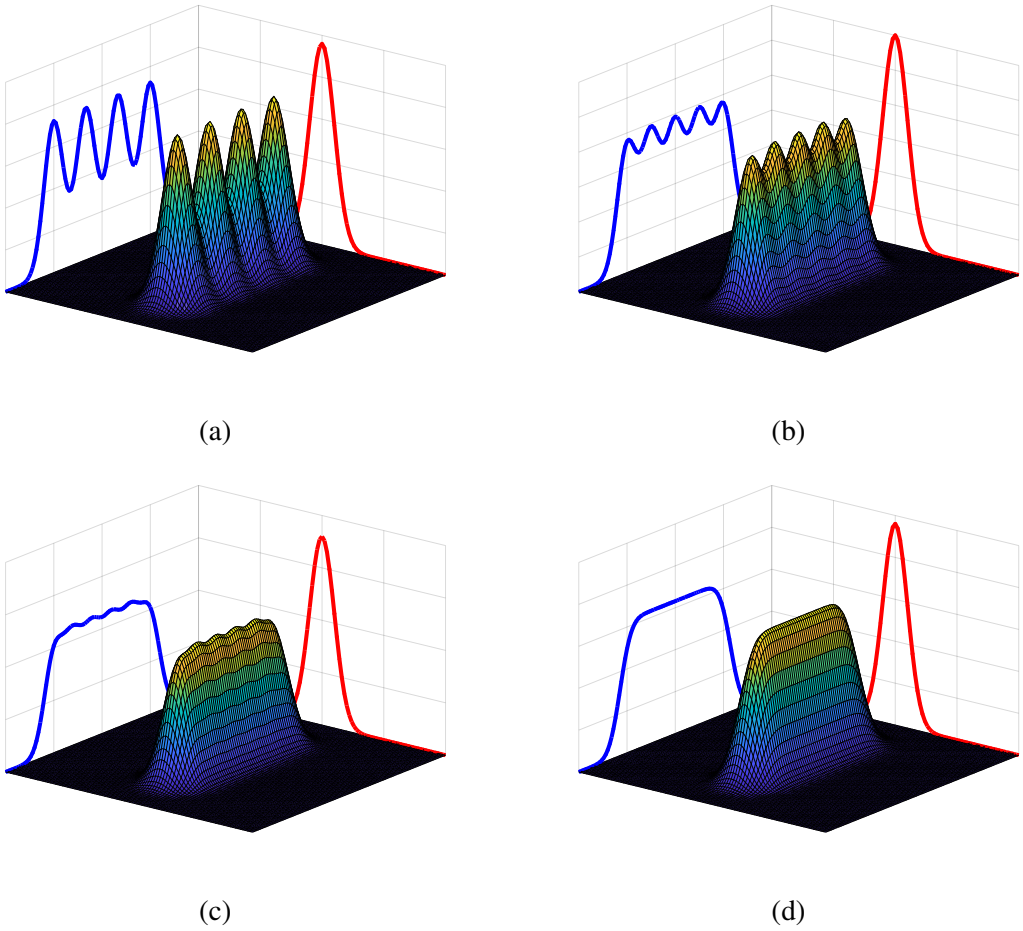

(a) (b)

(c) (d)

Figure 4.4: The sequence of PSFs with increasingly closer distance to each other and its projections (curves in red and blue) in both directions. We distributed 4 functions (a), 5 functions (b), 6 functions (c) and 8 functions (d) with same FWHM within the same length.

Since the LSF can be obtained from a set of aligned points very close to each other, the FWHM of the narrower projection (red curves in Fig. 4.4) equals the spatial resolution of the detector. However, this approach becomes quite complicated in practice because of the difficulty of building a slit thin enough. If producing the slit is possible, the acquisition time remains too large because of the small area.

4.1.3 Edge spread function (ESF)

The ESF can be produced by summing up parallel LSFs extremely close to each other, as shown in Fig. 4.5, which is analogous to the way a plane is created by summing up lines. Its projection is a step commonly described by the ERF function (the integral of the Gaussian function). This is the most useful function because it can be obtained experimentally using absorbers with sharp edges in front of the neutron beam.

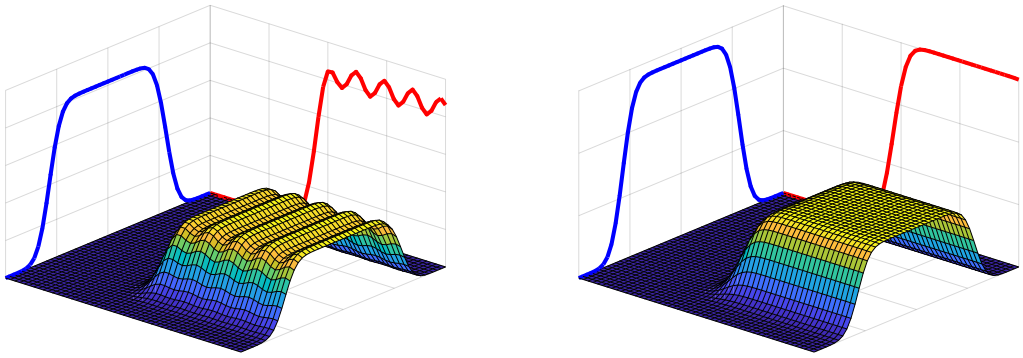

(a) (b)

Figure 4.5: The construction process of the ESF function (b) by summing up many LSF functions (a).

4.2 Efficiency

The detection efficiency of a detector is defined as its capacity to detect radiation of interest when exposed to a certain amount of radiation. In this case, considering that we are exposing the detector to a neutron beam, its detection efficiency will be $100\,\%$ in case all neutrons are detected and $0\,\%$ in case no neutrons are detected (in this case, one could not call it a detector). The prototype detector developed in this work uses $^{10}B_4C$ as converter material to detect neutron. This material was deposited on aluminum forming a $2.2\,\mu m$ thick layer. In the following discussion we evaluate the expected efficiency for the converter layer we used.

As discussed before, the neutron beam flux is exponentially attenuated when traveling a neutron-converting material, as shown in Equation 2.19. This attenuation happens because some neutrons are captured, producing detectable products (see Eq. 2.12). To evaluate the detection efficiency, one needs to get the total number of converted neutrons and consider the share which generates a detectable signal. In other words, we need to consider just the neutrons whose products can exit the depositon layer. The first step is to calculate the macroscopic cross-section Σ, using Eq. 2.15 together with

$$N = a\frac{\rho}{M}N_A, \tag{4.3}$$

where a is the stoichiometry of ^{10}B in a $^{10}B_4C$ deposition, which is approximately 4. Using also $\rho_{(^{10}B_4C)} = 2.3\,g\,cm^{-3}$ [71], $\sigma = 2991\,b$ [44] and $M_{B_4C} = 52\,g\,mol^{-1}$ as input, we obtain $\Sigma = 319\,cm^{-1}$. The amount of captured neutrons after traveling through a thickness l of material is given (using Eq. 2.19) by

$$\varepsilon_c = 1 - e^{-\Sigma l}. \tag{4.4}$$

Considering our $^{10}B_4C$ target, that has thickness of $2.2\,\mu m$, the capture efficiency $\varepsilon_c \approx 6.77\%$.

As mentioned, not all captured neutrons generate detectable products. Given that, to be detected these products have to cross the deposition to reach the gaseous volume, then generate a minimum amount of charge. This translates into the geometric constraint shown in Figure 4.6. In addition to some acquisition electronics parameters, the electronic noise determines the minimum amount of energy the system can detect. With this, we set the radiuses τ_α and τ_{Li} as the average distance the alpha particle and lithium nuclei travel to spend almost all of their energy, remaining an amount of energy equal to the threshold energy, which is $110(25)\,keV$ for our detector. In other words, we only count the particles that reach the gas with the minimum energy to be detected.

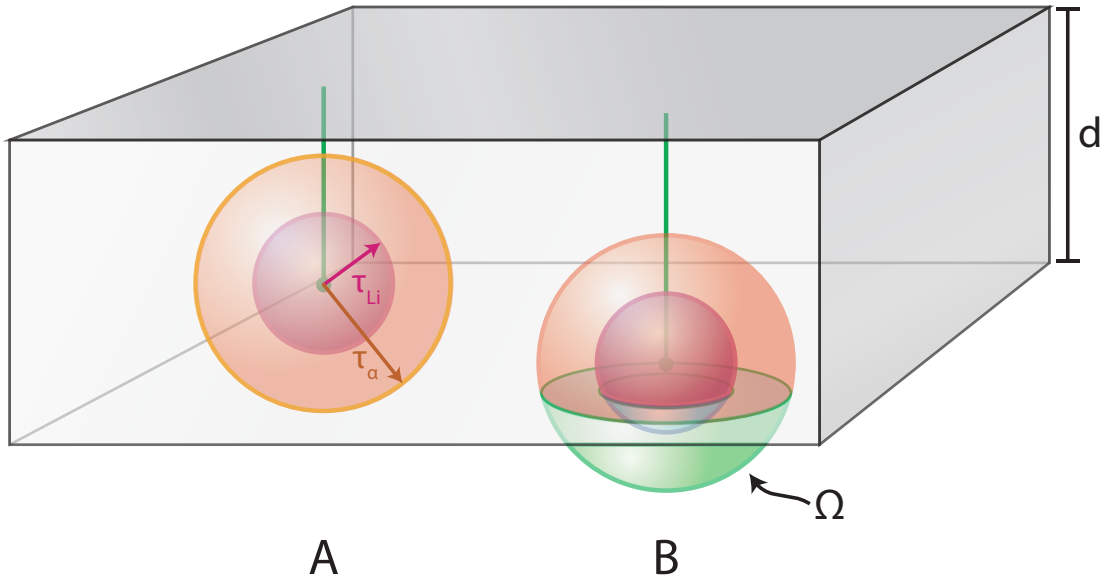

Figure 4.6: Representation of the region accessible to the products of the capture reaction, defined by spheres of radius τ_α for alpha particle and τ_{Li} for lithium nucleus, centered in the capture point (A). Depending on the position of the capture point, only the capture outcomes inside the solid angle Ω do cross the deposition and reach the gas (B).

The radiuses τ_α and τ_{Li} can be evaluated using the Stopping and Range of Ions in Matter (SRIM) software package [35], developed by James Ziegler and very helpful on calculating ion ranges in matter. It presents average $84\,\%$ accuracy for alpha and lithium ions [35]. As input for the SRIM simulations we used the composition reported on [72] for the $^{10}B_4C$ deposition over aluminum. For each of the four capture products (shown in

Eq. 2.12), 50 000 ions were calculated, generating the average stopping power curve of Fig. 4.7, whose integral gives the deposited energy shown in Fig. 4.8. By definition, the remaining energy after traveling some distance x equals the ion initial energy subtracted by the deposited energy (Fig. 4.8); this result is shown in Fig. 4.9.

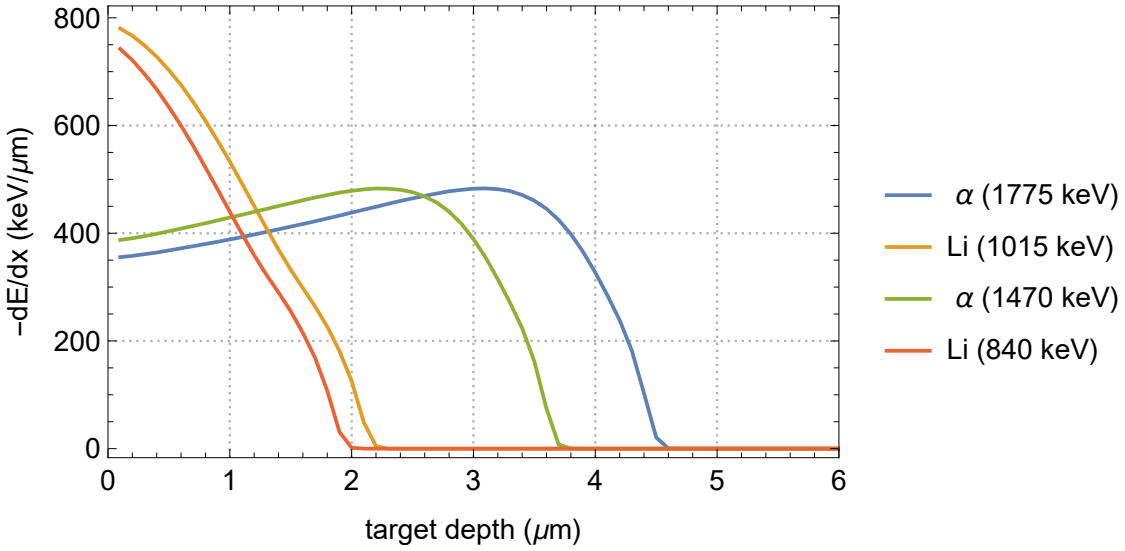

Figure 4.7: Stopping power as a function of the distance travelled in $^{10}B_4C$ target for each product of ^{10}B (n,α)^{7}Li thermal neutron capture reaction.

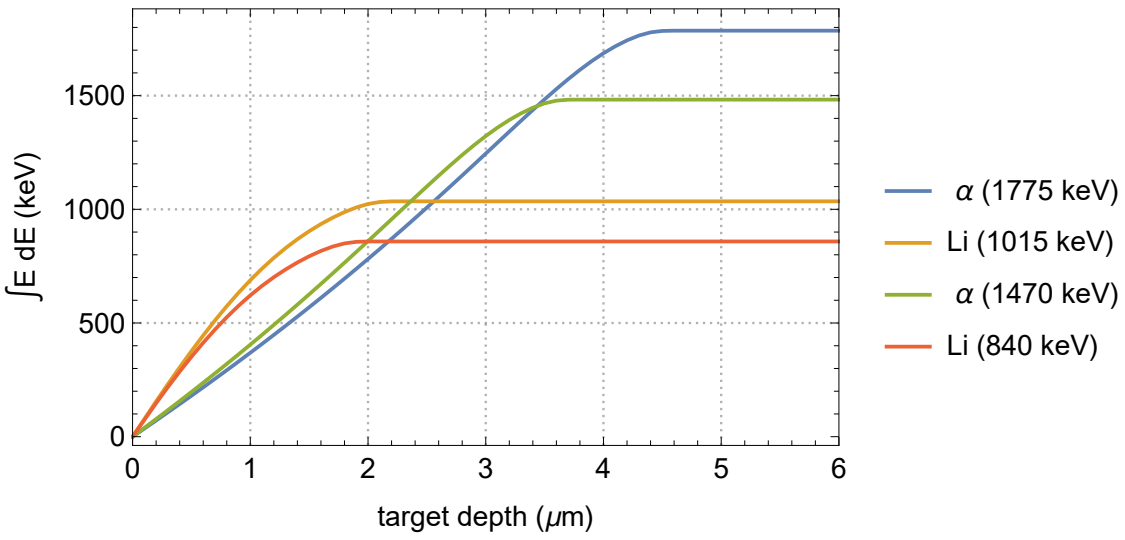

Figure 4.8: Energy deposited by the products of the ^{10}B (n,α)^{7}Li reaction as a function of the distance travelled in $^{10}B_4C$ target.

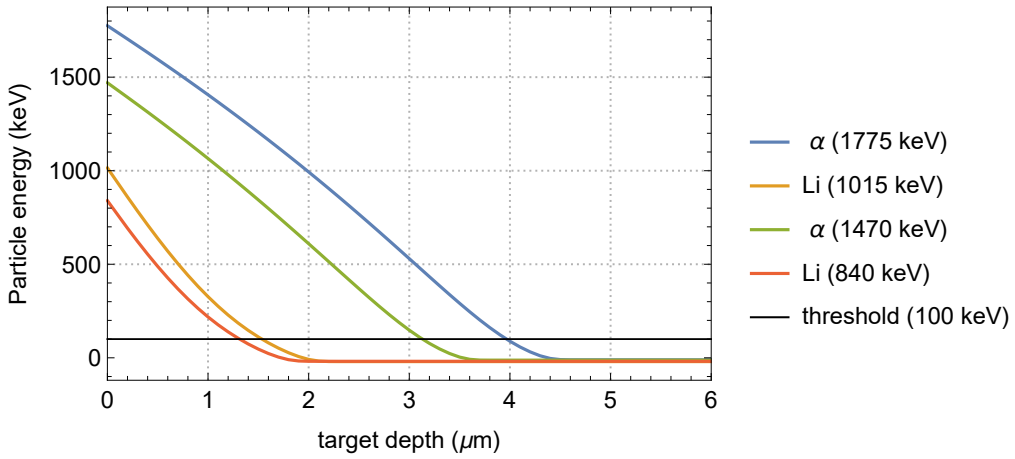

Figure 4.9: Remaining energy for each ^{10}B (n,α)^{7}Li reaction product as a function of the distance travelled in $^{10}B_4C$ target. The τ values used for the calculations are the depth in which the particle's remaining energy equals the threshold. This condition gives: $\tau_\alpha(1775\,\mathrm{keV}) = 3.97\,\mu\mathrm{m}$, $\tau_\alpha(1470\,\mathrm{keV}) = 3.13\,\mu\mathrm{m}$, $\tau_{Li}(1015\,\mathrm{keV}) = 1.54\,\mu\mathrm{m}$ and $\tau_{Li}(840\,\mathrm{keV}) = 1.31\,\mu\mathrm{m}$.

The geometric constraint presented in Fig 4.6 implies that only the capture products that leave the reaction in the solid angle shown in light blue in Fig. 4.10, and indicated with Ω, will provide a signal in the detector. Note that since just the products that escape the material are detected, Fig. 4.6 show us that the solid angle Ω depends on the distance x between the point where the neutron was captured and the surface of converter layer. For instance, if the neutron is captured very close to the surface (which means x very small), the solid angle is the approximately the whole hemisphere of the sphere.

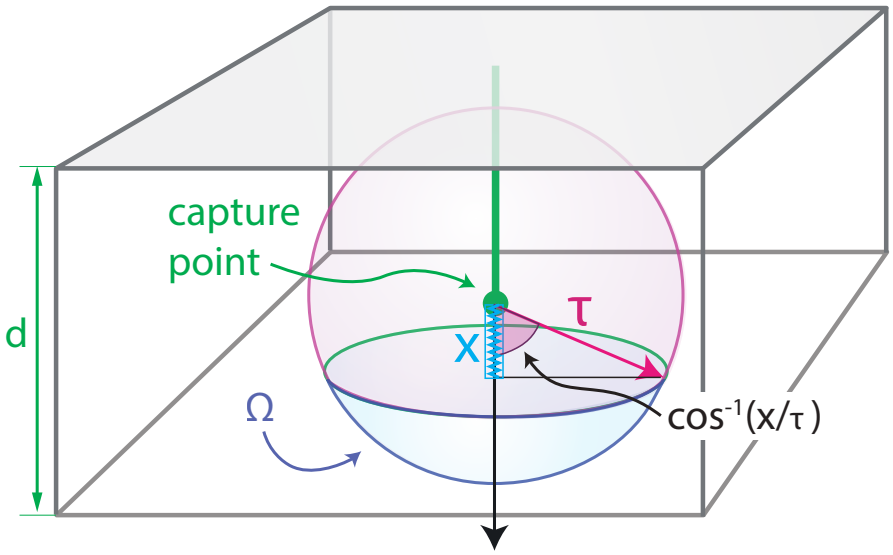

Figure 4.10: The solid angle Ω (light blue) is defined by the region limited by the angle $\cos^{-1}(x/\tau)$, where x is the distance between the point of interaction and the lower part of the deposition and τ the the particle average range in the deposition.

We can write the fraction F of detectable converted neutrons, for a determined product, as

$$F(d,\tau) = \frac{1}{4\pi}\int_0^d \int_0^{\cos^{-1}(x/\tau)} d\Omega dx, \tag{4.5}$$

where d in the deposition thickness. We can write the total fraction of detectable neutrons as

$$\begin{aligned} F_T(d) = 0.94\big(F(d,\tau_{\alpha(1470\,\mathrm{keV})}) + F(d,\tau_{Li(840\,\mathrm{keV})})\big) \\ + 0.06\big(F(d,\tau_{\alpha(1775\,\mathrm{keV})}) + F(d,\tau_{Li(1015\,\mathrm{keV})})\big), \end{aligned} \tag{4.6}$$

considering that the statistical composition of the neutron capture products follows Eq. 2.12, which gives $F_T(2.2\,\mu\mathrm{m}) = 47.7(44)\%$. We can evaluate the final detection efficiency by multiplying the conversion efficiency ε_c of Eq. 4.4 by the share of detectable ions $F_T(2.2\,\mu\mathrm{m})$, which results in:

$$\varepsilon = F_T\varepsilon_c = 3.22(18)\%, \tag{4.7}$$

where the uncertainty was derived from the uncertainties of thickness, F_t, and energy threshold.

Since ε depends on the thickness, this estimative can help find the optimal thickness for the deposition. The dependence is shown in Fig. 4.11 and indicates that the optimal thickness for one single layer is around $3\,\mu\mathrm{m}$.

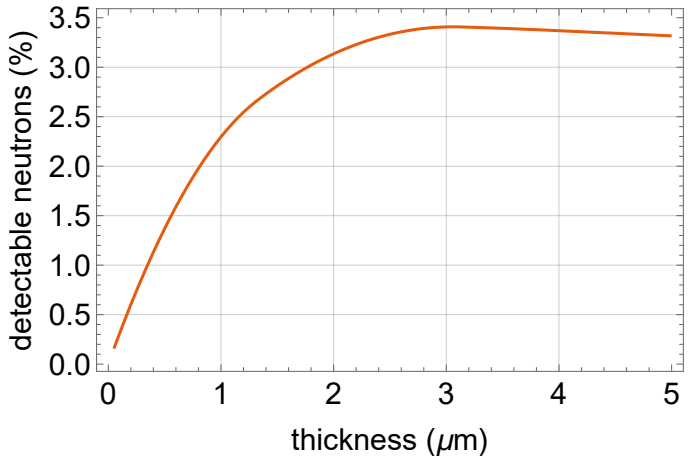

Figure 4.11: Detectable neutrons as a function of the deposition thickness, given by Eq. 4.7.

4.3 Geometric calibration and masks calibration

As introduced in section 4.1, the PSF, LSF, or ESF may evaluate the spatial resolution. However, this quantity should be measured with an adequate length unit (mm for our prototype). Therefore, it is mandatory to obtain the position calibration of the detector, which provides the correct dependence between an arbitrary unit and a known unit for spatial coordinates, allowing to locate events within the sensitive area of the detector.

We used cadmium masks with holes patterns for this task since this element has a huge neutron capture cross-section behaving practically as an ideal absorber above certain thickness. There was no need for high accuracy mechanical machining for the early tests stage, so the masks were handmade out of $\sim 1\,\mathrm{mm}$ thick cadmium foils and proved to be a simple way to perform initial tests quickly.

Nevertheless, it is still necessary to characterize their final geometric aspects since cadmium is a very soft metal susceptible to several small deformations. In other words, we need to know the position and the area of the holes drilled in cadmium. This informations was obtained by optically scanning the masks at $300\,\mathrm{ppi}$ resolution. They were scanned jointly with a calibration pattern shown in Fig. 4.12. The obtained images of all handmade masks are shown in Figs. 4.13, 4.14, and 4.15. In summary, the printed pattern allowed calibrating the handmade masks that were used to pre-calibrate our detector.

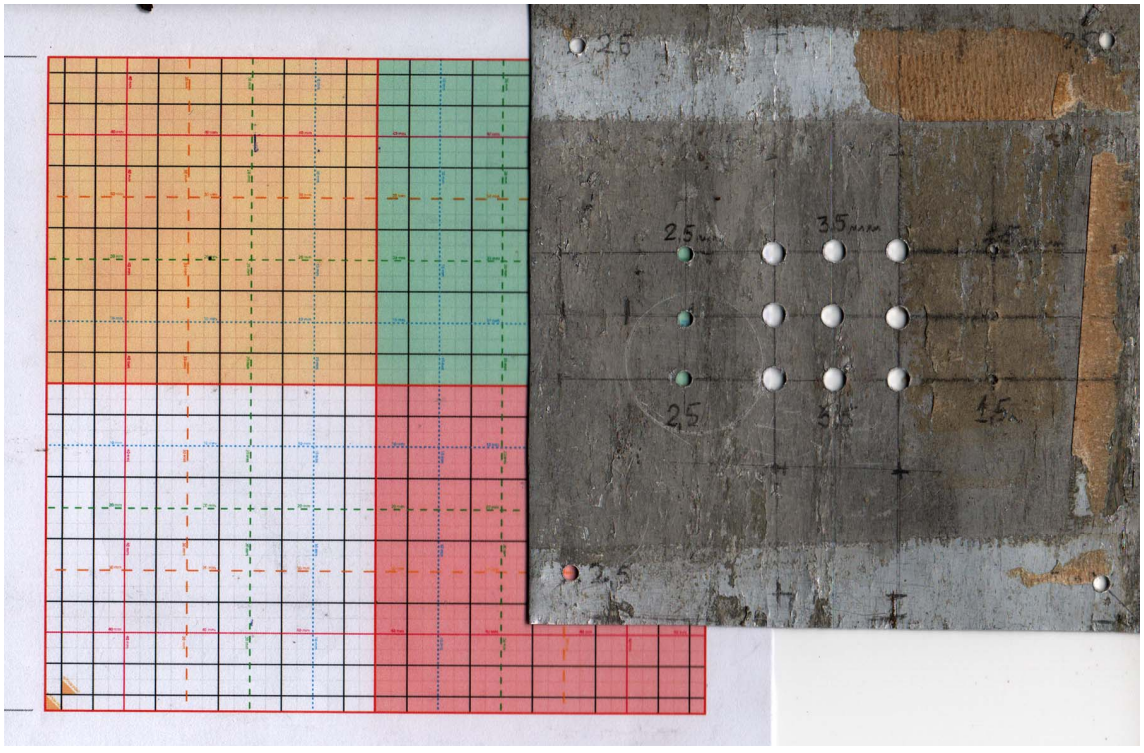

Figure 4.12: Scan of one of the cadmium mask together with the calibration pattern.

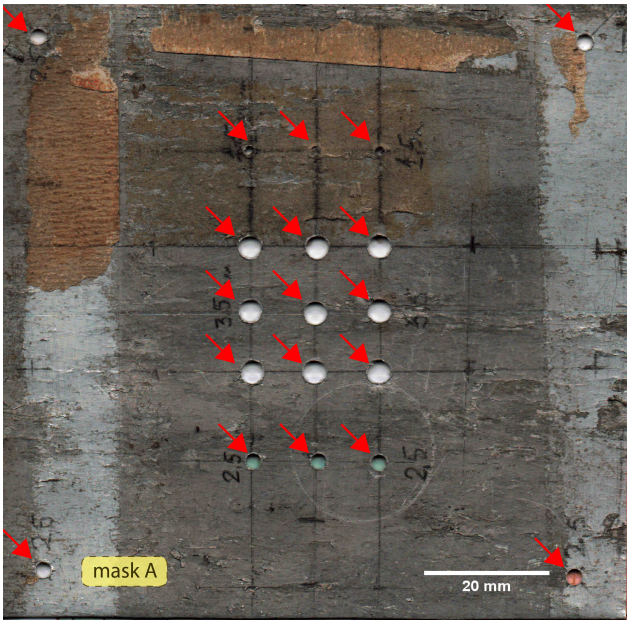

Figure 4.13: Cadmium mask with 19 holes of different sizes. There is a central 3×3 matrix with holes of $3.5\,\mathrm{mm}$ diameter. There are also 3 holes of $1.5\,\mathrm{mm}$, aligned at $15\,\mathrm{mm}$ above, and 3 holes of $2.5\,\mathrm{mm}$ diameter, aligned $15\,\mathrm{mm}$ below the matrix. In the corners we made 4 holes of $2.5\,\mathrm{mm}$. All holes are signed with a red arrow. This mask will be referred to as "mask A".

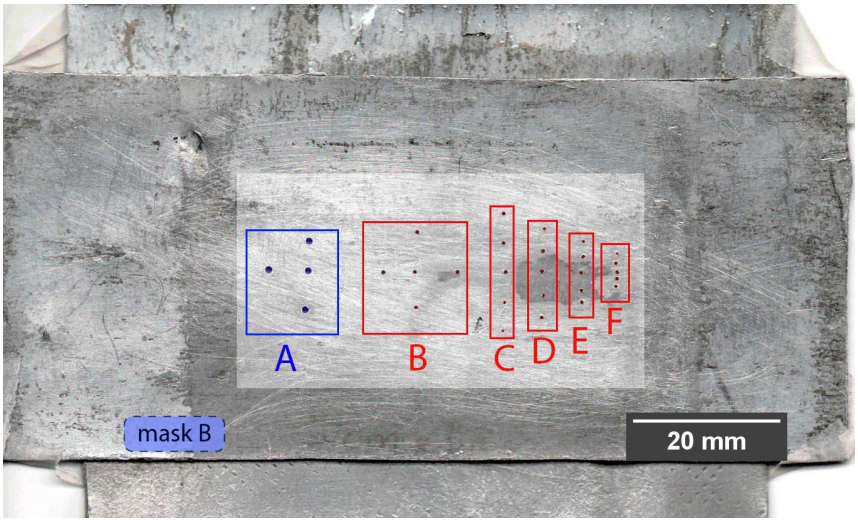

Figure 4.14: This was the mask with more holes. The are 19 holes in different areas. The holes of area A has $1.0\,\mathrm{mm}$ diameter, all the other holes have $0.5\,\mathrm{mm}$ diameter. The pitch between the holes of the areas F, E, D and C were meant to be $1.0\,\mathrm{mm}$, $2.0\,\mathrm{mm}$, $3.0\,\mathrm{mm}$, and $4.0\,\mathrm{mm}$. As it was drilled by hand, the precision in their position is not that good, which reinforces the need to scan the masks. This mask will be referred to as "mask B".

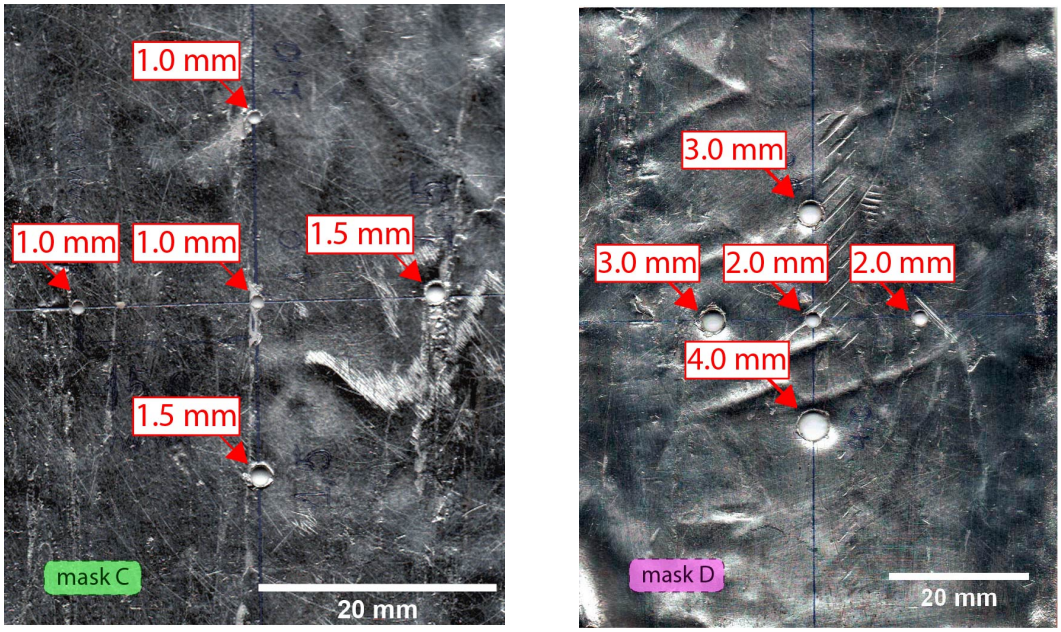

(a) (b)

Figure 4.15: Smaller masks with five holes each. One of them with holes of $1.0\,\mathrm{mm}$ and $1.5\,\mathrm{mm}$ diameters (a), which will be referred to as "mask C". The other mask with holes of $2.0\,\mathrm{mm}$, $3.0\,\mathrm{mm}$ and $4.0\,\mathrm{mm}$ diameters (b), which will be referred to as "mask D".

The calibration of the images was performed by obtaining the "calibration factor", defined as a given distance in pixels divided by its value in a standard length unit (such as millimeters). We used ImageJ, a consolidated program for analyzing scientific images [73], to obtain this factor, as illustrated in Fig. 4.16.

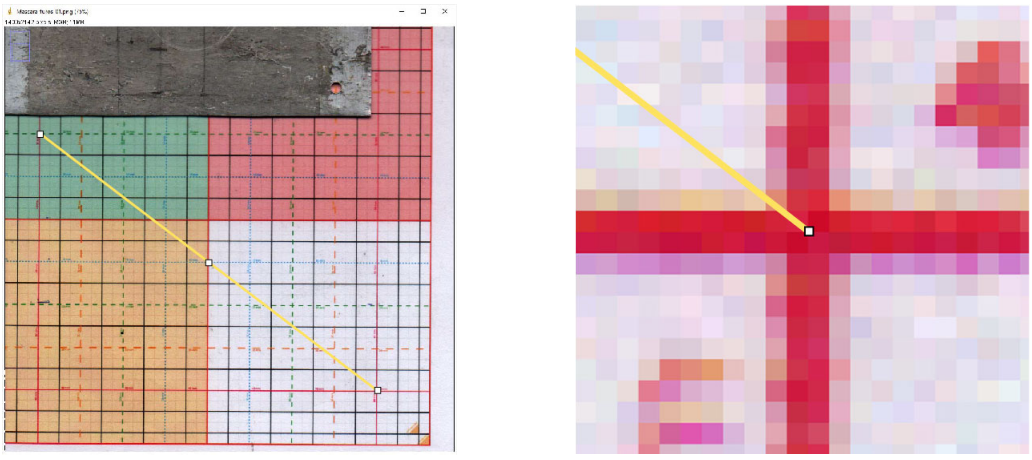

(a) (b)

Figure 4.16: Since the pixel aspect ratio of the scanned image is 1:1, we select points trying to maximize distance in the internal area of the calibration pattern (a). The program allows setting the calibration point in the intersection of pixels, which is interesting to locate the crossover of the perpendicular lines.(b).

Supposing the uncertainty of the scan process to be $1\,\mathrm{ppi}$, the calculated calibration factors was expected to be compatible with $11.811(39)\,\mathrm{px/mm}$, that is equal to $300(1)\,\mathrm{ppi}$. It was also reasonable to expect that 2 pixels encompass possible errors while defining the calibration distance in the program (see Fig. 4.16). The average calibration factor obtained for the set of all masks that we calibrated was $11.785(39)\,\mathrm{px/mm}$, compatible within one σ ($Z_{fac} = 0.47$) with the expected one. The comparison is evaluated using the Z-test:

$$Z_{fac} = \frac{|\mu_e - \mu_0|}{\sqrt{\sigma_{\mu e}^2 + \sigma_{\mu 0}^2}}, \tag{4.8}$$

where μ_e is the experimental average calibration factor value obtained, μ_0 is the expected value and $\sigma_{\mu e}$ and $\sigma_{\mu 0}$ the respective uncertainties.

After obtaining the calibration factor, the position and areas of the holes could be measured. This was done by drawing a circle over the image, that matches the hole in the mask. The program allows to extract its area and center, as shown in Figure 4.17.

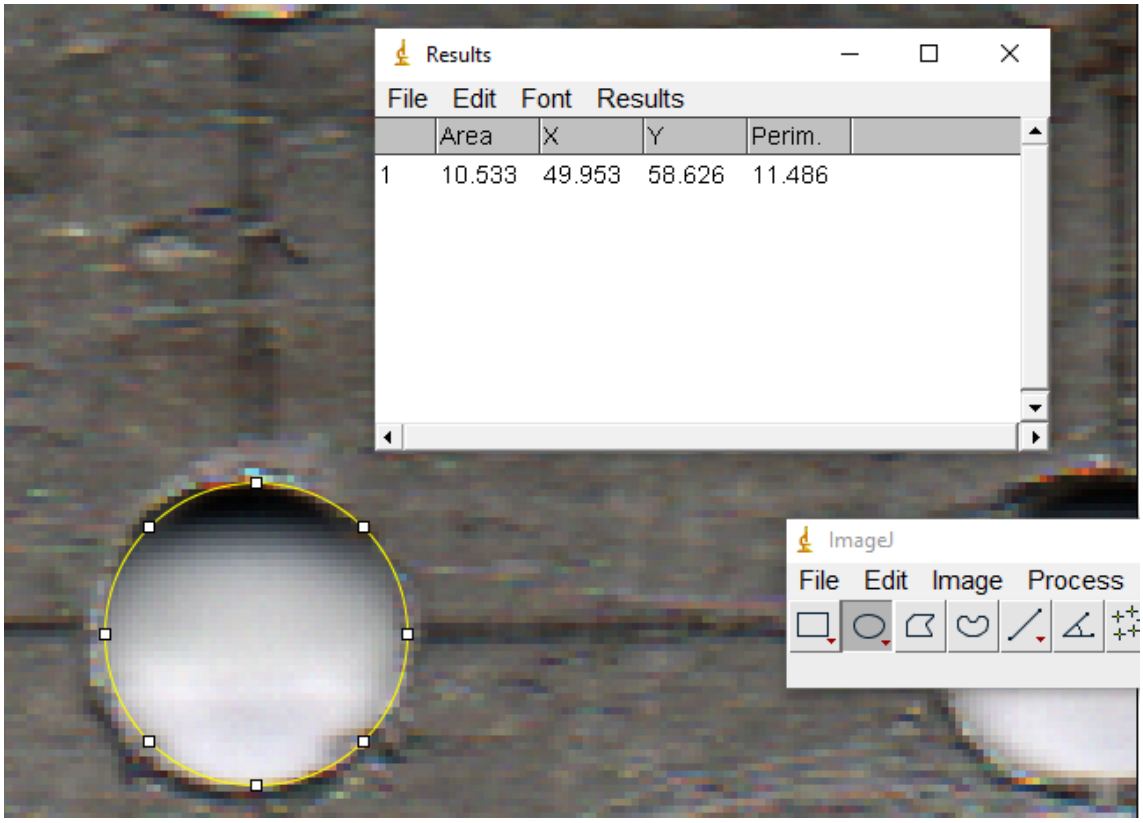

Figure 4.17: Method for extracting the area, center, and perimeter of a certain hole.

Only recently we were able[1] to access to the services of our Physics Institue mechan-

[1] because of the COVID-19 pandemic restrictions.

ical workshop, where was possible to fabricate a bigger mask ($125\,\mathrm{mm}\times125\,\mathrm{mm}$) with proper precision and quality. The dimensions of this new mask are shown in Fig. 4.18. As it was precision machined, we already knew its uncertainties are about some tenths of micrometer and consequently was no need to scan it.

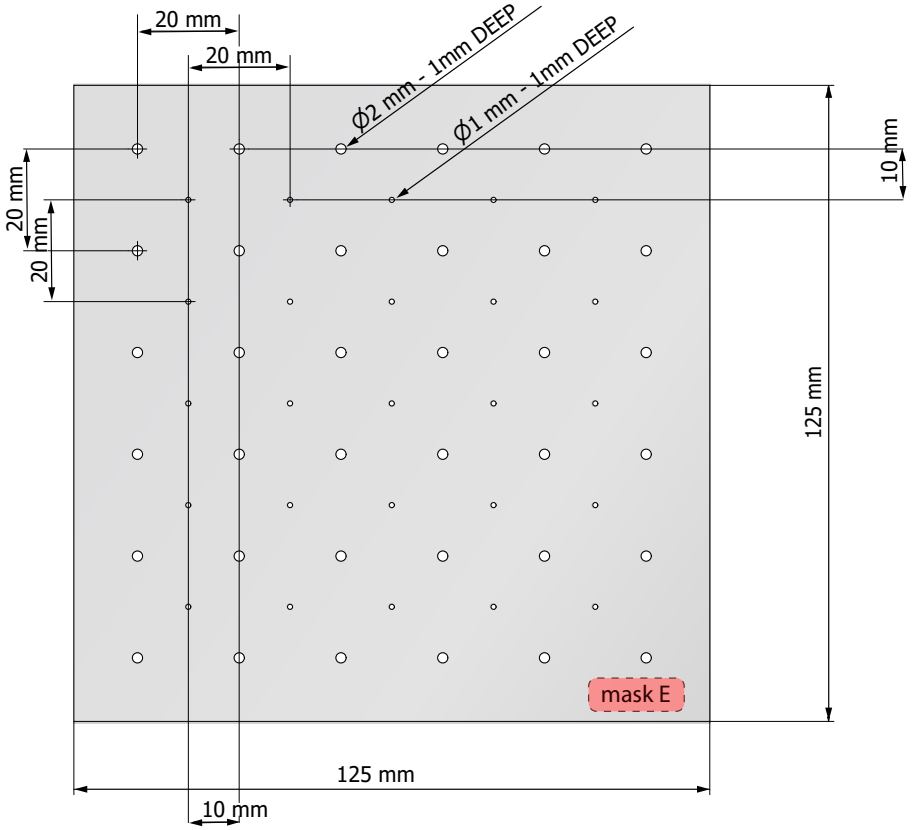

Figure 4.18: Project of a cadmium mask with holes pattern machined with proper tools. This mask will be referred to as “mask E”.

As mentioned, the scanning process provides us with correct information about the final position of the holes over the material for the hand-made masks. We use this information to generate the position calibration of the detector after producing the neutron image from these masks, taking care to acquire long enough to have a good amount of counts for each image. The first step of the process was to select sets of holes in the X and Y direction in the neutron image obtained, as shown in Fig.4.19.

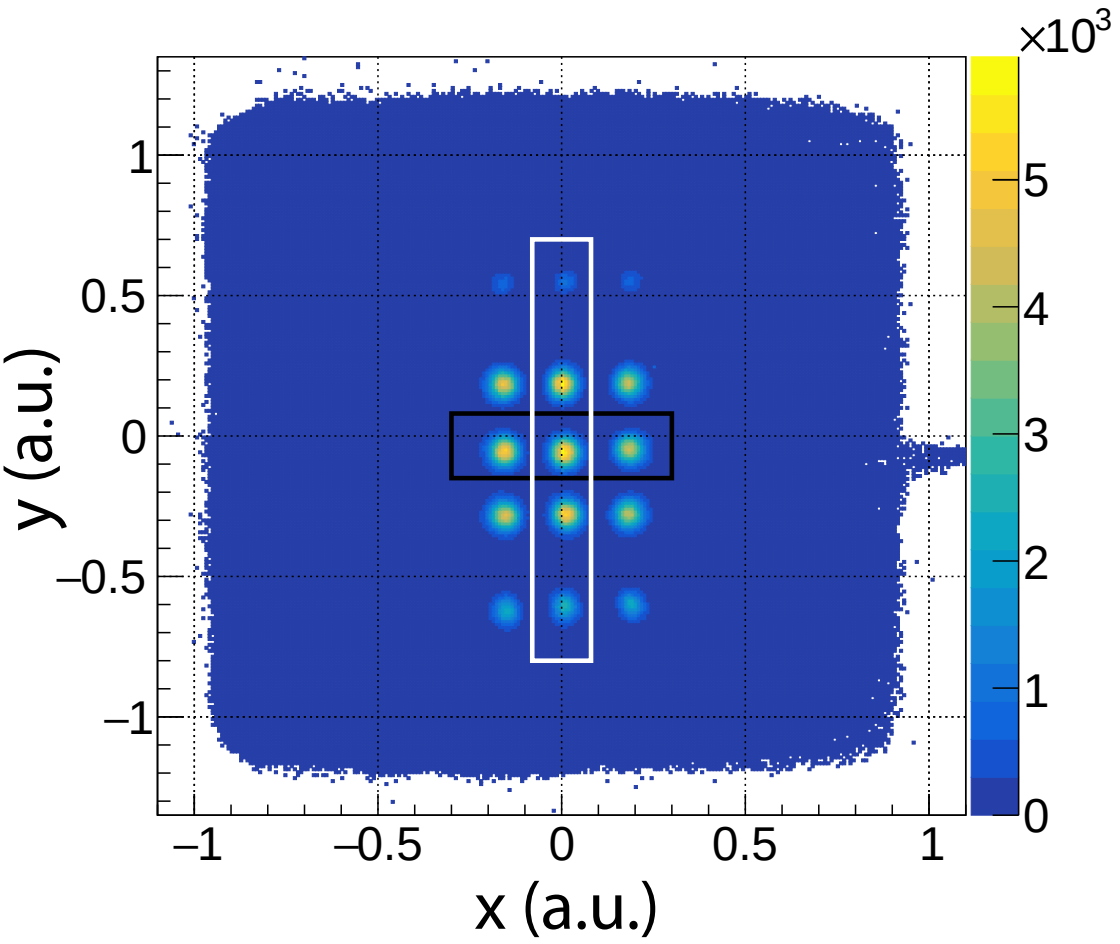

Figure 4.19: Neutron image produced from mask A, shown in Fig. 4.13, for a 2 h 35 min run. The white and black reagions were selected for the calibration.

To locate the position of the holes, we fit a gaussian curve to its projection, as shown in Figs. 4.20a and 4.20b. The information of the scanned position with the center of each peak enabled us to fit the linear correspondence between them, as we see in Figs. 4.20c and 4.20d.

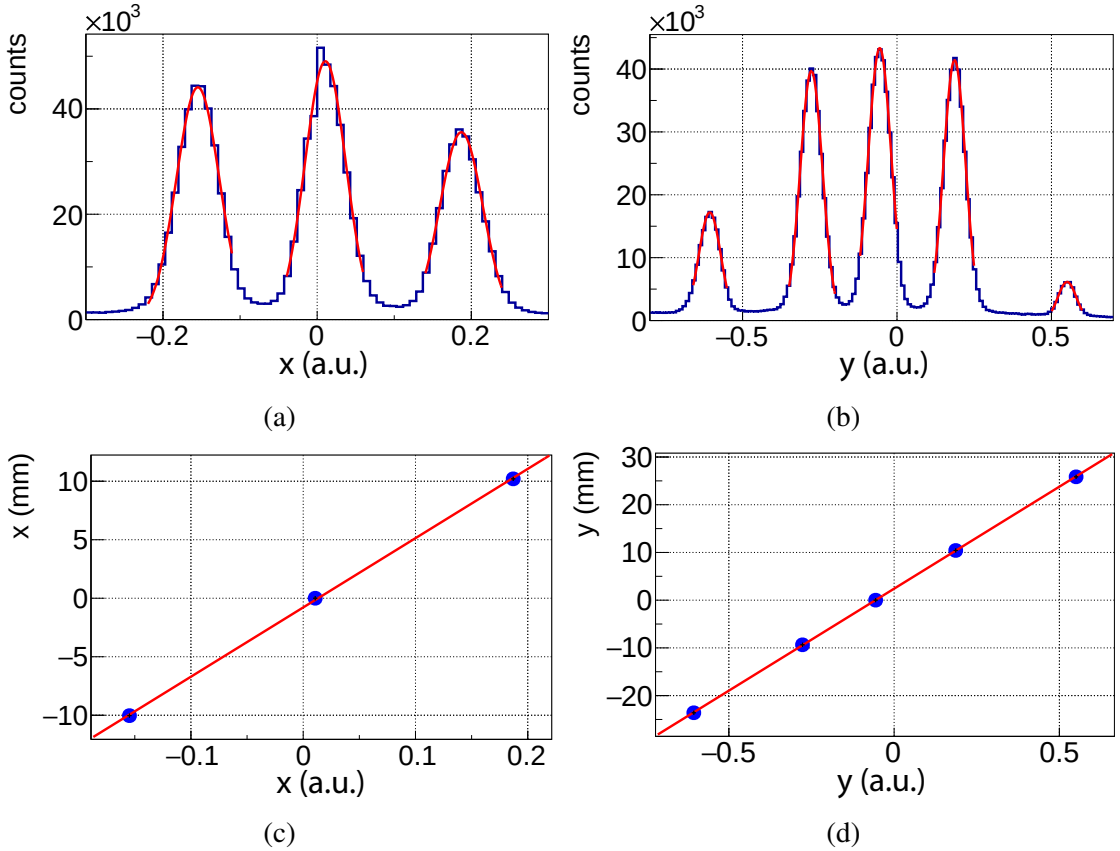

Figure 4.20: Calibration process, with the projection of the three horizontal central holes (a) and the projection of the central vertical holes (b). The calibration consists of the linear dependence that corresponds bins coordinates to mm coordinates for x (c) and y (d) directions.

With the calibration, all the runs measured can be analyzed concerning the dimensions of the detector, allowing us to obtain the position resolution and measure distances of the neutron image. The result of the process shown in Fig. 4.20 is depicted in Fig. 4.21.

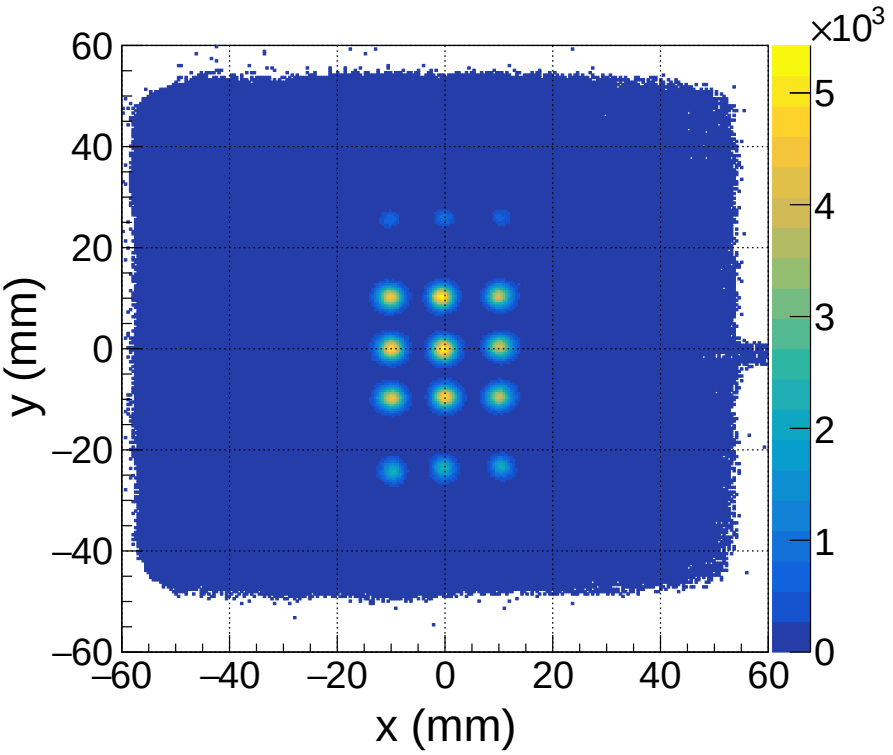

Figure 4.21: Calibrated neutron image resulted from the calibration process shown in Fig. 4.20, using mask A, shown in Fig. 4.13, for a $2\,\mathrm{h}\ 35\,\mathrm{min}$ run.

Patterns distributed along a larger region are better to use in calibrations. Analyzing Fig. 4.21, the borders in Y direction are closer to $\pm 50\,\mathrm{mm}$, matching the sensitive area of the readout. For the X direction, there is a slight difference that should be reduced by using more holes in that direction. However, the shape of the beam limits the area one can illuminate at the same time. Besides, the border regions present some distortion, due boundary conditions posed by the end of the readout strips pattern and a small border effect of the electric fields.

The mask A, shown in Fig. 4.13 is preliminary, and the same process was performed for the mask in Fig. 4.18, which has more precise dimensions. Nonetheless, we recommend that every time one turns the detector on, a five minutes run of the calibration mask must be acquired. This recommendation is because variations in pressure and temperature can change the detector's gain, as discussed in sec. 3.5.3, implying subtle changes in the calibration constants.

4.3.1 Area uncertainty

In this section, we start from some general considerations to verify the effectiveness of our calibrations regarding the obtained uncertainties. To evaluate the uncertainty in the

calibrated area for circular holes, we associate the area with the linear dimension related to the calibration; the diameter, writing

$$A_c = \frac{\pi}{4} d_c^2, \tag{4.9}$$

where d_c is the calibrated diameter. Since the calibration also imposes some error, we also consider that

$$d_c = \frac{d_p}{F_{cal}}, \tag{4.10}$$

where d_p is the diameter in pixels (native unit) and F_{cal} the calibration factor. As mentioned in sec. 4.3, for a $300\,\mathrm{ppi}$ image, we expect to obtain $F_c = 11.811(39)\,\mathrm{px/mm}$. Applying the simple error propagation theory (without considering covariances, since these variables are expected to be independent) to the area of Equation 4.9, we get

$$\sigma_{Ac}^2 = \left(\frac{\pi}{2} d_c \sigma_{dc}\right)^2. \tag{4.11}$$

The same reasoning is used to obtain σ_{dc}, as follows:

$$\sigma_{dc}^2 = \left(\frac{d_p \sigma_F}{F_{cal}^2}\right)^2 + \left(\frac{\sigma_{dp}}{F_{cal}}\right)^2, \tag{4.12}$$

where σ_{dp} is the uncertainty of the diameter in the pixels that can be estimated. For sharp images where it is possible to identify the hole border easily, it can be considered 1 pixel, as in our calibrations. Applying Eq. 4.12 in Eq. 4.11 and expressing d_c as a function of A_c, we get

$$\sigma_{Ac} = \frac{1}{F_{cal}} \sqrt{4A_c^2 \sigma_F^2 + \pi A_c \sigma_{dp}^2} \Rightarrow \frac{\sigma_{Ac}}{A_c} = \frac{1}{F_{cal}} \sqrt{4\sigma_F^2 + \pi \frac{{\sigma_{dp}}^2}{A_c}}, \tag{4.13}$$

shown in Fig. 4.22, where we used the values that we obtained for our experiment: $F_c = 11.811\,\mathrm{px/mm}$, $\sigma_F = 0.039\,\mathrm{px/mm}$, and $\sigma_{dp} = 1\,\mathrm{px}$.

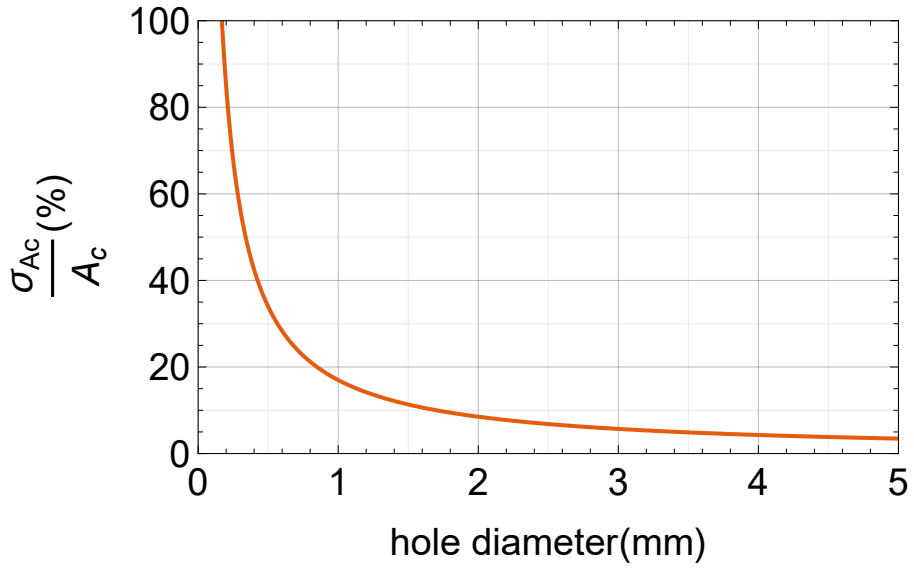

Figure 4.22: Relative uncertainty in the area of the hole as a function of the diameter for the parameters we obtained experimentally.

As shown in Fig. 4.22, above $1.5\,\mathrm{mm}$, the uncertainty in the area of the hole is below $20\,\%$, which justifies using $300\,\mathrm{ppi}$ as digitalization resolution.

The areas of the holes obtained for the scanned handmade masks are compatible ($\max(Z_{fac})= 1.8$) with the expected, which is the nominal area given by Eq. 4.9, considering uncertainty zero for simplicity. It is possible to see this agreement by plotting the experimental values we obtained with the nominal area, shown in Fig. 4.23.

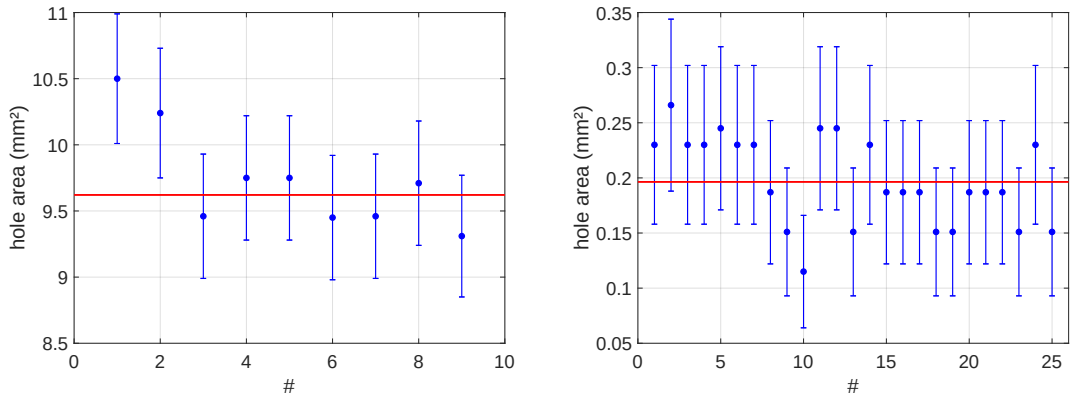

(a) (b)

Figure 4.23: Obtained areas for the $3.5\,\mathrm{mm}$ diameter holes from the mask A, presented in the Fig. 4.13 (a) and for the $0.5\,\mathrm{mm}$ from the mask B, presented in the Fig. 4.14 (b). The red line on both plots represent the nominal area, computed with Eq. 4.9.

The dispersion of the points for the $0.5\,\mathrm{mm}$ diameter holes (Fig. 4.23b) suggests that the uncertainties considered using this method are slightly overestimated, while reason-

able for $3.5\,\mathrm{mm}$ diameter holes (Fig. 4.23a). Considering this case, the average uncertainty evaluated using Eq. 4.13 is about $64\,\%$ bigger than the standard deviation, which also points a small overestimation. It happens because the obtained area for small holes is generally bigger than expected (which is the drill diameter) due to the cadmium malleability. A smaller transversal area of the $0.5\,\mathrm{mm}$ thick drill imply a bigger pressure transfered to the material, which suffers some deformation during the drill. The resultant holes ends up slightly larger than the drill and with some burr, which are removed later. As bigger area A_c, bigger σ_{A_c} (see Eq. 4.13). Nevertheless, it does not pose a problem since the distribution of areas remains near the expected value, making it still reasonable to consider these holes as $0.5\,\mathrm{mm}$ diameter holes and also use $300\,\mathrm{ppi}$ digitalization. Despite seeming trivial, this is an important consistency check, since cadmium is extremely malleable, liable of suffering important distortions when drilled without precision machines and proper drilling masks.

A similar analysis is used for rectangular holes, where the difference lies only in the expression for the area (Equation 4.9), which results in

$$\frac{\sigma_A}{A} = \frac{2}{F_{cal}}\sqrt{\sigma_F^2 + \frac{{\sigma_{dp}}^2}{A}}, \tag{4.14}$$

very similar to the dependance found in Eq. 4.13. This analysis was critical on the detection efficiency evaluation, that will discuss in next sections.

Chapter 5

Experimental Setup

5.1 Detector setup

This prototype was expected to detect only thermal neutrons with fair efficiency in a high background gamma environment, using just one converter layer. We also expected to produce a position-sensitive prototype that could be easily assembled and operated. It should also be easily transported and fixed if any problem happens and should work for at least some hours in a steady regime. The main geometrical aspects of the detector are shown in Fig. 5.1.

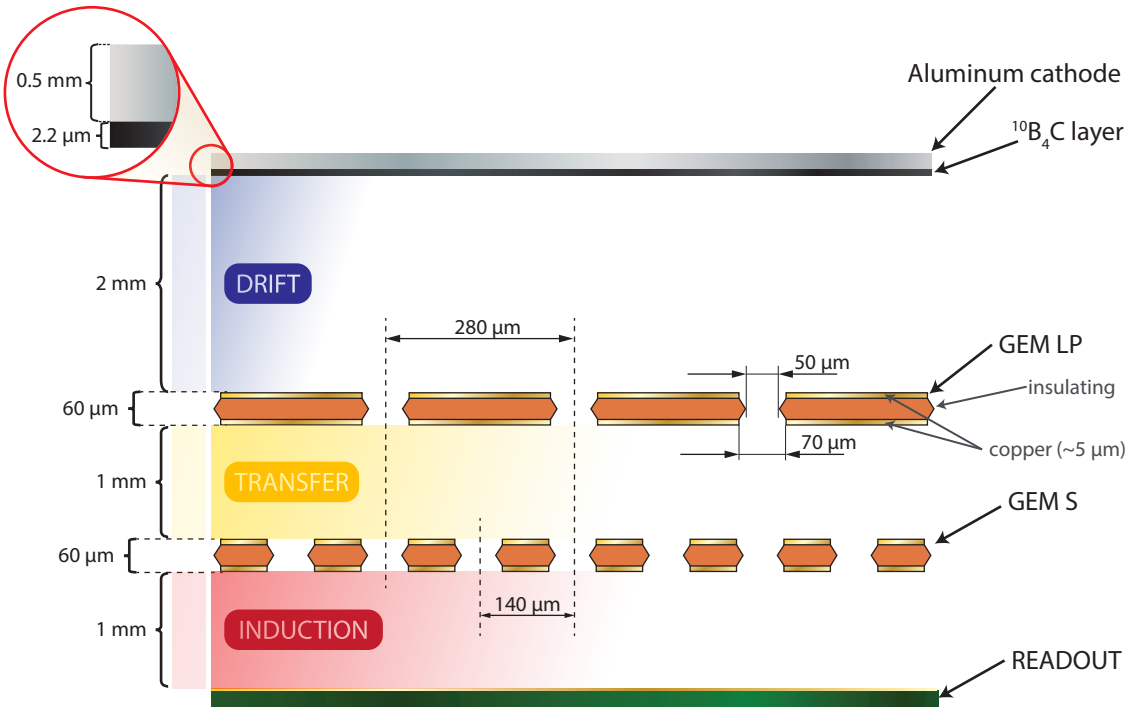

Figure 5.1: Scheme showing the detector setup (out of scale).

Given its versatility, a $0.5\,\mathrm{mm}$ thick aluminum cathode was decided as a suitable sub-

strate for the deposition. The ESS has the know-how to perform this kind of deposition, that was done by direct-current magnetrom sputtering in the ESS Detector Coating Workshop, at Linköping, Sweden. Details about the processes and characterization of the depositons are available in other works they published [74–76].

As kindly informed by Chung-Chuan Lai, the coating process is done installing two $^{10}B_4C$, more than $95\,\mathrm{wt.\%}$ of ^{10}B enriched, on the sputtering cathodes of a CemeCon AG CC800/9 deposition unit and attaching an Al plate to an Al backing plate, mounting the whole assembly to an electrically grounded sample table. The system is first pumped down to $1.5 \times 10^{-4}\,\mathrm{Pa}$ while the deposition plate is heated up to $\sim 280\,^{\circ}\mathrm{C}$ for $3\,\mathrm{h}$, to remove water residues from the surface, before cooling down for additional $2\,\mathrm{h}$. The substract is then treated with radio frequency plasma etching (at $0.35\,\mathrm{Pa}$ pure Ar) to improve the coating's adhesion and increase surface roughness. The system is then filled with Ar up to $0.8\,\mathrm{Pa}$ to begin the deposition process. A polished Si reference plate is monted at an equivalent position of the Al deposition plate in the same run for the thickness measurement, which resulted to be $\sim 2.2\,\mu\mathrm{m}$ using a Bruker DektakXT profilometer. The thickness was decided to enhance the neutron detection, considering that thicker depositions will absorb more neutrons (not necessarily detected), and thinner ones will allow more capture reaction products to escape.

The drift zone is a vital component of the detector since it has to provide room enough for the products of the neutron capture reaction to create as much as possible ionization but be sufficiently thin to present low sensitivity, i.e., low efficiency, for gamma-rays. Attention should be paid since, by making drift zone too thin, the energy that can deposit decreases since almost all the particles quickly encounter the top GEM (see sec. 3.5.3), even inducing sparks if many encounters happen too near the holes at close times. Therefore, the detector is pretty sensitive to the depth of the drift zone. The solution for this problem was based in the knowlege of the neutron capture products (see Eq. 2.12) and preliminary SRIM[35] simulations, shown in Fig 5.2.

As we can see in 5.2, the most energetic α needs around $10\,\mathrm{mm}$ to deposit all its energy, which is unpractical given that the detector has to be not sensible to gamma-rays. Considering the density of the $ArCO_2$ gaseous mixture ($\rho \approx 1.6 \times 10^{-3}\,\mathrm{g\,cm^{-3}}$) and the maximum mass atenuation coefficient for the gas ($\mu/\rho \sim 1 \times 10^{4}\,\mathrm{cm\,g^{-2}}$ [77]), the probability of gamma-rays absorption is negligible to a $2\,\mathrm{mm}$ layer of gas. The experimental tests with several minutes runs did not obtain a single gamma count with the neutron beam off.

Integrating the energy loss curves makes it possible to obtain the energy deposition curve, shown in Fig. 5.3. Considering the worst-case scenario, where the most energetic alpha crosses the $2\,\mathrm{mm}$ thick layer of gas hitting the GEM, it would deposit around

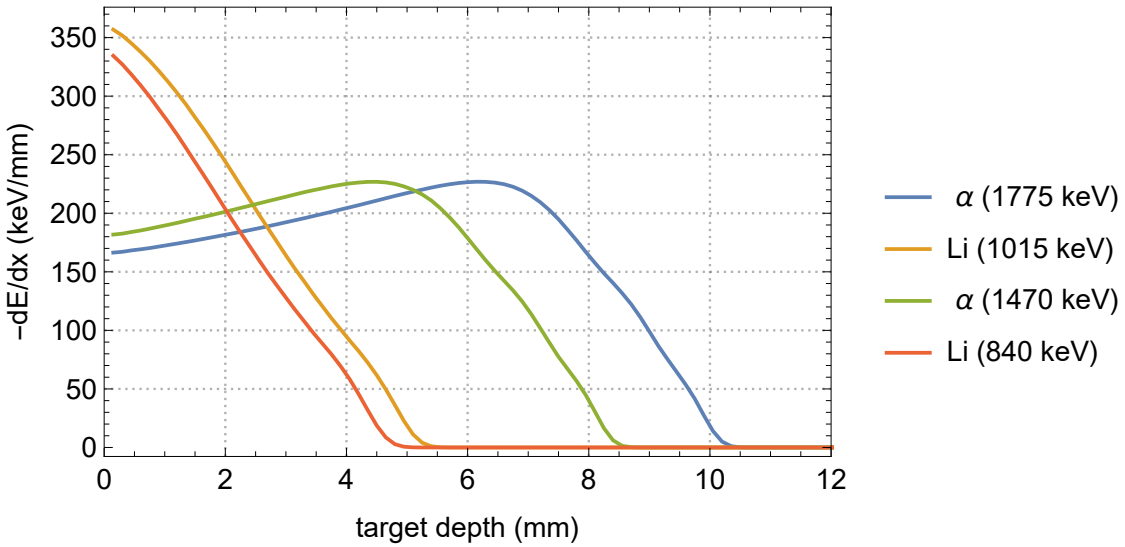

Figure 5.2: Average energy loss for α and ^{7}Li for both decays, in $ArCO_2$ (90/30) as a function of the distance travelled, SRIM simulation using 50000 ions for each curve.

$400\,\mathrm{keV}$ that is detectable considering our electronic threshold (about $100\,\mathrm{keV}$). Moreover, just a few particles will escape almost perpendicularly to the deposition since the decay is isotropic.

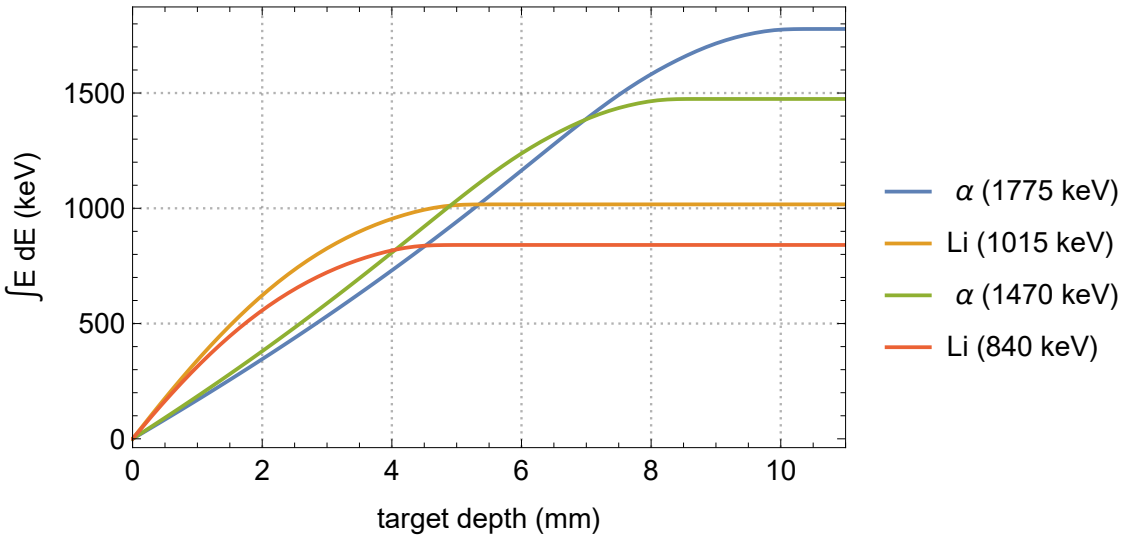

Figure 5.3: Deposited energy in the gas by the products of the neutron capture. SRIM simulation using 50000 ions for each curve.

Using two GEMs was another choice, considering the stability of the detector. The probability of discharge depends on the distance to the radiation source (in our case, the deposition itself, since we are measuring the products of the neutron capture reaction) and the gain of the GEM [78]. For this reason, we also choose the large pitch (LP) GEM as the top one since it presents a much lower holes density. With this consideration, positioning

a GEM closer to the deposition, still guaranteeing stable and safe (no discharges) working conditions, requires operating it at slightly low voltage. To maintain a suitable gain by lowering the voltage, we needed to add a second GEM. The choice of transfer and induction region as $1\,\mathrm{mm}$ thick was considered to reduce the gamma interaction probability and the gaseous volume of the detector.

The electric fields used were $0.5\,\mathrm{kV\,cm^{-1}}$, $3.0\,\mathrm{kV\,cm^{-1}}$, and $4.0\,\mathrm{kV\,cm^{-1}}$ for the drift, transfer and induction zones, respectively, and the voltage biases in both GEMs were $300\,\mathrm{V}$. The detector never suffered any discharges, even operating continuously for hours, which means the discharge probability is negligible at this voltages regime. It is worth noting that the voltages applied are all negative so that we can collect the electrons at the readout. These values were chosen started from simulations made by Geovane Grossi, a fellow of our research group, in his work [79]. However, preliminary tests with the detector were essential to fine-tune the configurations (also considering that Geovane's simulations treated very different energies). With some knowledge about the working of these detectors gained in previous work, it was possible to converge to these values.

5.2 Resistive charge division

The charges produced at the drift zone and multiplied by the GEM cascade are collected in the readout plane. The readout plane is made of a printed circuit board (PCB) coupled with the reading layer responsible for its sensitive zone. This layer consists of two sets with 256 copper strips each, stacked so that the direction of the strips of each group is perpendicular to the direction of the other. For obvious reasons, these strips do not touch each other. Their manufacturing process is very similar to the manufacturing of GEMS: the strips pattern is drawn, using standard PCB techniques, on both sides of a $50\,\mu\mathrm{m}$ thick polyimide foil that is afterward fixed on a support. Eventually, the polymer between the strips of the exposed side is corroded with solvent [80]. The strips cover a square area of $10\,\mathrm{cm}$ side, with a pitch of $400\,\mu\mathrm{m}$ and has $80\,\mu\mathrm{m}$ thick and $340\,\mu\mathrm{m}$ thick, respectivelly, as shown in Fig. 5.4. The width difference of the strips is to assure an equal share of charge since they are not in the same plane.

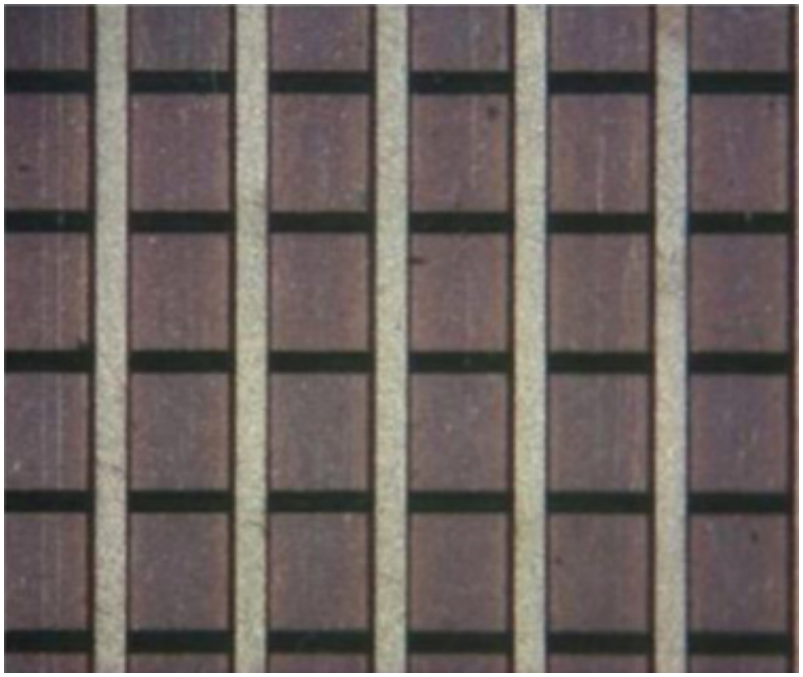

Figure 5.4: Readout close up. The X-Y strips are patterned over a thin polyimide foil that is etched to remove the material between the top strips. The top strips have a width of $80\,\mu\mathrm{m}$ and the bottom ones $340\,\mu\mathrm{m}$ to assure equal charge distribution between the top and bottom stripes. Figure from [81].

The negative charges generated by the incoming radiation and multiplied by the GEMs stack are collected in the strips, which are kept at ground potential. The signal is read using resistive chains that provide four electronic channels, two channels for each direction (X and Y), as shown in Fig. 5.5. For each direction, the resistive chain connects the strips with resistors responsible for attenuating the collected signal.

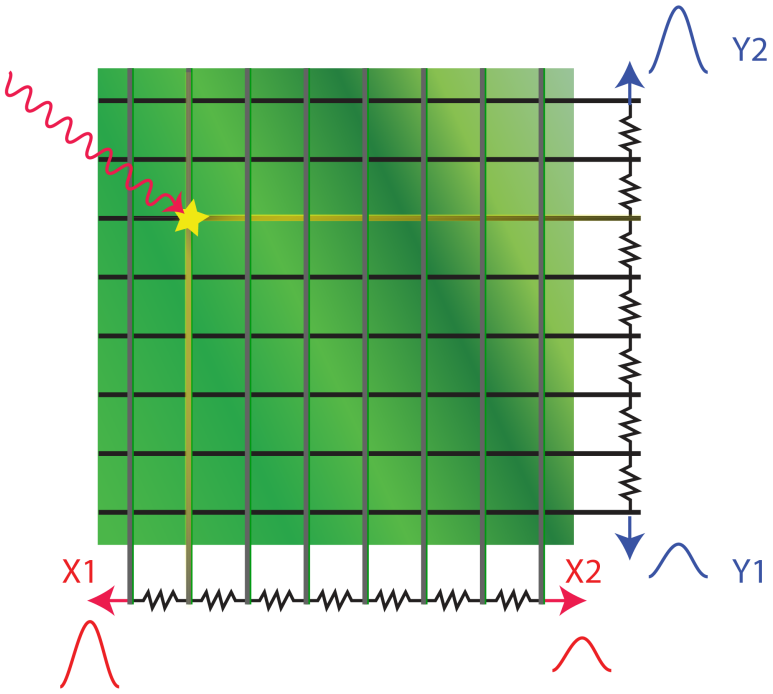

Figure 5.5: Simplified scheme of the readout charge collection process showing a point charge collection and the signal shape at each end of the resistive chain.

The mentioned attenuation is related to the distance the charge has to travel to be collected. When it reaches the resistive chain, it is divided in inverse proportion of the resistance between its strip and the pre-amplifier input. In other words, this idea is pictured in Fig. 5.5, where there is a difference in the signal received for each corner X1, X2, Y1, Y2, of the system. To reconstruct the original position where the charge reaches the readout, it is possible to use a center of gravity (COG) type algorithm:

$$x = A\frac{Q_{X2} - Q_{X1}}{Q_{X2} + Q_{X1}}, \qquad y = B\frac{Q_{Y2} - Q_{Y1}}{Q_{Y2} + Q_{Y1}} \tag{5.1}$$

where Q_{X1}, Q_{X2}, Q_{Y1}, Q_{Y2} are the collected charges at each end of the resistive chains, and A and B constants that adjust the length of the image (they have length dimension). Nevertheless, this algorithm leads to pin cushion distortion due to the interdependency between the directions (we have few pF capacitance between each strip and the other coordinate's plane) as well as charge losses in the borders. The details of this problem will be not addressed in this work since its well-known solution consists of reconstructing the image by using the total charge of the event as the denominator to compute the event coordinates [82–84]:

$$x = C\frac{Q_{X2} - Q_{X1}}{Q_T}, \qquad y = D\frac{Q_{Y2} - Q_{Y1}}{Q_T}. \tag{5.2}$$

where Q_T is the total charge of the event, and C and D are constants. The charge information of the event, Q_T, is collected at the bottom of the lower GEM and will be discussed further. The Fig. 5.6 shown the reconstruction using the algorithms of Eq. 5.1 and 5.2. As expected, the distortion is stronger in the borders for the first case (Fig. 5.6a).

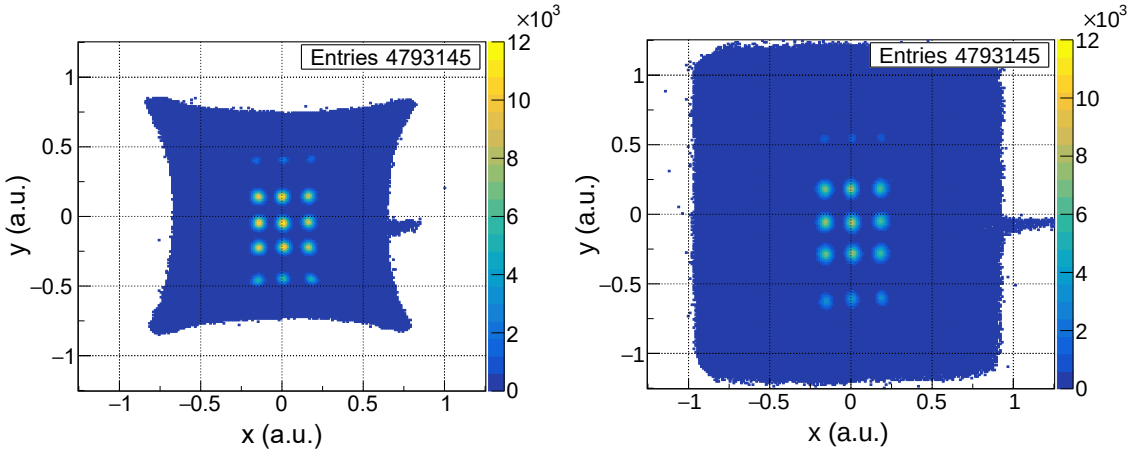

(a) (b)

Figure 5.6: Image reconstruction of mask A, shown in Fig. 4.13, using the partial charge given by Eq. 5.1 (a) and the total charge, given by Eq. 5.2 (b). Constants A, B, C, and D were considered equals to one. The run presented in the reconstruction has a $2\,\mathrm{h}\ 35\,\mathrm{min}$ acquisition time.

The resistive chains were projected specifically to fit this sort of readout in a previous work [85]. Each one has 128 SMD resistors of $60.00(6)\ \Omega$. Its dimensions (about $43\,\mathrm{mm}$ x $79\,\mathrm{mm}$) were designed so they can be series connected next to the other (at the connectors soldered in the readout plane), forming the 256 resistors chain for each direction. The boards, shown in Figure 5.7, were produced and assembled by local industry and it showed to be an accessible process regarding the time of production and cost. A Panasonic®130-pin connector (nowadays discontinued) was used to match the readout plane provided by CERN.

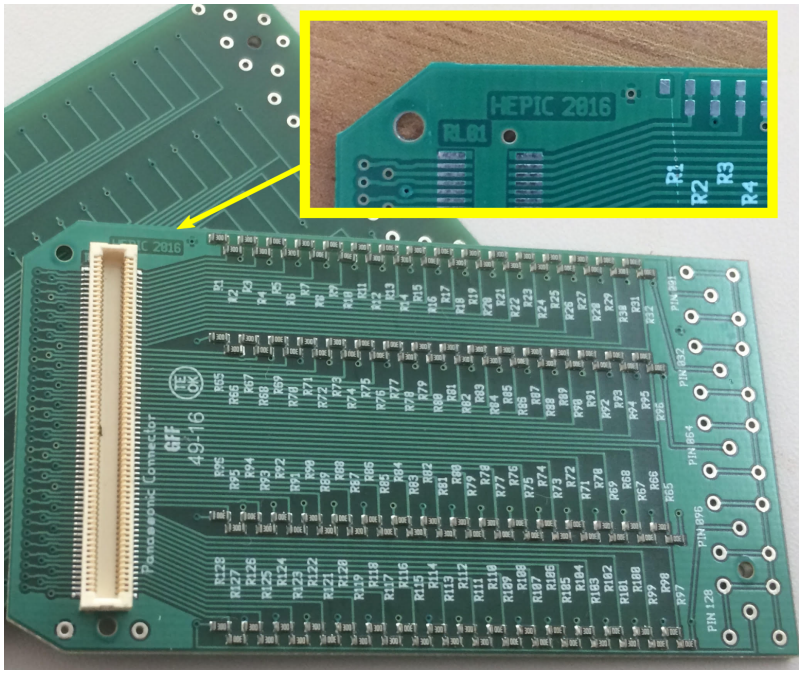

Figure 5.7: 128 channels resistive chains produced by our group. Figure from [79].

5.3 Acquisition setup

The acquisition configurations foresaw a total of 5 channels, 4 used for the position information and the last for energy information. The energy information is given by a percentage of electrons that are captured on the bottom of the lower GEM, this represents typically $64\,\%$ of the electrons generated at the multiplication [79]. On the other hand, the position information is provided by the different fractions of the charge that arrive at each end of the resistive chains. The total charge carried to the readout plane is equally divided between X and Y directions, except when very close to the borders, where this division is not equal.

All the electric charges of the 5 channels are collected by non-commercial preamplifiers made at Michigan State University. The pre-amplifiers integrate the charge signal, generating a voltage pulse with its height proportional to the integrated charge as shown in Fig 5.8.

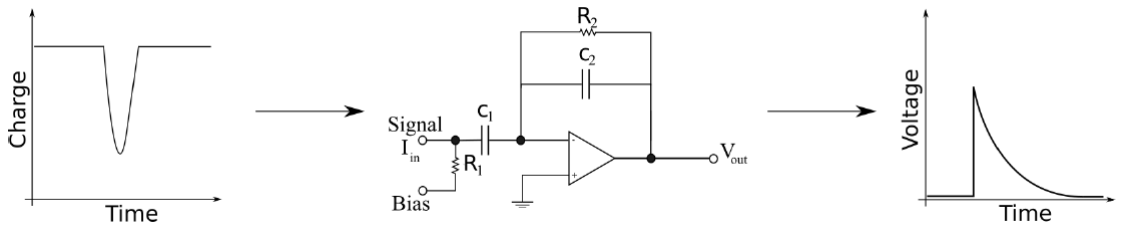

Figure 5.8: Preamplifiers working principle. Figure from [79].

An important characteristic of the preamplifier is the decay time constant $\tau_p = R_2C_2$ which sets the time interval needed so the pulse height decays $1/e$ of the original height. This value has to be chosen so the signal decays fast enough to avoid pile-up, which can interfere in the signal acquisition.

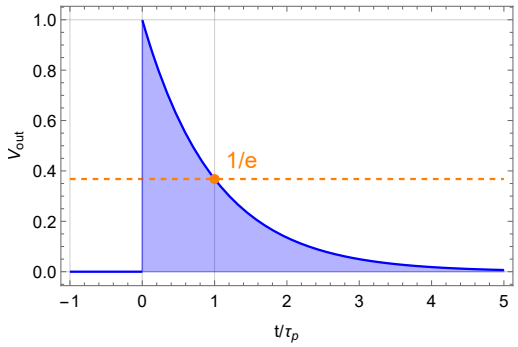

(a) Preamp response to a charge pulse. The peak voltage was set to 1V for easier visualization.

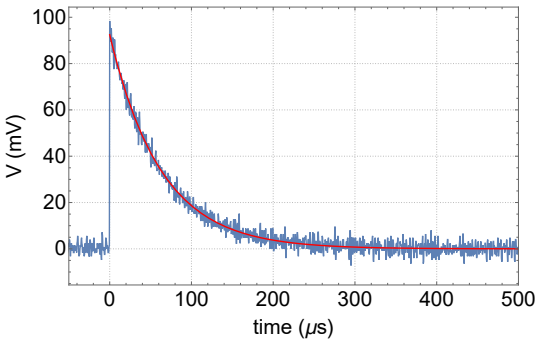

(b) Real preamp response fit, with the obtained $\tau_p = 62.41(38)$ µs time constant.

Figure 5.9: Theoretical preamp output (a) and the output of one of the preamps used in this experiment (b).

The next step of the processing chain, for all channels, is executed with NIM (Nuclear Instrumentation Modules) modules. The voltage pulses produced by the preamplifiers are carried to NIM shaper-amplifiers also produced by Michigan State University. These amplifiers differentiate and integrate the voltage pulse 3 times, in an alternate way, and also offer the possibility to collect the signal after just one differentiation and one integration, using the "fast" output. This output is particularly useful for the trigger signal which needs to be faster than the other 4 acquired ones. The differentiation constant τ_d and the integration constant τ_i can be set using switches inside the module, as pictured in Figure 5.10.

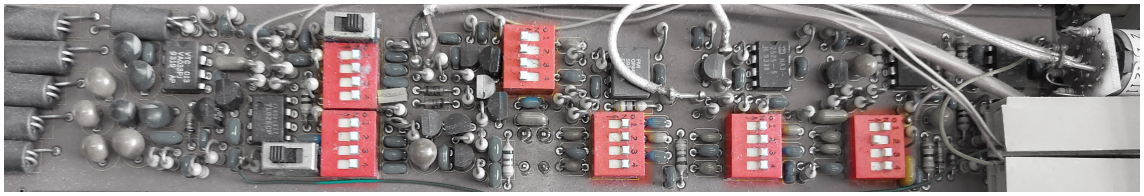

Figure 5.10: Shaper-amplifier NIM module differentiation and integration constants selectors (colored). For the first stage, the available constants are 30 ns for the differentiation and 10 ns for the integration, where each of them that can be multiplied by 1, 3, 10 or 30 using the selectors. For the another three slow stages, the constants are 1 µs with possibility to add 2 µs and 4 µs separately ou simultaneously.

The purpose of shaping the signal is to assure a correct signal reading; since the pulse height is proportional to the charge collected, it has to be properly measured. The sharp peak of the preamp output is not easy to be read and is also high-frequency noise sensitive [33]. The shaping process provides proper rise and fall times and is usually done utilizing differentiator and integrator circuits. The most common kind of these circuits is the CR filter, also known as the highpass filter, for the differentiation and the RC filter, or lowpass filter, as the integrator circuit. Together they act as a bandpass filter, as shown in Figure 5.11.

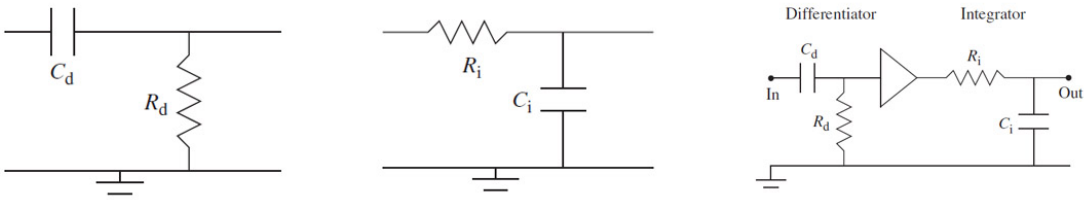

Figure 5.11: CR differentiator circuit (left), RC integrator circuit (center) and combined CR-RC shaper circuit. Note that there is an Voltage amplifier between the CR and RC parts of the shaper circuit.

It is interesting to consider the response of these circuits for a step input signal, depicted in Figure 5.12. For a sufficiently high value of the time constant τ_p of the preamplifier, we can consider its output approximately as a step signal. For the real case, there is a small undershoot in the final output, which is often corrected using the pole-zero cancelation, by adding a variable resistor in parallel to the differentiator capacitor.

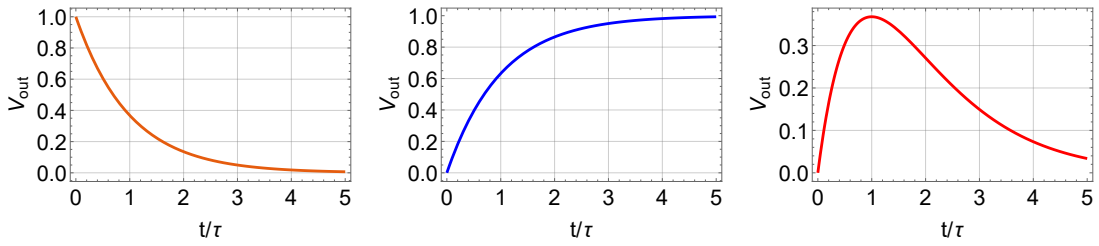

Figure 5.12: Signal responses for the CR circuit (left), RC circuit (center) and combined CR-RC circuit for a step input signal. Here we supposed that $\tau_i = \tau_d = \tau$.

As shown in Fig. 5.12, the shaping process is a very versatile way to control the input signal to be read since one can fine-control the rise and fall times, preserving linearity between the maximum voltage and the initial quantity of charge that generated the signal. The CR-RC shaper shown in Fig. 5.11 commonly uses variable components to simplify changes in the time constants. As shown in Fig. 5.10, it is possible to combine shaper circuits to obtain an even precise control, as in the case of the modules we use.

After passing the shaper-amplifiers, the four position signals are ready to be read. The trigger signal, meanwhile, travels through a different chain: it is collected at the fast output of the shaper amplifier and goes to the discriminator module (ORTEC CF8000) where we set a voltage threshold to avoid noises triggering the signal digitalization. When the discriminator module receives a signal above the threshold, it triggers the gate generator module (ORTEC GG8010) by sending a logic signal to it.

The gate module is responsible for determining the time window in which the peak-ADC will work. The gate signal's width and delay are adjustable by changing the square signal this module sends to the CAMAC peak-ADC module (PHILLIPS 7164), where the maximum height of each of the five signals is digitized. As the analogical signals coming from the amplifiers have the same time constant, we expect these signals to arrive near each other, so this fine adjusts of width and delay take this into account. This processing chain is pictured in Figure 5.13.

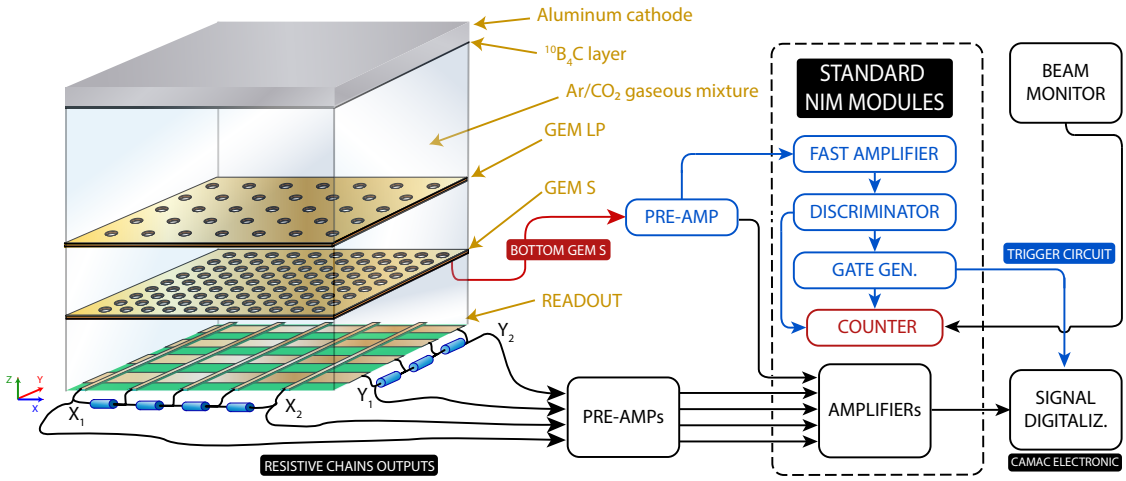

Figure 5.13: Scheme showing the detector and acquisition setup (out of scale). Figure from [86].

A multichannel counter module (CAEN N1145) is used to register the counts of a neutron beam monitor (LND3053), positioned at the outlet of the neutron beam. It is also used to simultaneously check the discriminator and gate generator, making it easier to identify eventual electronic flaws that could happen in any of these two modules.

5.3.1 Electronic limitations

A CAMAC serial module connected with the PC via an ISA board established the connection between the CAMAC ADC module and the computer. The acquisition computer uses ROOT-based software developed by a fellow of our research group. However, given unknown software or hardware limitations, some events are lost.

We carried out some tests to find out the problem's nature. There was the supposition the system behaved following the know *paralyzable* or *non-paralyzable* models for the dead time [34]. The difference between them regards the variation of the dead time: in the non-paralyzable one, the dead time is fixed, whereas, in the other model, it can grow depending on the events rate injected into the system. Confronting the number of events from the saved run files with the annotated events from the counter (see Fig. 5.13), we can check the behavior of the registered rate as a function of the approximated real rate, as shown in the plot of Fig. 5.14. This last assumption is valid since the counter's specifications and the characteristic time of the NIM analogic electronic modules works correctly with rates of at least several kHz.

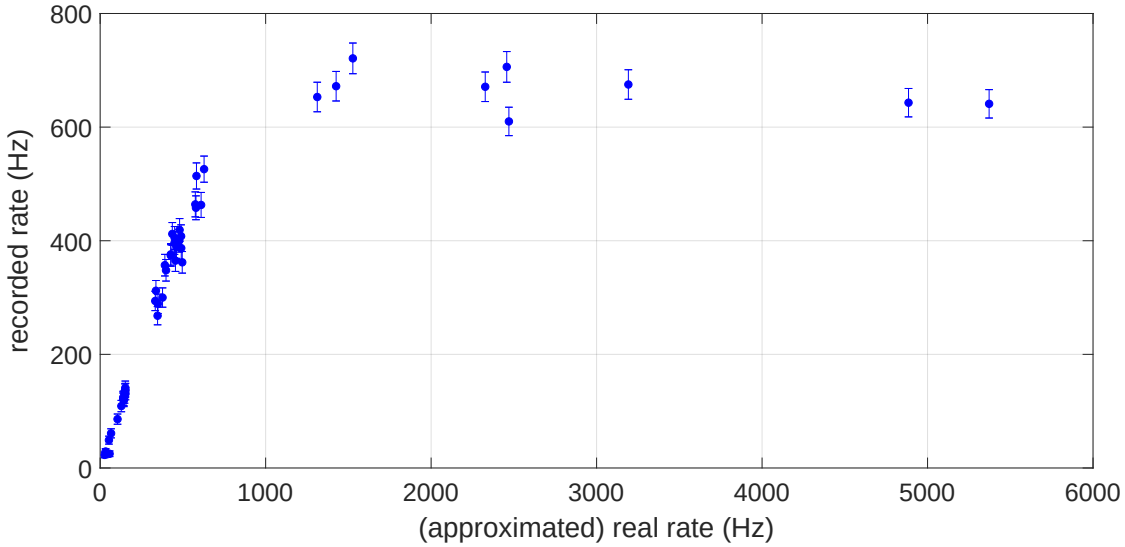

Figure 5.14: Recorded rate (Hz) as a function of the approximated real rate (Hz) for 49 runs. The uncertainties are given by $\sqrt{N}$.

The dependency between the recorded and the actual rates seems to behave linearly until around 700 Hz, where the recorded rate reaches its possible constant maximum. The behavior of the system points towards the existence of a buffer that limits the acquisition. We fit the linear dependency and the continuous value to search for second-order structures, as presented in Fig. 5.15. No second-order structures were found, which means it is safe to consider the system to behave following a linear dependency until about 700 Hz and at a constant recording rate for higher rates.

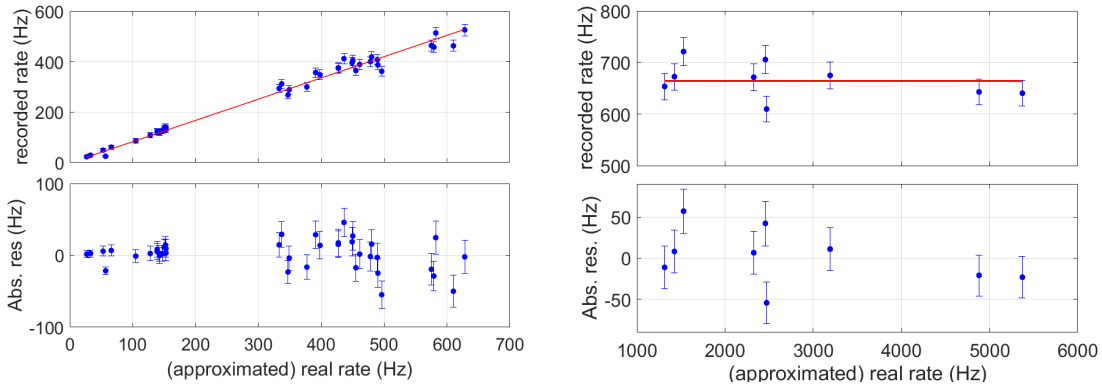

(a) (b)

Figure 5.15: Linear fit ($mx + n$) for real rates up to 700 Hz, resulting m = $0.843(11)$ and n = $-1.5(25)$ Hz (a). Constant fit for real rates higer than 1000 Hz resulting $664.1(86)$ Hz (b). The uncertainties are given by $\sqrt{N}$.

Based on the results presented in Fig 5.15, we must operate the detector at rates lower

than $600\,\mathrm{Hz}$ to get the minimum loss of data, around $15\,\%$. Nevertheless, it is still interesting to perform another test with well-defined frequencies by injecting the proper signal in the test input of the pre-amplifier used as trigger (that also provides the charge signal) to map the recorded rates. Through a capacitor, the test input transforms a voltage step signal (easily produced with a wave generator) into a charge signal injecting it in the preamplifier's standard input. It is important to note that this behavior does not happen in reality since the neutron beam is not pulsed, but it is still helpful to check the CAEN counter and verify if the system has any easiness with constant rate events. The result is shown in Fig. 5.16.

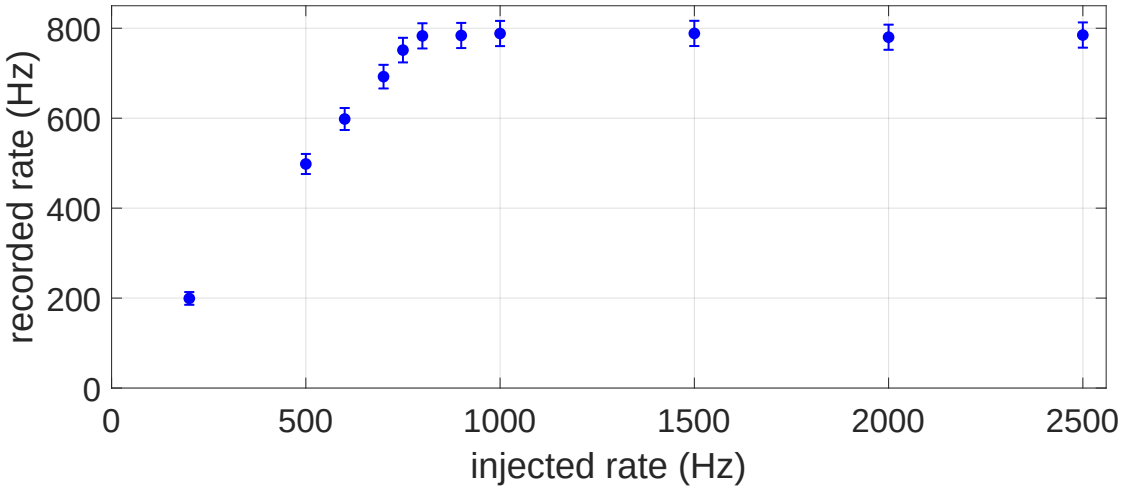

Figure 5.16: Recorded rate (Hz) as a function of the injected rate (Hz). The uncertainties are given by $\sqrt{N}$. The system registered all the events injected for rates below than about $780\,\mathrm{Hz}$. For higher rates, it recorded a constant rate of $784.8(32)\,\mathrm{Hz}$.

The test presented in Fig. 5.16 indicates that the system can deal with higher rates with well-determined frequencies. The CAEN counter behaved as expected[1], offering the maximum error equals $0.004\,\%$ for these rates. However, it is interesting to compute the expected event loss rate for a real source, assuming the dead time of the system equals the period of the saturation rate $(784.8\,\mathrm{Hz})$.

The arrival probability of a neutron in the detector at a given time is constant, which means this is a Poisson random process [34]. Therefore, the probability density function of the intervals between events is provided by,

$$dpf(t) = re^{-rt}, \tag{5.3}$$

plotted in Fig. 5.17, below, for a $784.8\,\mathrm{Hz}$ rate.

[1] this module handles dozens of MHz, making it reasonable to consider its uncertainty virtually zero at our operation rates.

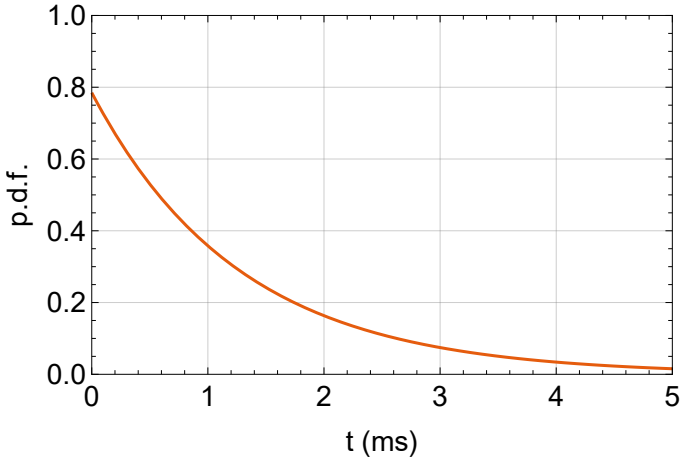

Figure 5.17: Probability density function for the time interval between two consecutive events with same probability to happen, considering the rate r =784.8 Hz, as function of the time interval.

Considering our detector with dead-time $\tau = 1.27\,\mathrm{ms}$, which is the period, τ, for the saturation rate (784.8 Hz), it is helpful to evaluate the event loss rate from the p.d.f. shown in Fig. 5.17. Events separated by a time interval larger than the dead time will be detected, which means that the event loss rate (r_L) can be computed as the fraction of consecutive events in which the time difference is smaller than τ:

$$r_L(r) = \int_0^{\tau} re^{-rt}\,dt = 1 - e^{-r\tau}. \tag{5.4}$$

Naturally, the event loss rate is dependent on the real rate. The dependence obtained in Eq. 5.4 is plotted in Fig. 5.18.

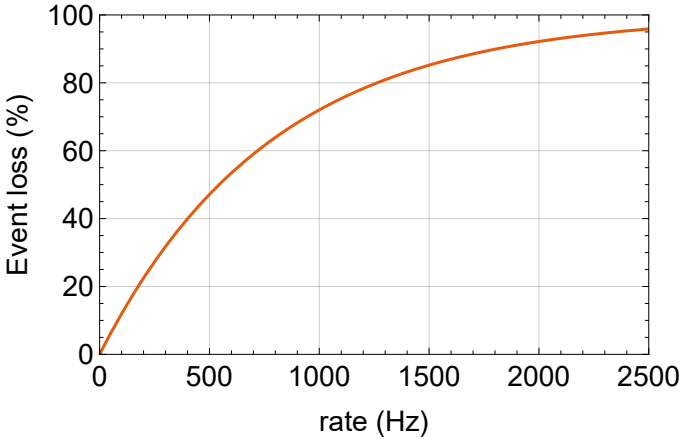

Figure 5.18: Event loss rate as a function the the real rate that enters the acquisition system.

Since our system can be fairly described by the linear dependence fitted in Fig. 5.15a, its loss remains about 16 % for every rate until the saturation rate. This means it be-

haves better than a simple non-paralyzable model but is far from what we expect from a CAMAC system, whose modules are designed to hold at least $140\,\mathrm{MHz}$ [87].

5.4 Measurement setup

The detector was tested with neutrons at the IEA-R1 nuclear research reactor at the Nuclear and Energy Research Institute (IPEN), it is a water-cooled pool-type reactor (see Fig 5.19) that operates at $4.5\,\mathrm{MW}$ [88]. The neutron beam used for this work is the same as AURORA's diffractometer [89] neutron beam.

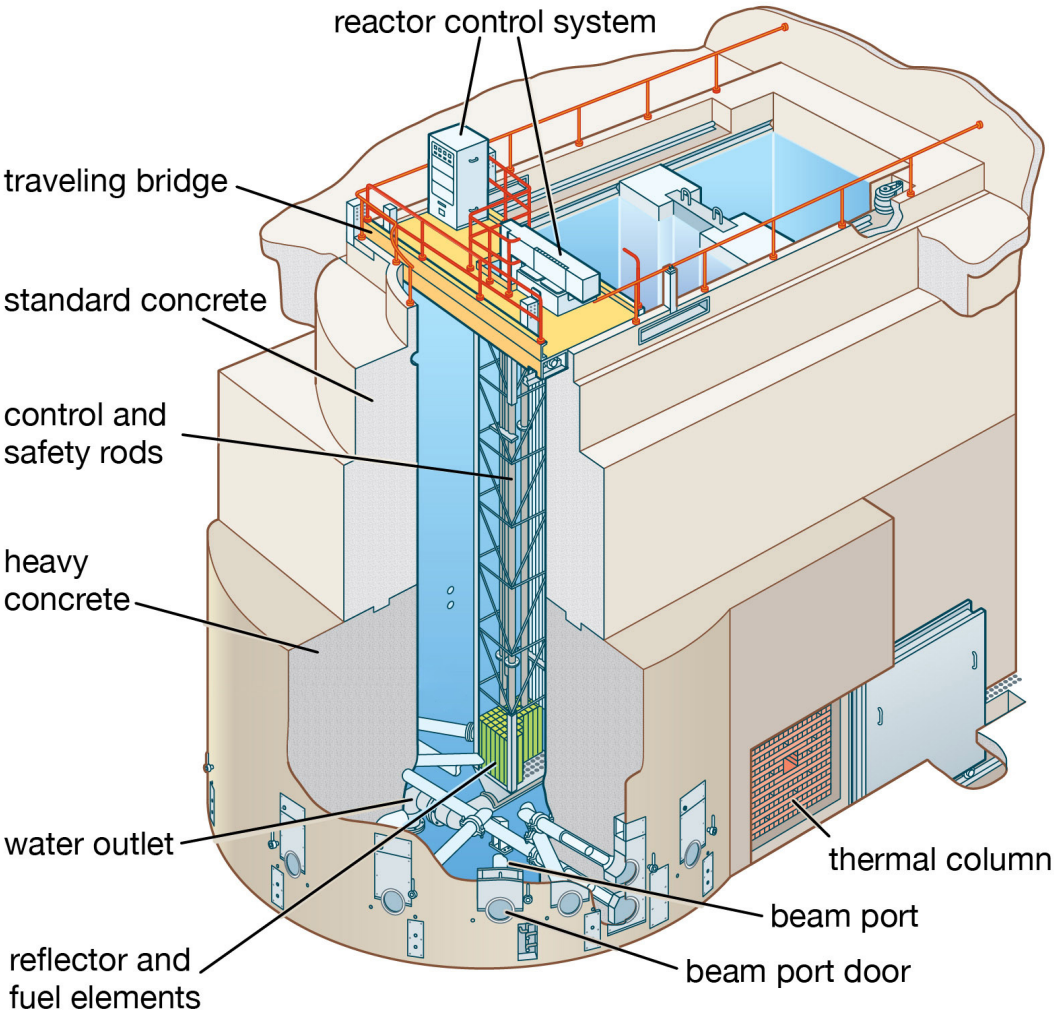

Figure 5.19: Pool type reactor. Adapted from [90].

The detector was positioned using an X-Y-Z table fixed over a regular wooden table. The set was placed in front of the neutron beam, parallel to its outlet, as shown in the Figures 5.20 and 5.21.

Figure 5.20: The blue wall is the reactor pool wall, where it is possible to see two closed beam port doors. The yellow structure encases the AURORA experiment's monochromator and two focusing structures; the set allows the desired neutron energy to be selected. The violet structure contains the position-sensitive detectors of the AURORA experiment [89]. The electronics rack is also visible on the left and the beam stopper (yellow barrel) on the right.

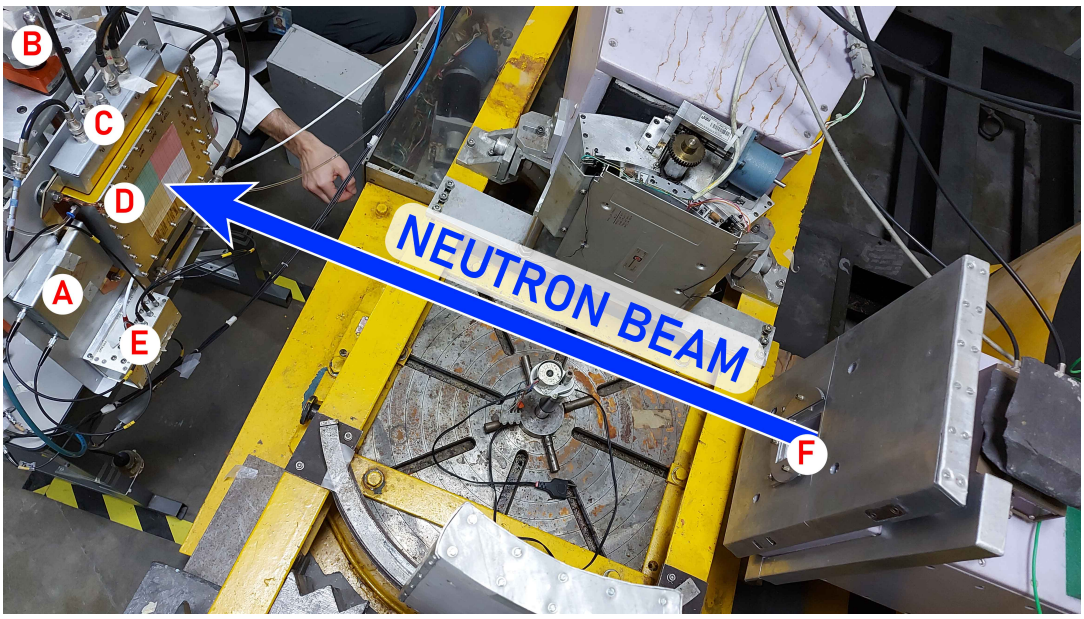

Figure 5.21: Position of the detector relative to the beam showing as well the following elements: shields of the y-direction resistive chains (A), the crank of the precision table for the z-direction (B), High voltage inputs (C), the detector (D), the preamps box (E), and the beam outlet (F).

The neutron beam tube we use (BH-6) is directed towards the reactor core, as pictured

in Fig. 5.22, which means it receives a higher gamma fluency than non-radial tubes. For that reason, proper shielding is necessary to maintain the background radiation at safe levels. Nevertheless, the remaining gamma background is enough to provide a radiation dose of the magnitude of $5\,\mathrm{mSv\,h^{-1}}$ [91].

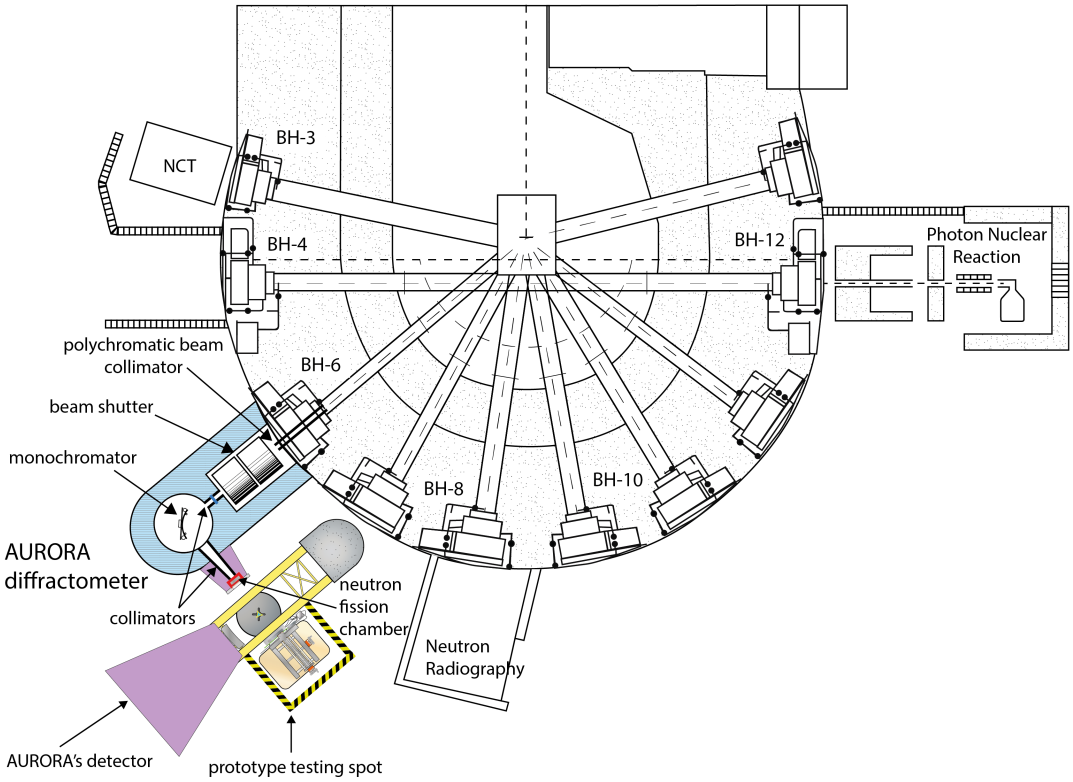

Figure 5.22: IEA-R1 reactor neutron beam lines. Image adpted from [92].

As pictured in Fig. 5.22, the polychromatic neutrons are initially collimated (at the end of the BH-6 beam tube), following towards a beam shutter, another collimator, and finally hitting the monochromator, which will select thermal neutrons from the incident ones through Bragg's diffraction.

The double-focusing silicon monochromator is shown in Fig. 5.23. As reported by [89]: the monochromator is composed of 9 silicon slabs with approximately $5\,\mathrm{mm} \times 14\,\mathrm{mm} \times 190\,\mathrm{mm}$ disposed on a polygonal approximation to a sphere. As also reported in [89], the monochromatic beam exiting the monochromator is collimated by a pyramidal duct that ends in the beam outlet, where a neutron fission chamber used as a neutron monitor is located as also a slit holder (see letter F of Fig. 5.21). This monochromator allows to select 4 different wavelenghts to select. The measurements present in this work were all carried out using $1.399\,\text{Å}$ wavelength ($\approx 41.8\,\mathrm{meV}$) neutrons.

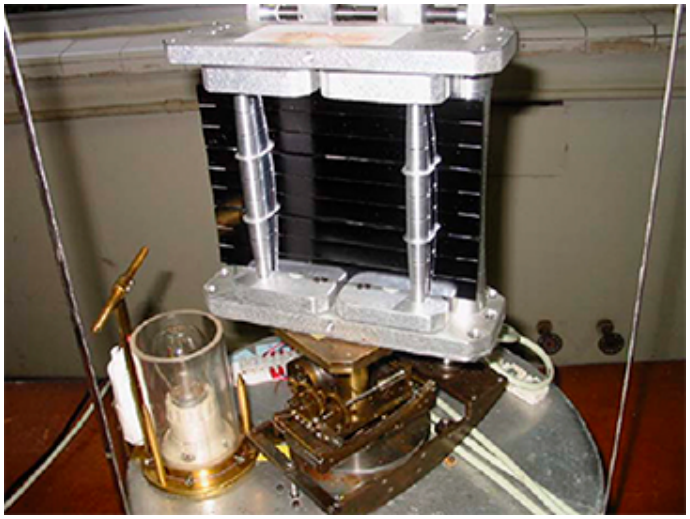

Figure 5.23: AURORA's monochromator. Figure from [89].

The flux of the collimated thermal neutron beam used in the experiment was measured (using an activation reaction, described at sec. 2.3) by the nuclear metrology laboratory at IPEN, with a $12\,\mathrm{mm}$ diameter thin gold foil centered at the beam outlet (letter F of Fig. 5.21). The measurement took almost $8\,\mathrm{h}$ and the obtained flux was $\phi_c = 6.22(19) \times 10^4\,\mathrm{n\,cm^{-2}s^{-1}}$. It was also registered the counts in the neutron monitor[2] fission chamber at the end of the beam collimator (see Fig. 5.22). When collecting data, the fission chamber count is an essential quantity to correct the neutron flux because there is some variation (even if small) in the neutron flux.

It was possible to calibrate the neutron monitor using its count rate, the neutron flux measurement, and the elapsed time, as described. This was an essential procedure to use the fission chamber as a flux meter, estimating the actual flux for different days/runs of the experiment. However, it is crucial to note that the entire beam illuminates the chamber, which means that the calibration only refers to the flux at the central region of the beam, a fact that has to be considered whenever the flux measurement is used.

[2] it is a LND 3053 neutron beam monitor, that uses $130\,\mathrm{mg}$ of ^{235}U enriched more than $93\,\%$ and operates with Ar at $760\,\mathrm{torr}$ pressure.

Chapter 6

Experimental Results

This section presents a brief discussion regarding the neutron beam geometry and some preliminary results from simulations compared with the experiment. Essential characteristics of the detector were also measured and are discussed in detail here, using the concepts previously presented.

6.1 Preliminary measurements

Preliminary measurements were conducted after assembling the detector as testing the acquisition system, NIM modules, and the pre-amplifiers. The detector was positioned in front of the neutron beam outlet and properly centered (see Fig. 5.21).

One of the first images obtained with the system is shown in Fig. 6.1b. It is the neutron image of a plastic and metal power outlet, similar to the one shown in Fig. 6.1a. The relatively high amount of hydrogen in the polymers causes the neutrons to scatter via the $^{1}H(n,n)^{1}H$ elastic scattering, allowing to locate the plastic region due to the difference in the intensity of the image.

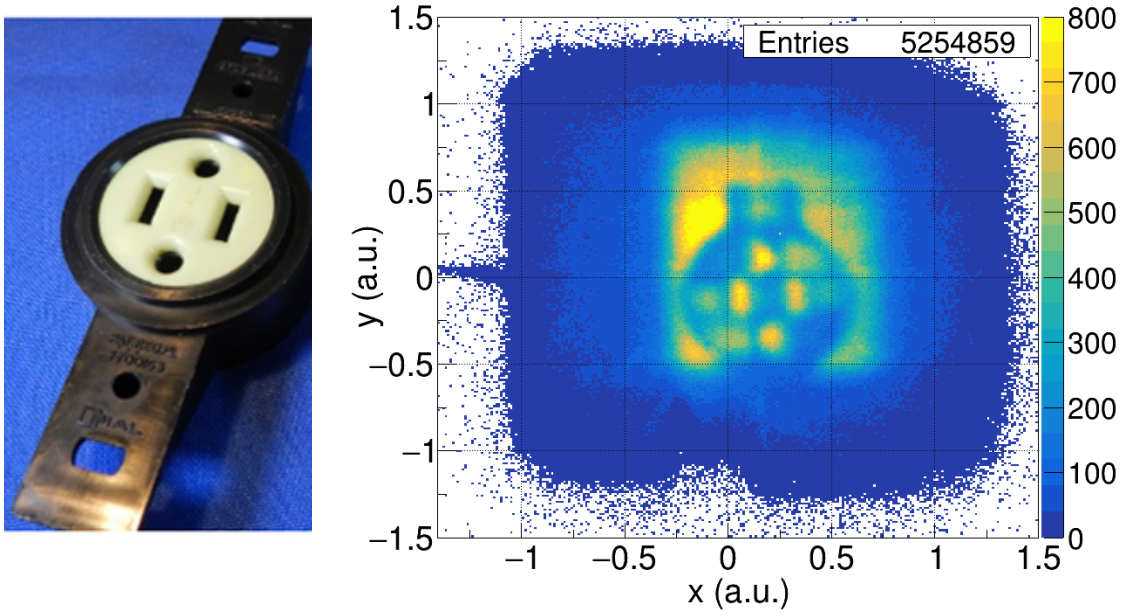

(a) (b)

Figure 6.1: Common vintage plastic power outlet (a) and the very preliminary neutron image obtained using a similar one for a $1\,\mathrm{h}\ 57\,\mathrm{min}$ run (b). There is some distortion at the bottom because of loose electrical conection, that was fixed later.

A vital information to be measured is the profile and intensity of the neutron beam. As presented in section 5.4, this neutron beam comes from AURORA's focusing silicon monochromator [89], which could result in differences in its intensity. The neutron beam was measured through a thin natural cadmium foil $\sim 0.4\,\mathrm{mm}$ thick fixed at the detector's aluminum lid to limit the acquisition rate, as discussed in sec. 5.3.1. The expected rate r_e after the foil can be evaluated using Eq. 2.19, which results about $1.2\,\%$ of the original flux ($\Phi \approx 6 \times 10^4\,\mathrm{n\,cm^{-2}s^{-1}}$), for this case. To estimate the expected rate one can consider the area A of the beam about $4\,\mathrm{cm} \times 8\,\mathrm{cm}$ (see Fig. 6.2b), the thickness x of Cd-Nat foil as $400\,\mu\mathrm{m}$, the event recording rate m ≈ 0.84 (see Fig. 5.15a) and the neutorn detection efficiency $\varepsilon \approx 3\,\%$, we can write:

$$r_e = \Phi_0 e^{-\Sigma x} A m \varepsilon \approx 613\,\mathrm{Hz}, \tag{6.1}$$

which agrees with the obtained rate[1]. The neutron beam image obtained is presented in Fig. 6.2 that also depicts its projections in the X and Y directions. As expected, the neutron beam is not homogeneous and presents a substantial decrease in intensity when moving away from the central region.

[1] the 182 927 events per 300 s results about 610 Hz.

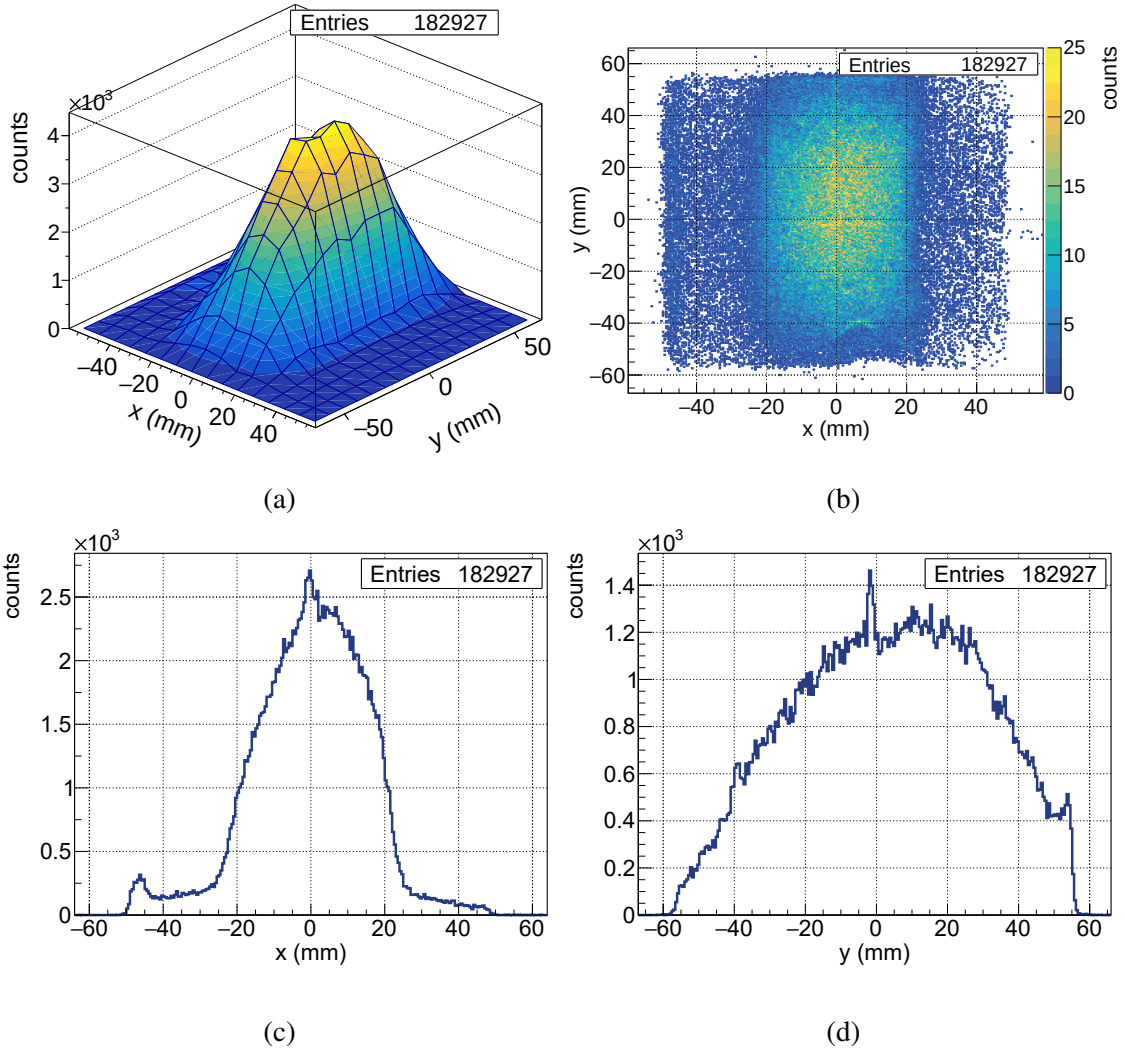

Figure 6.2: Obtained image of the beam plotted as a 3D surface (a) and a 2D histogram (b), with the respective projections in the X (c) and Y (d) directions for an $\sim 300\,\mathrm{s}$ run. There is a wide distribution along the Y direction.

The reason for the non-homogeneity is that this neutron beam was projected for neutron diffraction, presenting a focusing effect, as related by [89]. As we can see, this effect is more substantial in the Y direction, and the fact that the detector is not positioned at the sample's position magnifies the distortion. The peaks around $0\,\mathrm{mm}$ in Figs. 6.2c and 6.2d are due to some noise entering the acquisition in this preliminary test. It can be removed in offline analysis and was removed from the system in further runs by eliminating the noise.

6.2 Preliminary simulations

Using the integrated results of the dE/dx curves from SRIM simulation for the $^{10}B_4C$ conversion layer (Fig. 4.8) and for the gas (Fig. 5.3), we created preliminary simulations to understand the influence of several factors to be considered when constructing the detector. Despite not containing information about the neutrons energy, the energy spectrum of the ionizing products allow us to understand details about the working principle of our detector. For this purpose, we developed the code illustrated in Fig. 6.3.

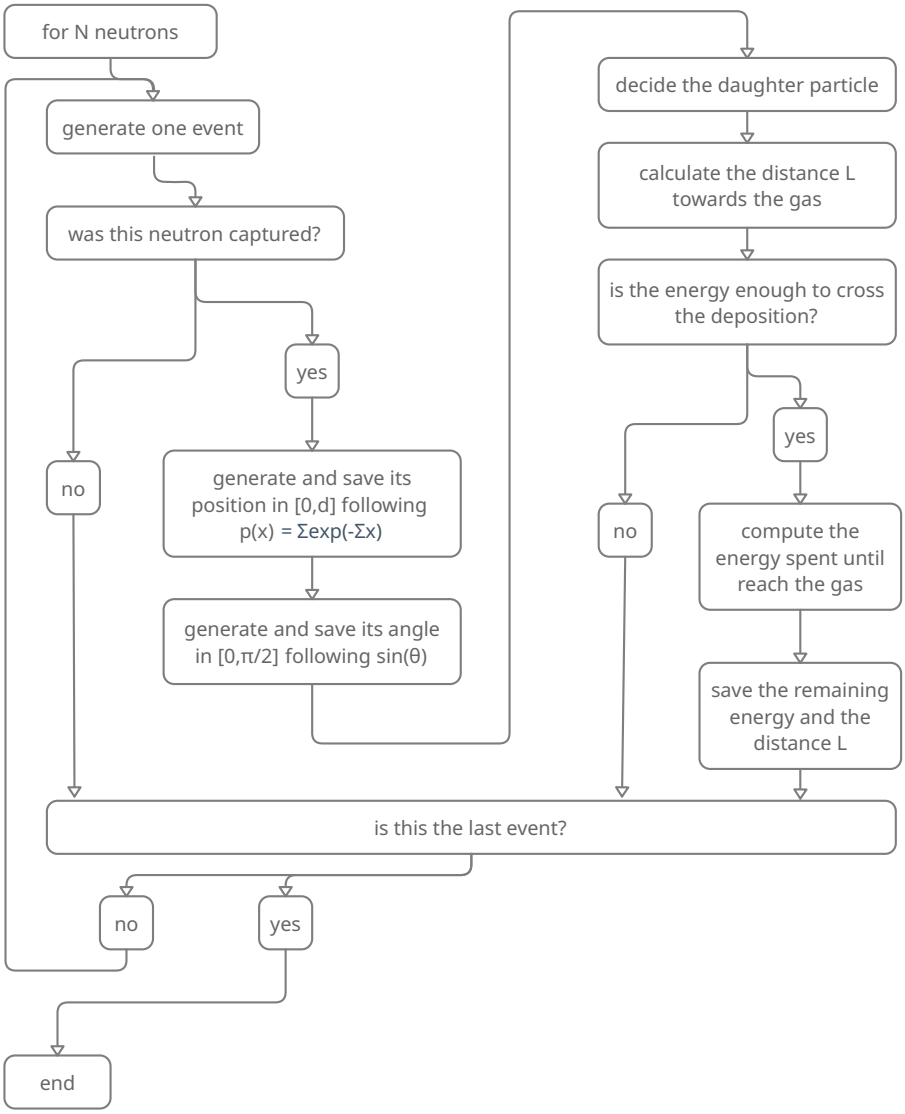

Figure 6.3: The structure used for the simulation of the energy spectrum of the products that reaches the drift zone. It is worth to note that the daughter particle decision follows the probabilities shown in Eq 2.12.

The energy spectrum for a $2.2\,\mu\mathrm{m}$ thick $^{10}B_4C$ deposition is shown in Fig. 6.4 for each product of the capture reaction. Thinner depositions result in lower efficiency and more well-determined energies while thicker depositions smooth the energy distribution, as shown in Fig. 6.5. As discussed in sec. 4.2, the efficiency decreases for depositions thicker than $\sim 3\,\mu\mathrm{m}$ because some percentage of the captured neutrons are not detected. In other words, this extra thickness lowers detection efficiency, removing neutrons (that are captured but not detected) off of the neutron beam. It implies that for thicknesses larger than $\sim 3\,\mu\mathrm{m}$, the shape of the energy spectrum of the products that enters the gas does not change, and its intensity decreases.

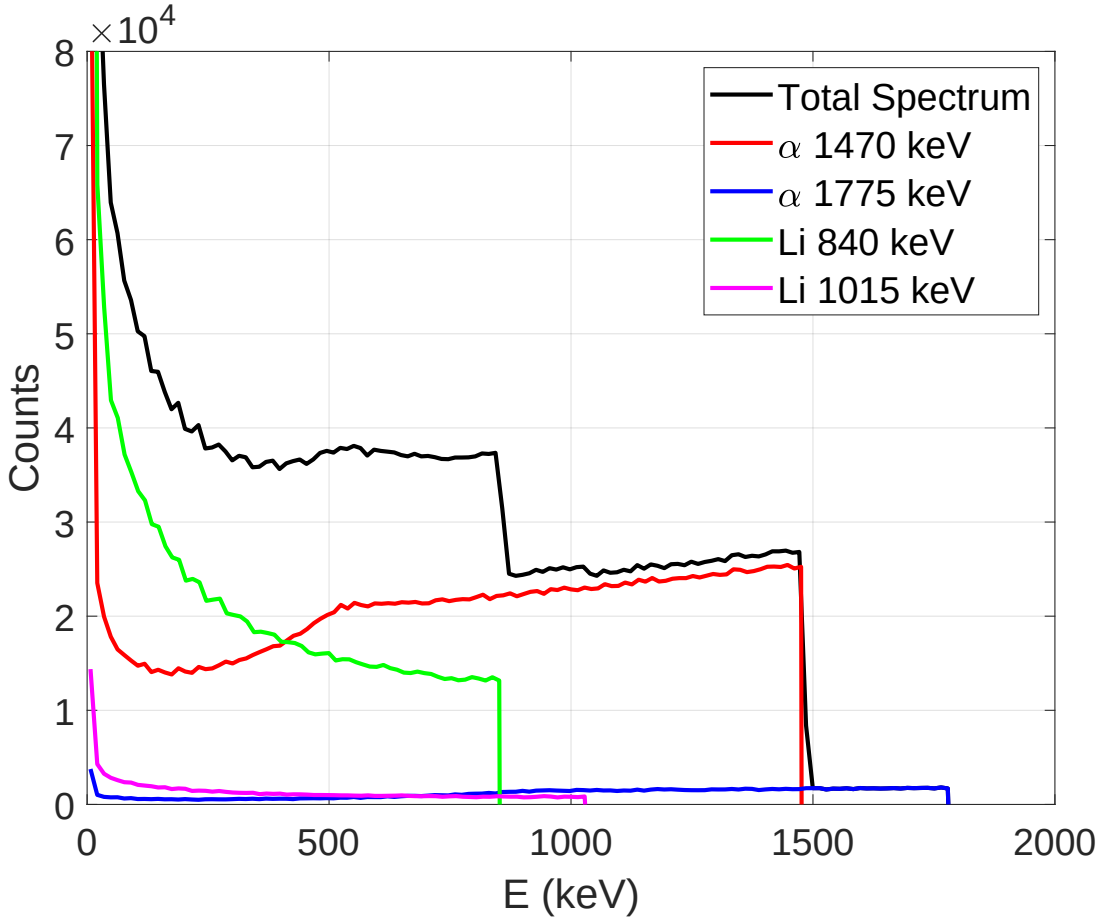

Figure 6.4: Spectrum of products entering the gas obtained simulating 1×10^8 neutrons using the algorithm shown in Fig. 6.3. Result for $2.2\,\mu\mathrm{m}$ thick $^{10}B_4C$ deposition.

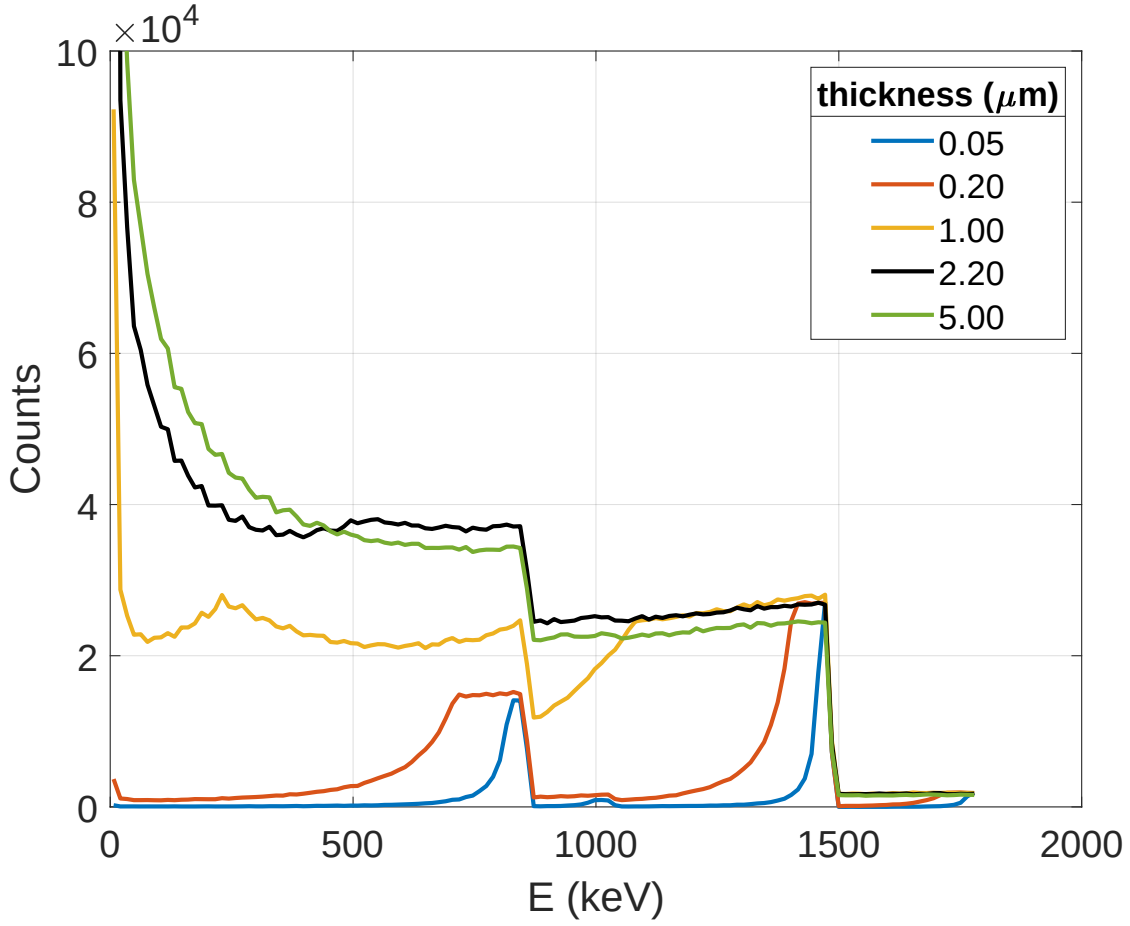

Figure 6.5: Total spectrum of products entering the gas obtained simulating 1×10^8 neutrons using the algorithm shown in Fig. 6.3, for different thicknesses.

After a glimpse of how the energy spectrum of the capture products that enter the drift zone looks like, it is also essential to understand the modifications imposed by the geometrical constraints[2]. We developed a second preliminary simulation, shown in Fig 6.6, to evaluate the spectrum obtained by the detector.

[2] i.e., the fact that the gaseous layer is not thick enough to absorb all the energy of the products.

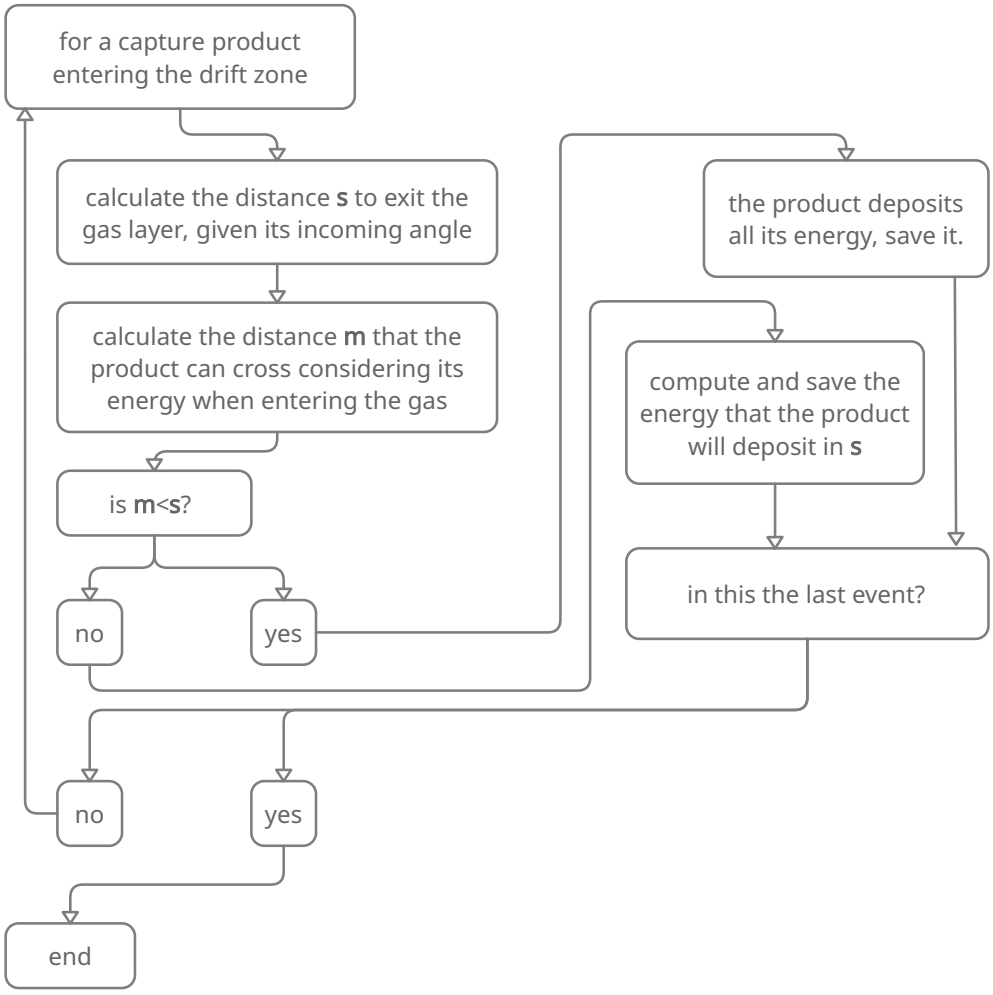

Figure 6.6: The structure used to simulate the energy spectrum obtained by the detector for a given drift zone depth. There is the possibility to consider a given energy resolution R when saving the events, providing a more accurate result.

The simulation of the detected spectrum is shown in Fig. 6.7, and considers $2\,\mathrm{mm}$ drift zone and the detector's energy resolution $R = 10\,\%\,\mathrm{FWHM}$, a reasonable initial value for these kind of detectors [82]. It means that each calculated value of energy E is registered as $E(1 + r\sigma_E)$, where r is a random number that follows a normal distribution (with $\mu = 0$ and $\sigma = 1$), and $\sigma_E = ER$, which is the definition of energy resolution.

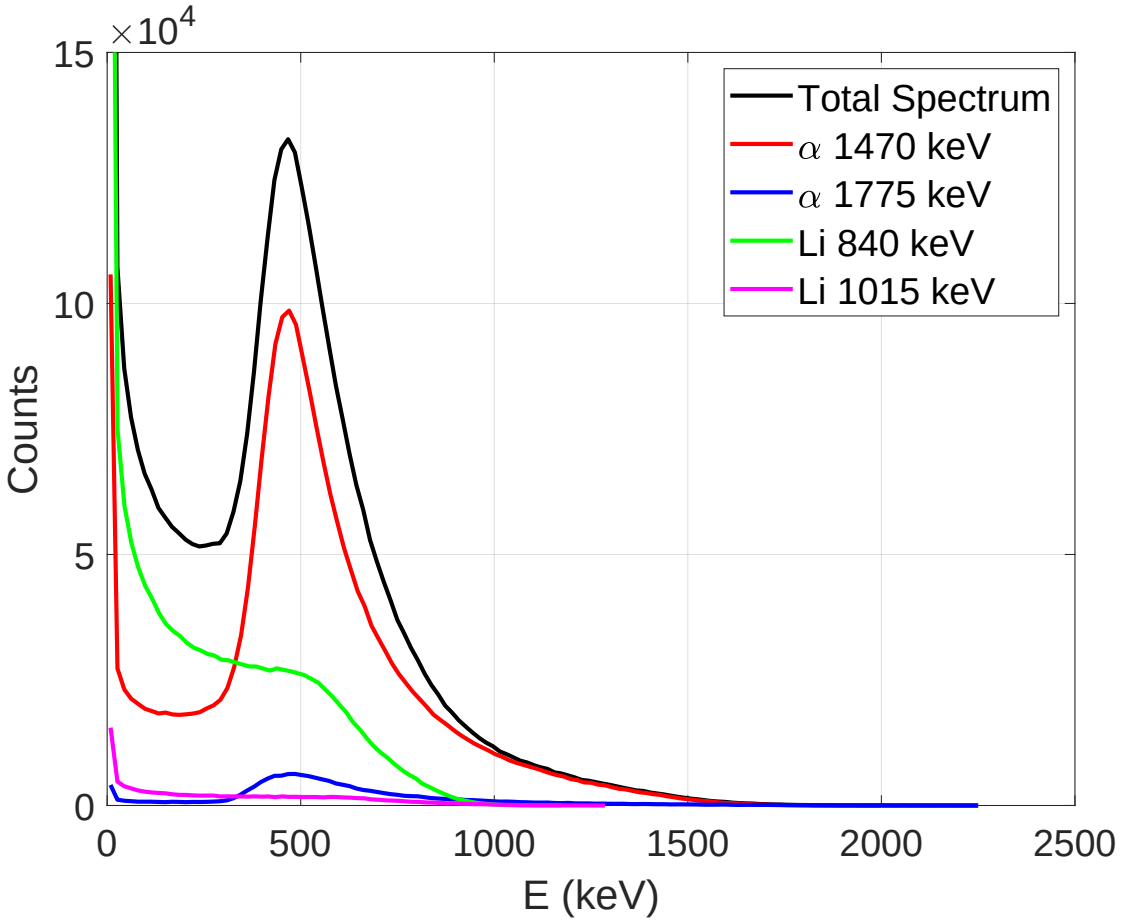

Figure 6.7: Energy spectrum deposited in the gas by the products of Fig. 6.4, using the algorithm shown in Fig. 6.6, for $2\,\mathrm{mm}$ drift zone, $10\,\%$ energy resolution.

Comparing the simulation with the experimental measurement, shown in Fig. 6.8, there is a fair agreement regarding the main structure of the energy spectrum, even though there are systematic differences for low energies and energies above about $500\,\mathrm{keV}$. It corroborates the versatility of this kind of preliminary simulation when planning the geometrical considerations of the detector, for instance.

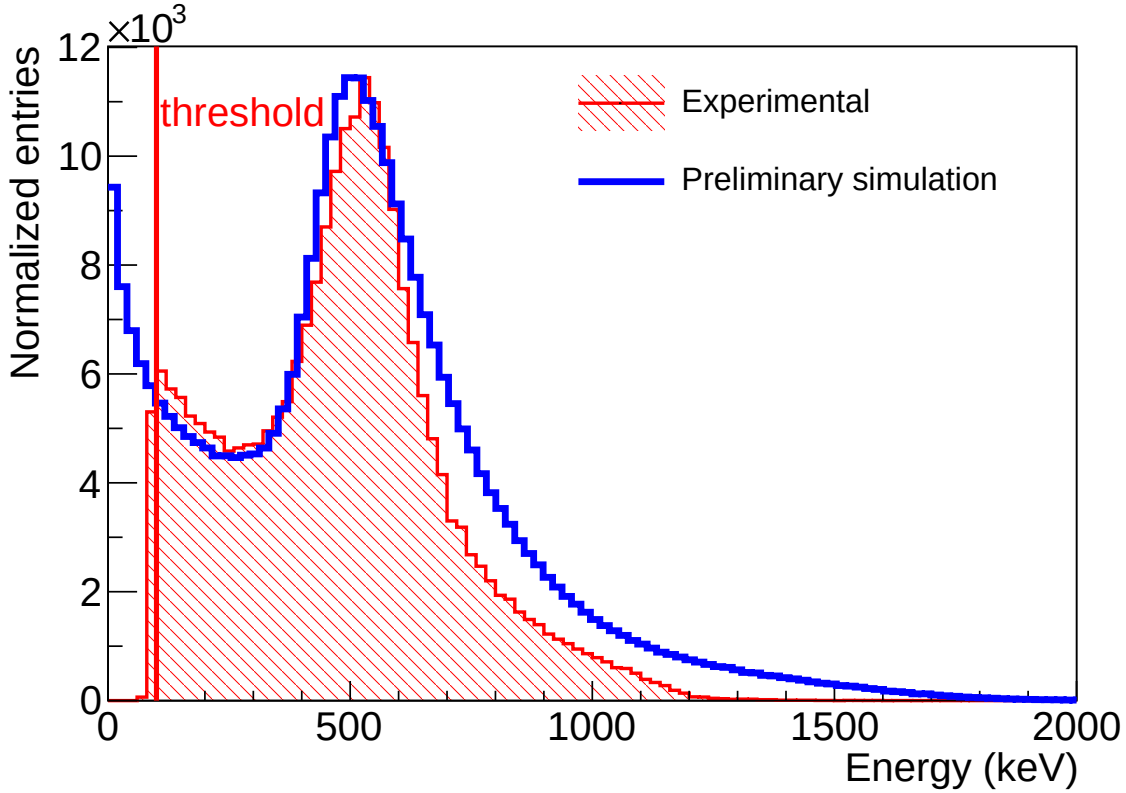

Figure 6.8: Comparison between the total simulated spectrum and the experimental one. The simulated spectrum was normalized to present the same peak height as the experimental one. It was also used to pre-calibrate the energy of the measured spectrum since its original unit is ADC channels.

The peak should be related to the geometric constraint imposed by the GEM, since it does not appear in the energy spectrum of the particles that comes off the deposition (Fig. 6.3). To check this assumption, the simulation can be extended for different drift zones, as shown in Fig 6.9.

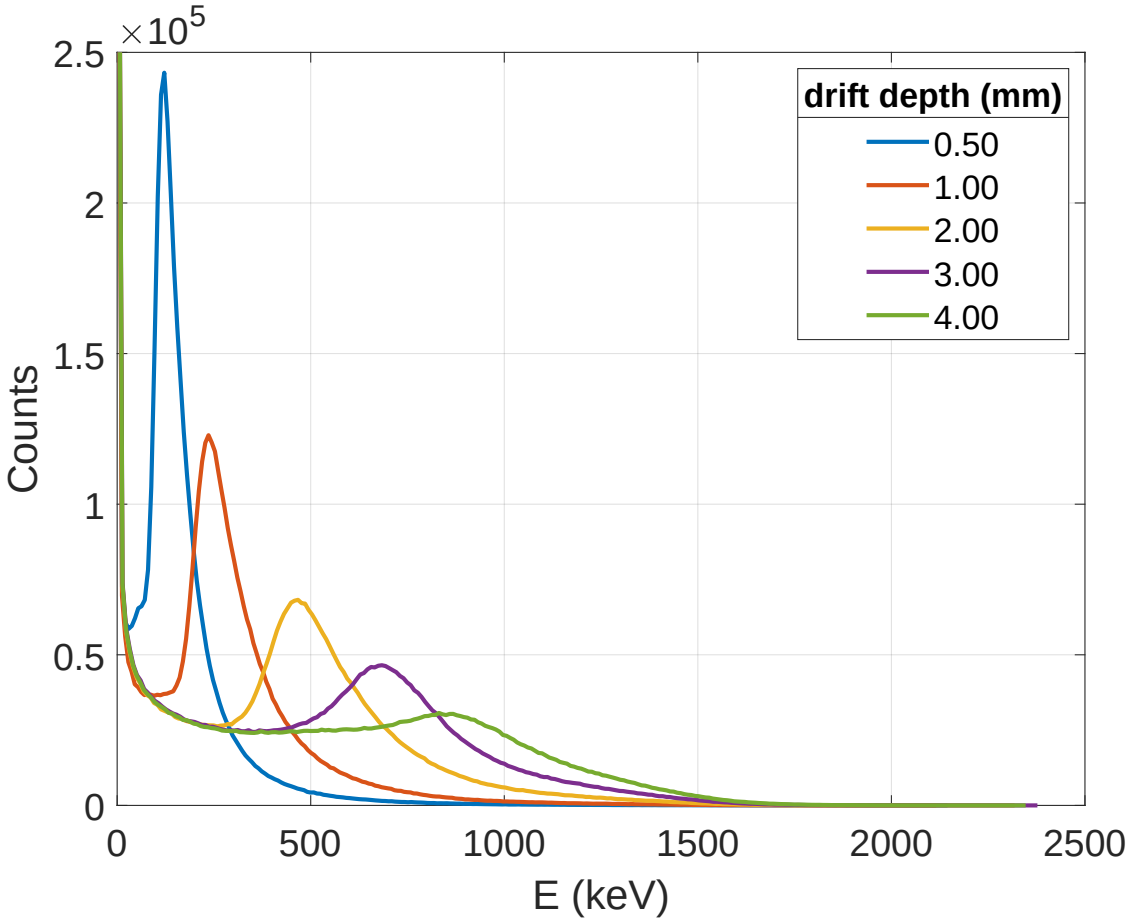

Figure 6.9: Simulated spectrum of the deposited energy in the gas, using the algorithm shown in Fig. 6.6, for $2.2\,\mu\mathrm{m}$ thick $^{10}B_4C$ deposition, for several drift depths, $10\,\%$ energy resolution, and 1×10^8neutrons.

As expected, small drift zones result in peaks with smaller energy and more counts because of the geometric constraint mentioned, as shown in Fig. 6.9. This is a significant result that shows the problem is understood, and it is possible to use this tool in further applications with different requirements.

The simulation of the energy spectrum for products entering the gas (see Fig. 6.3) considers that N neutrons interact with the detector (in our simulations N = 1×10^8). As we discussed (see sec. 4.2), about $7\,\%$ of these neutrons are absorbed, and only a part of them are detectable. We can also use the simulation to compute the detection efficiency. As mentioned, the detection efficiency is the number of products that escape the deposition divided by the total number of neutrons impinging on the detector. As shown in Fig. 6.10, the simulation closely agrees with the analytical result previously presented in Fig. 4.11, except for a slight systematic difference for thicknesses bigger than $4\,\mu\mathrm{m}$.

The preliminary character of these simulations lies in considering just one kind of

interaction and some simplifications. We did not account for recoils, direction-changing during elastic collisions, etc. This means that these results are intent on depicting the first-order mechanisms acting in the problem. We carried out these simulations for being a versatile (and relatively fast) way of obtaining first approximations to direct our planning. Naturally, further simulations are necessary for a better picture of the phenomena.

When comparing the preliminary simulations with more complex simulations carried out by other fellows from our research group, there was a reasonable agreement for thicknesses smaller than $2\,\mu\mathrm{m}$ but overestimated (around $13\,\%$) the efficiency for larger thicknesses. Using Geant4 [93] simulations with the physics list *QGSP_BERT_HP*, which has high precision models for low energy neutrons [94], Maria Monalisa, a fellow of our group produced the efficiency simulation [95] labeled as "Geant4" in Fig. 6.10.

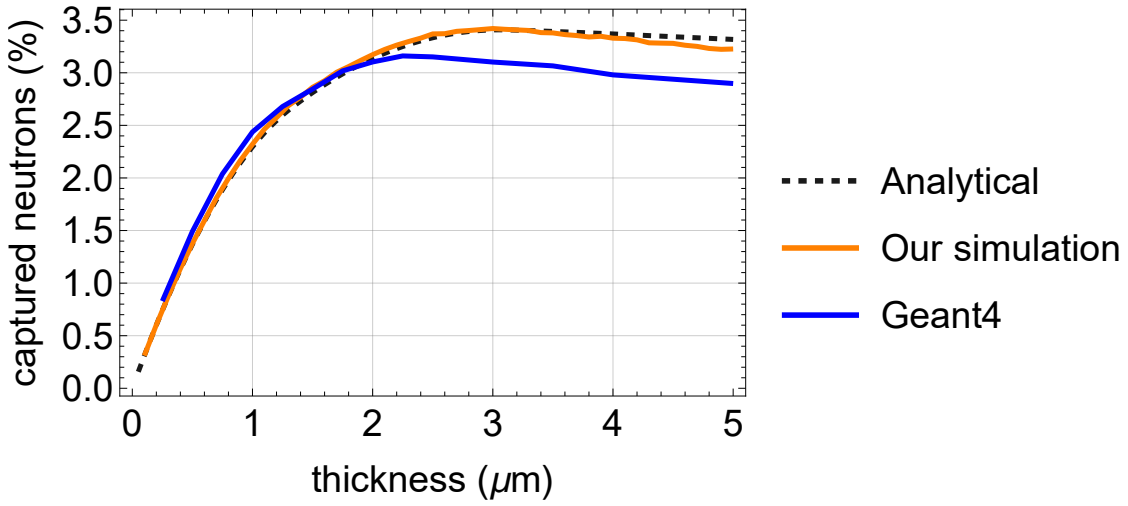

Figure 6.10: Simulated efficiencies using the algorithm illustrated in Fig. 6.3 and using Geant4, plotted over the analytical dependency computed from Eq. 4.7. The preliminary simulations generally agree with the analytical prediction. Nevertheless, Geant4 is a much more reliable framework and indicates around $2.52\,\mu\mathrm{m}$ as the optimal thickness.

It is also important to compare the experimental energy spectrum with more consolidated simulations, this comparison was made using a Geant4 simulation [96] for the expected energy spectrum produced by Renan Felix, from our research group. This simulation used the Livermore [94] model, a low-energy electromagnetic model. It took into consideration the interaction between the neutron and the deposition and the interaction of the ionizing products with the deposition and the drift zone. We used this result to pre-calibrate our energy spectra. The process consists in aligning the experimental peak together with the simulated one, using the mean of a gaussian curve fitted in each one to evaluate the scale factor. The final result is presented in Fig 6.11.

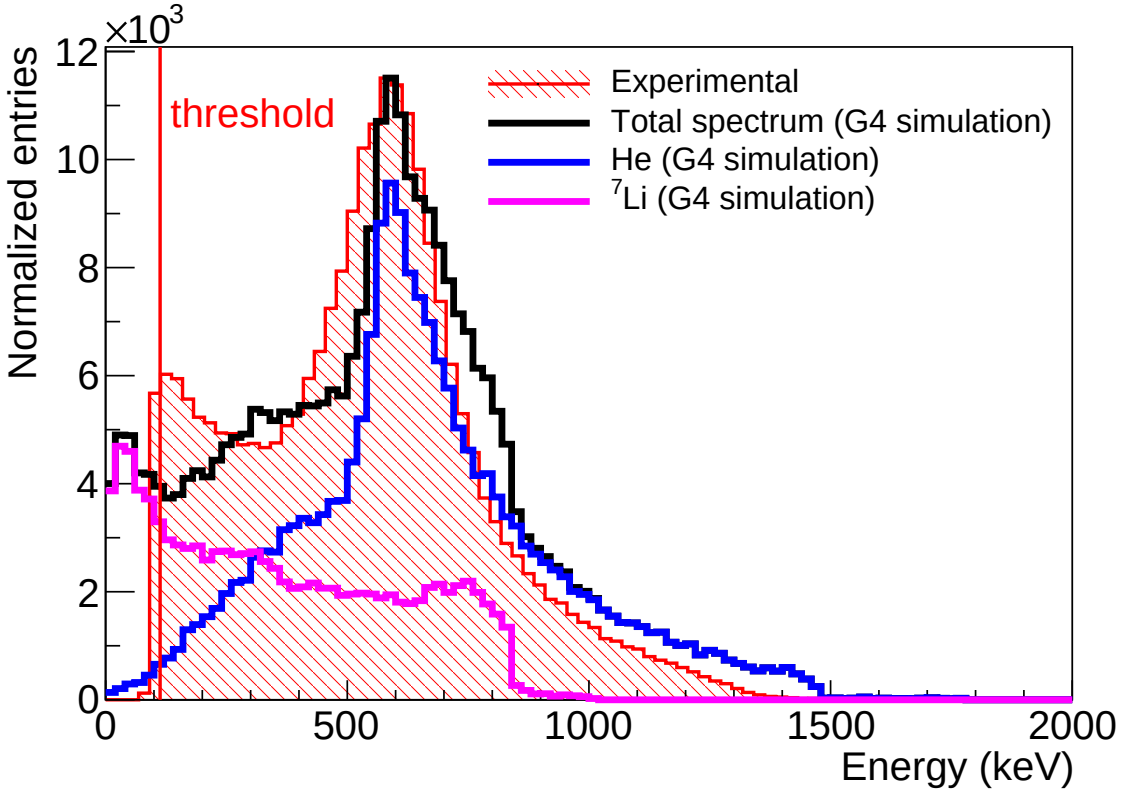

Figure 6.11: Geant4 simulated [96] spectra used to pre-calibrate the experimental one. The simulation, which has $87\,874$ entries, did not include the effect of the detector finite energy resolution. The spectra were normalized in relation to the maximum value of the experimental one.

Even though Geant4 is not commonly used for interaction of ionizing particles in gaseous environments, a reasonable agreement was obtained. The advantage of its use regards the nuclear interaction between the neutron and the absorber that is much more sophisticated. We will not discuss the details in this work. Nevertheless, there was consistency between the simulations, and it is possible to argue that the primary mechanism that originates the peak is due to the geometric configuration of the detector. It is also reasonable to expect the peak lying between $400\,\mathrm{keV}$ and $700\,\mathrm{keV}$.

6.3 Gain stability

As discussed in sec. 3.5.3, variations in temperature and pressure affect the detector gain [62, 82, 97, 98]. This consideration is essential because gain changes imply variations in the efficiency since they drift the energy spectrum. The analysis method we present in this section aims to spot gain variations to monitor the detector's stability. To monitor possible variations, we plot the energy spectrum, i.e. the histogram of the signal collected at the bottom of the lower GEM, as a function of the time, as shown in Fig. 6.12a. This

plot is then divided into batches of a few minutes, each set corresponding to the energy spectrum obtained during those minutes. For each batch, it is possible to get the peak of its spectrum using the peak identification algorithm [99–101] implemented in TSpectrum class within the ROOT framework [102]. With the peak information for each batch, we proceed to analyze their dispersion through their histogram. The complete analysis is depicted in Fig. 6.12.

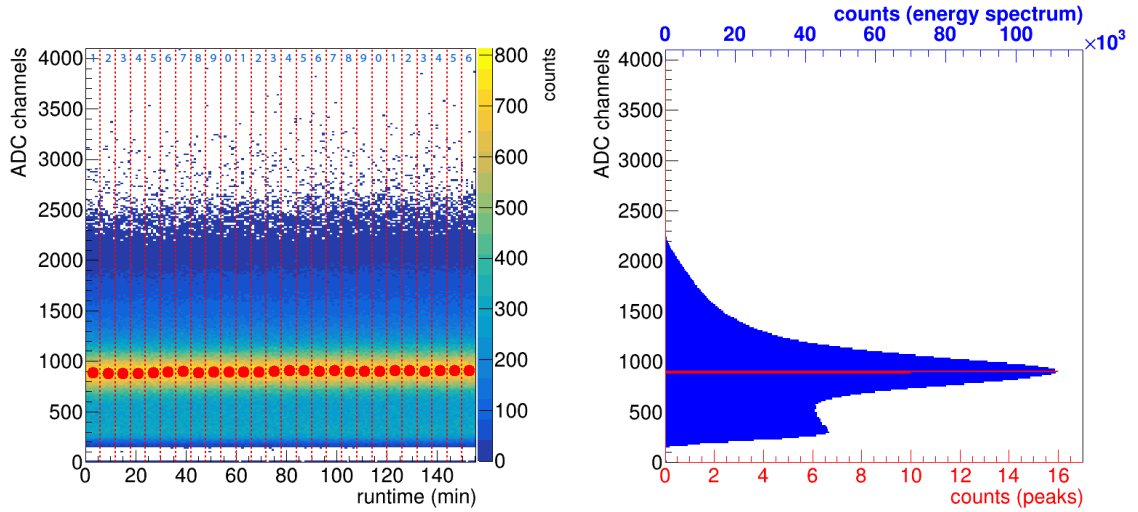

(a) (b)

Figure 6.12: The stability analysis consists in computing the energy spectrum in batches of a few minutes. The division is represented as the dotted red lines in (a), while the red points are the spectrum peak location for each batch. The histogram of these peaks positions is plotted in red (b) on top of the histogram for the whole run, in blue. There were 26 peaks for the presented analysis whose distribution had a standard deviation equal to 9.2 ADC channels.

When there are no noticeable drifts in the gain, like the case shown in Fig. 6.12, the distribution of the position of peaks of the batches is narrow, with variations caused purely by statistical effects inherent to any measurement. This behavior is seen by superimposing the distribution of the batches' peaks with the energy channel spectrum for the whole run, as depicted in Fig. 6.12b. In this case, the standard deviation of the distribution of the batches' peaks resulted in 9.2 ADC channels[3].

There are two kinds of behaviors that we can quickly identify from this analysis: variations due to atmospheric changes or due to electronic problems. The main difference between the two of them is the velocity of change.

Electronic problems usually manifest quickly compared to the run time. They are often generated by hardware problems of our electronic system, such as exploding capacitors, resistivity change of the analogic components due to the joule effect, etc. An

[3] we use a 12-bit ADC, which means we have 4096 bins between 0 V and 10 V.

example of real problem case is illustrated in Fig 6.13, where we can spot a significant variation around minute 12. The quick-change of gain and the drift of the threshold indicates electronic problems since the variations in temperature and pressure are expected to happen smoothly. Besides the odd shape of the peaks distribution, the issue is also observed when calculating the standard deviation of the peaks, in the case of Fig. 6.13 equals 70 ADC channels.

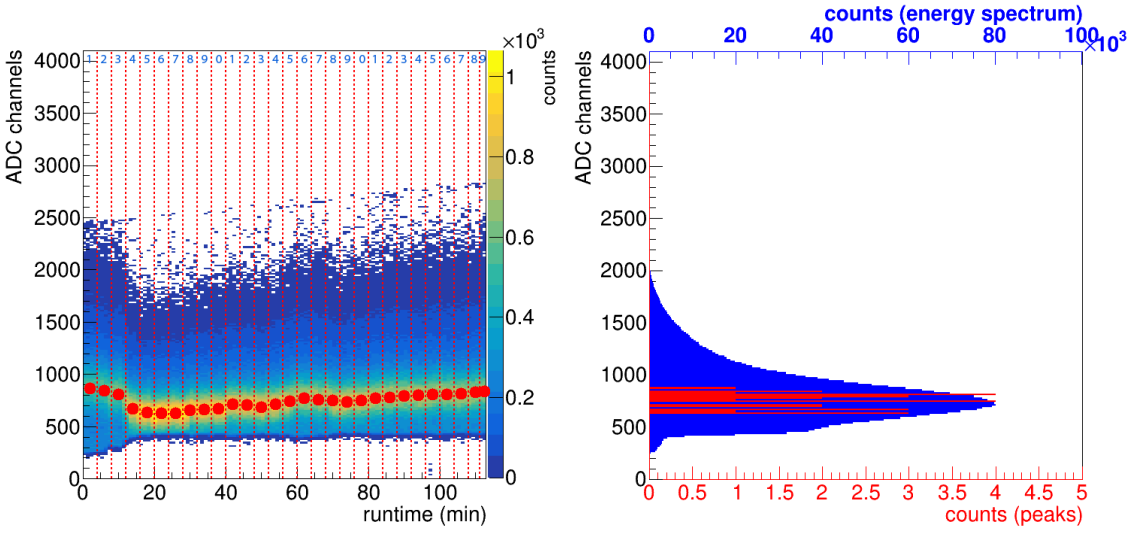

(a) (b)

Figure 6.13: Stability analysis for a run that presented electronic problems. It is easily noticed by the quick changes in the gain and particularly by the unexpected variation of the threshold around minute 12 (a). The run spectrum has a different shape in the first 500 ADC channels and the 29 peaks of this analysis presented a standard deviation equals to 70 ADC channels. (b)

On the other hand, atmospheric variations imply changes in the property of the gas, such as time of drift and recombination rate, as seen in sec. 3.1.1. This particular kind of variation happens slowly. Since our detector did not suffer from this behavior, we simulated a gain drift of 20 % for the run shown in Fig. 6.12. The simulation is presented in Fig. 6.14 and consists of artificially changing the gain with time. Our purpose, in this case, is to study the structure formed for cases where the gain suffers a slow drift, as the atmospheric variations do.

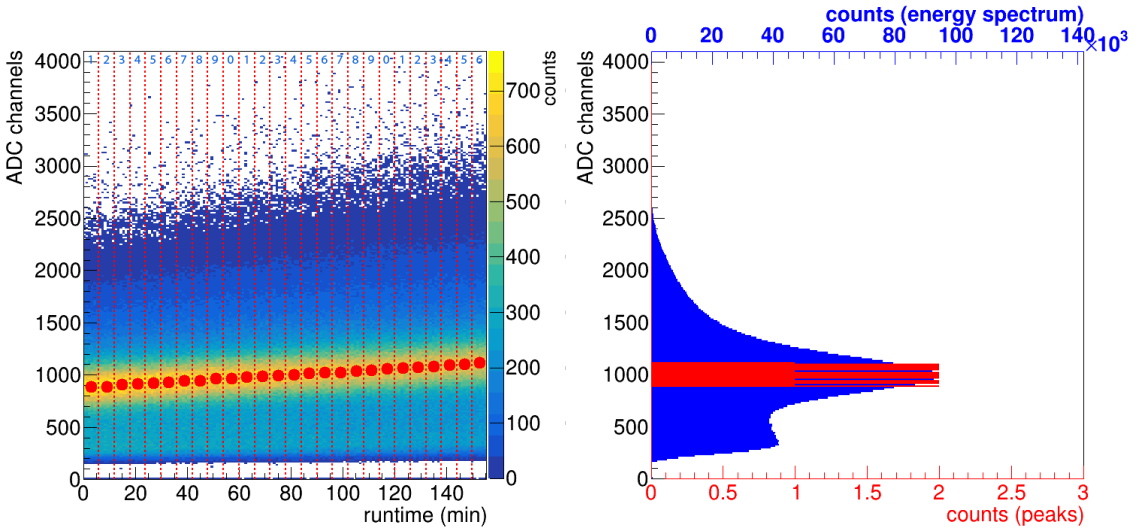

(a) (b)

Figure 6.14: Stability analysis for a simulation of gain linear drift of $20\,\%$. The batches have 6 minutes each, generating 26 spectra. We can quickly notice the drift using the time plot (a). The peaks distribution is also wider, and in this case, calculating the standard deviation does not make sense since it is not randomly distributed (b).

It is interesting to note that the overall spectrum does not visually change (see Fig. 6.14b), but the series of peaks distribution is monotonic and wider. Therefore, it does not make sense to compute the standard deviation for the peaks distributions since it does not follow a normal distribution.

This analysis can be applied to every run in order to check the stability of the detector. As mentioned, its importance lies in the fact that gain variations drifts the energy spectrum and changes the detector efficiency, which is bad for the detector.

6.4 Spatial resolution

Since the project aims to produce a position-sensitive neutron detector, measuring the spatial resolution is crucial. In this section, we present the results for the spatial resolution of the detector, measured by two different methods. However, the first compulsory step is the geometric calibration of the detector, discussed in sec. 4.3, allowing us to determine positions in a know length unit. An example of calibrated run is shown in Fig. 6.15, below.

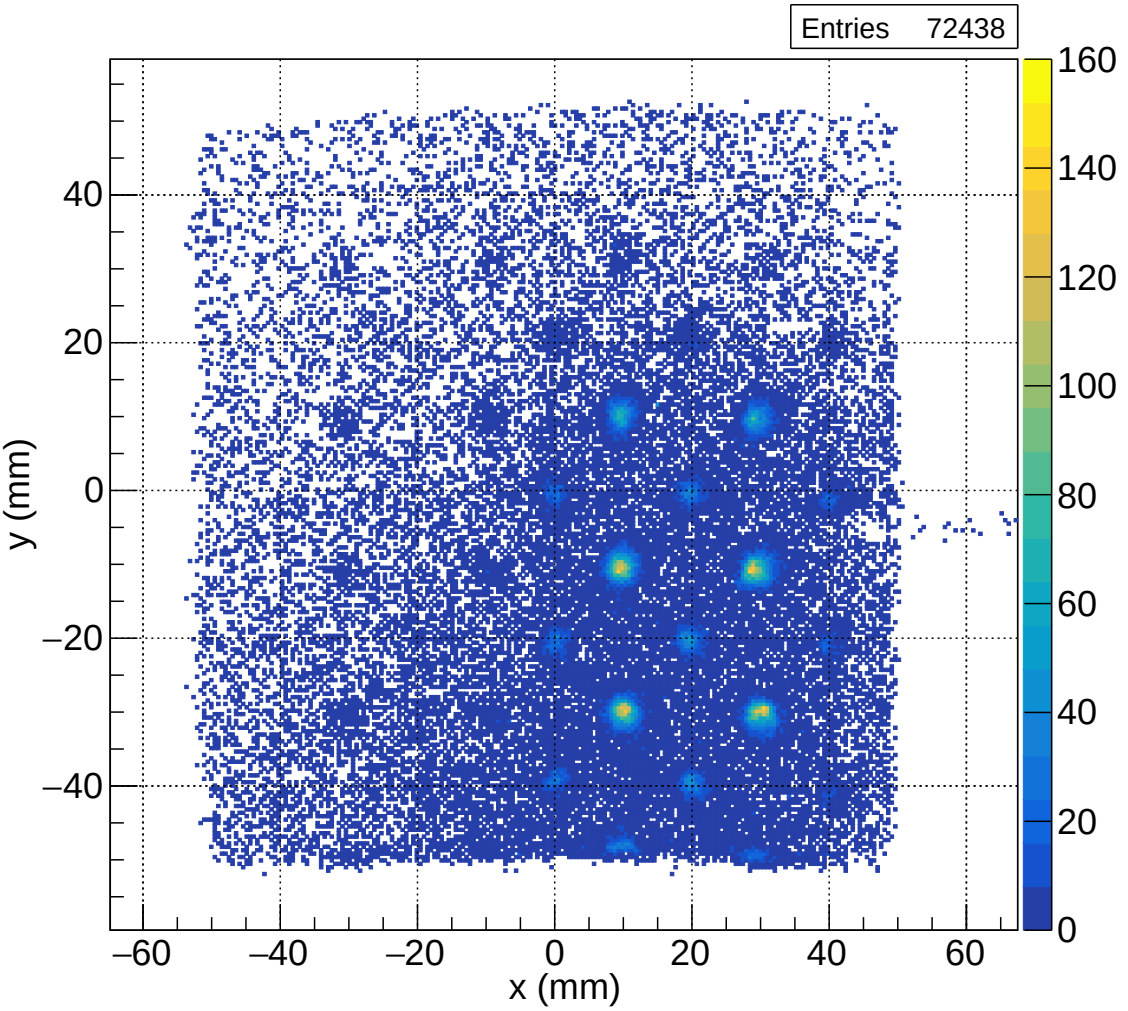

Figure 6.15: Example of calibrated neutron image produced with the Cadmium mask E, shown in Fig. 4.18, for a $10\,\mathrm{min}$ run.

As mentioned in sec. 4.3, the relashionship between the arbitrary units and mm is linear, given by: $C[\mathrm{mm}] = A \cdot C[\mathrm{a.u.}] + B$, where C is a given coordinate expressed in arbitraty unit (a.u.) or mm. The obtained calibration values for Fig. 6.15 was $A_x = 55.1\,\mathrm{mm\,a.u.}^{-1}$ with $B_x = 1.3\,\mathrm{mm}$ for X direction and $A_y = 49.1\,\mathrm{mm\,a.u.}^{-1}$ with $B_y = -0.6\,\mathrm{mm}$. With the calibrated neutron image, it is possible to measure the spatial resolution.

The first method used to measure the spatial resolution was the “edge method”. As discussed in sec. 4.1.3, the projection of the image produced by the edge provides us information about the detector’s spatial resolution. For an ideal detector with infinite spatial resolution, this image converges to a perfect step.

It is important to note that even if it were possible to use an ideal readout with infinite

spatial resolution, the projection of the neutron image of the edge, produced by our prototype, would not be a perfect step. This happens because the products of the capture reaction does not interact punctually as the neutron does. This means that one of the factors that limit the spatial resolution is the dispersion of these products. A way to overcome this limit is to reconstruct the products trajectory, but that imposes extra requirements such as high-end electronics and a bigger drift region, to create a time projection chamber (TPC) system that can reconstruct the point where the initial capture took place. Another possibility is to reduce the drift zone size, which would also raise discharge probability.

Sharp edges cadmium masks are easily assembled from $1\,\mathrm{mm}$ thick cadmium foils since they can be made overlapping several rectangular pieces, as shown in Fig. 6.16a. Considering that the neutron beam we used has a width limited to about $40\,\mathrm{mm}$, it was necessary to split the image of oversized masks in different runs, as shown in Fig. 6.16b and 6.17.

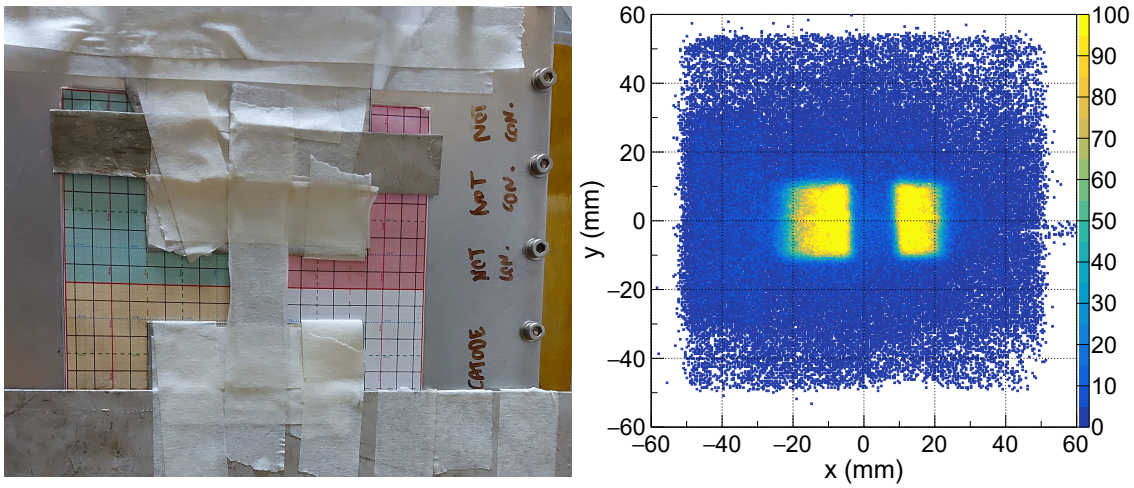

(a) (b)

Figure 6.16: Sharp edges cadmium mask on top of the detector (a) and its neutron image for a $5\,\mathrm{min}$ run (b).

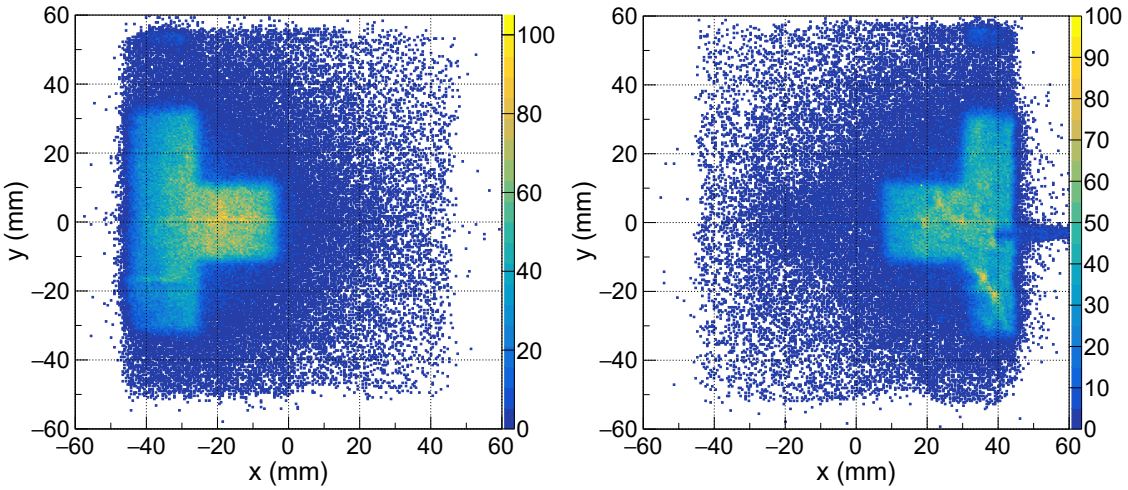

(a) (b)

Figure 6.17: Images were obtained with the same masks as Fig. 6.16, moving the detector to the right (a) and left (b) regarding the beam for 5 min runs. In these runs, we covered the beam with a thin cadmium foil to reduce the count rate. Some marks present in this foil appear as the brighter spots in (b).

To illustrate the edge method, we selected two rectangular regions of Fig. 6.16b, shown in Fig. 6.18, as the red and cyan rectangles over the Figure. Vertical edges are used to obtain the spatial resolution in the X direction while the horizontal edges in the Y direction. The selected regions were projected in the direction of their wider side, where we fitted the ESF (see Fig. 6.19).

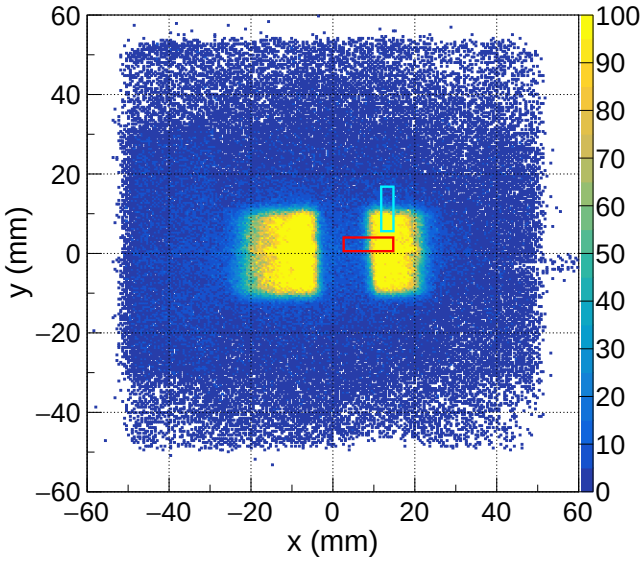

Figure 6.18: Image (5 min run) with sharp edges produced using cadmium masks with marked regions to apply the edge method for evaluating spatial resolution.

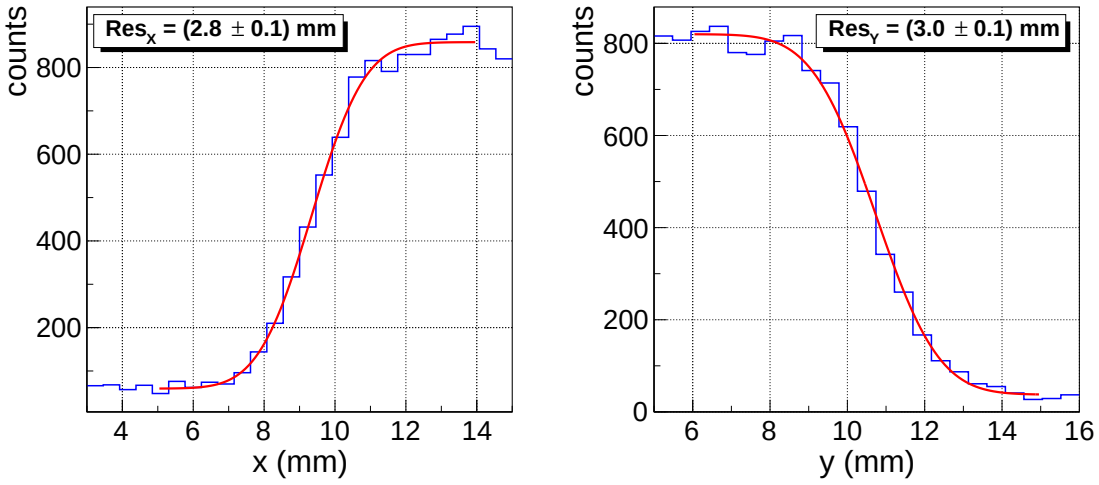

(a) (b)

Figure 6.19: Fit of a step function erf (a) and erfc (b) for the regions of the Fig. 6.18 marked in red (a) and cyan (b). The resolution obtained for the red (in the X direction) and cyan (in the Y direction) regions in the Fig. 6.18 were $2.8(1)\,\mathrm{mm}$ and $3.0(1)\,\mathrm{mm}$, respectively.

The ESF fitted for the case presented in Fig. 6.19 was proportional to the *erf* function, defined by [102, 103]:

$$erf(p) = \frac{2}{\sqrt{\pi}} \int_0^p e^{-t^2} dt, \tag{6.2}$$

or its complementary $erfc(p) = 1 - erf(p)$, where

$$p(x) = \frac{x - \mu}{\sqrt{2}\sigma}, \tag{6.3}$$

for the X direction, which is analogous to the Y direction. Defining p as in Eq. 6.3 relates it with the parameters of the PSF gaussian-equivalent function, as discussed in sec. 4.1. The resolution is given by Res = FWHM $\approx 2.355\sigma$, as noted in Eq. 4.2.

The use of these simple cadmium masks easily allow performing a mapping of the spatial resolution, as shown in Fig. 6.19. This is an essential procedure because it allows us to identify possible distortions in the image introduced by irregularities in the resistive chains.

We prioritize mapping the central area of the detector since it is usually the most important, given that the borders have expected distortions, and can easily be measured using the central region of the beam. The obtained resolutions (in millimeters) are presented in Figure 6.20. We considered the uncertainties equal to the standard deviation of the obtained values since we expect a homogeneous spatial resolution throughout the

whole central region of the detector.

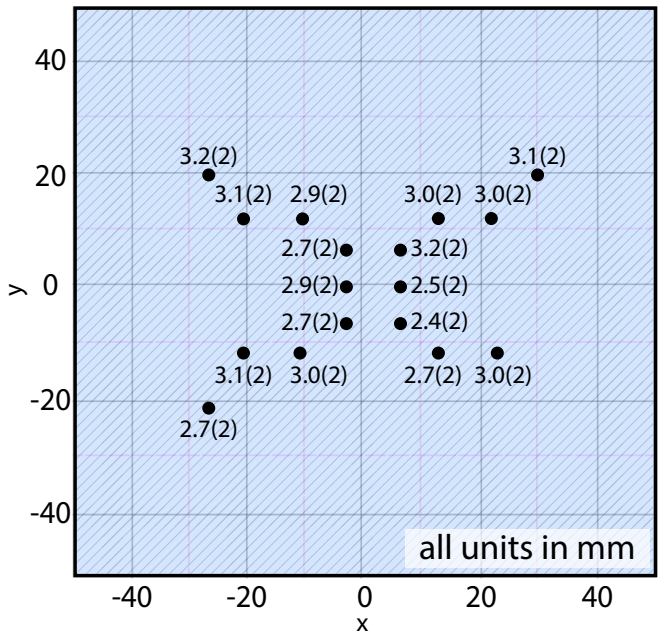

Figure 6.20: Regions of the readout plane with its spatial resolution, in millimeters. The analysis focused on using the central area of the neutron beam since its homogeneity is not preserved far from the center.

The second method to measure resolution consisted of analyzing the dependence between the full width at half maximum (FWHM) of projections of circular regions and the diameter of these regions. In the X-direction, the ideal projection of a circular homogeneously illuminated area with radius R is given by

$$P_j(x) = \int_{-\sqrt{R^2-x^2}}^{\sqrt{R^2-x^2}} dx = 2\sqrt{R^2+x^2}, \tag{6.4}$$

which is also valid for to the Y-direction by changing x for y. In our case, the problem is discrete, since the readout has 256 stripes for each direction. Considering a circular area with a $4\,\mathrm{mm}$ diameter, in order to check our conclusions, we performed a quick simulation shown in Fig. 6.21, illustrating how the ideal projection would look like.

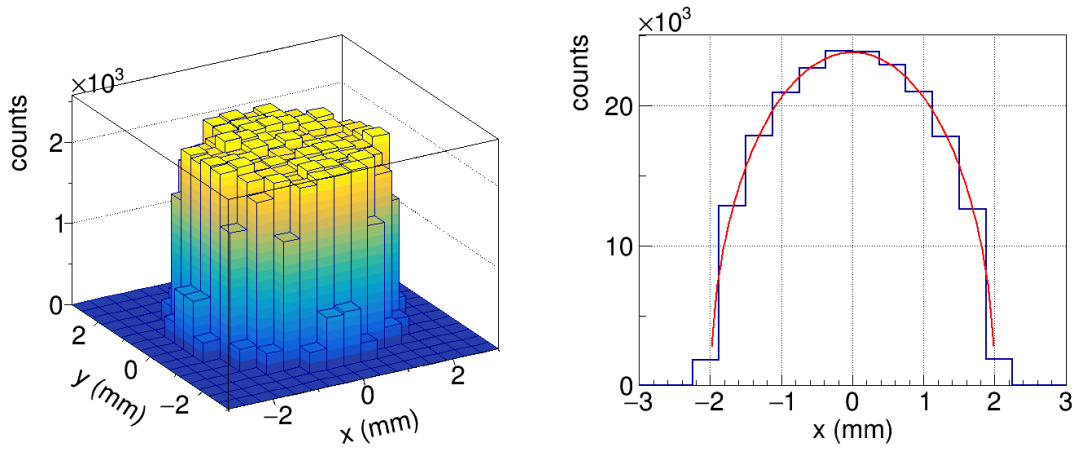

(a) (b)

Figure 6.21: Simulation with 2×10^5 entries of a uniform distribution over a $4\,\mathrm{mm}$ diameter circular region as seen by an ideal detector of 256×256 strips covering an area of $100\,\mathrm{mm} \times 100\,\mathrm{mm}$ (a). The figure (b) shows the projection along the X direction of (a); the distribution was fitted with a curve proportional to Eq. 6.4, providing $r = 1.994(5)\,\mathrm{mm}$.

However, the actual projection we measured results from the convolution of the profile function $P_j(x)$ with the unknown PSF of our detector. Even though the PSF is unknown, it is reasonable to consider it a gaussian function since the definition of spatial resolution purely relies on the FWHM. In other words, for practical reasons, the PSF can be thought of as the equivalent Gaussian function representing the FWHM that will define the spatial resolution for our detector. We can write the measured projection as

$$P_{meas}(x) = (P_j \circledast g)(x) := \int_{-\infty}^{\infty} f(\tau) g(x - \tau, \sigma) d\tau, \tag{6.5}$$

where g is the gaussian function, PSF of our detector, centered at zero. Note that g also depends on σ, which for the gaussian curve is related with the FWHM through Eq. 4.2. Following from the previous results, assuming σ such that the spatial resolution equals $3\,\mathrm{mm}$, we evaluate the projection $P_{meas}(x)$ numerically for different diameters, as pictured in Fig. 6.22. We also noted the FWHM for each projection. One can see that the FWHM converges to spatial resolution.

The FWHM function is also numeric and can be applied to the obtained projection P_{meas} for different holes to understand the convergence better. Considering the same detector with the spatial resolution equals $3\,\mathrm{mm}$, we evaluated this dependence, shown in Fig 6.23.

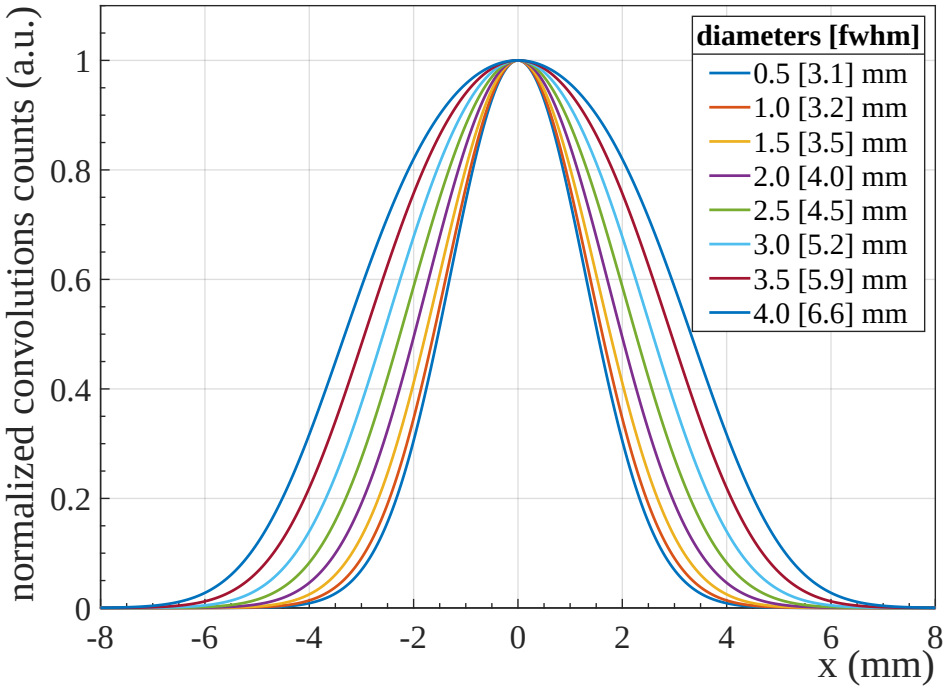

Figure 6.22: Numerical calculation of the measured projection function $P_{meas}(x)$ computed to holes with different diameters, as seen from a detector with a spatial resolution of $3\,\mathrm{mm}$. The legend also presents the FWHM for each curve. The values converge to the spatial resolution.

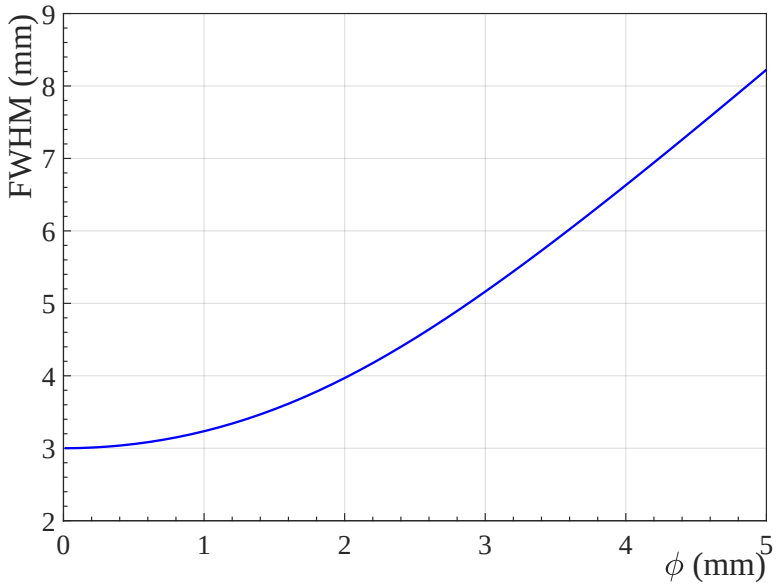

Figure 6.23: The dependence between FWHM of the projection function $P_{real}(x)$ for a given circular area and the area diameters for a detector with $3\,\mathrm{mm}$ spatial resolution.

It is possible to fit the dependence shown in Fig. 6.23 to experimental data. To obtain

the circular projections, we used the cadmium masks with different hole patterns, namely: masks A, B, and C, shown in Figs. 4.13, 4.14, and 4.15, respectively. We select the regions containing the holes, as in the Fig.6.24, and project them in x and y directions, as presented in Fig. 6.25.

As discussed, the projections of the circular region are the function $P_{meas}(x)$. Nevertheless, as we are interested in the FWHM, we fit a gaussian function to these projections. There is an excellent agreement to the gaussian function for all the regions we projected. We used projections from runs taken on different days. The amount of obtained data for each hole of each diameter is given in Table 6.1. Since the sets of data used are small samples, the FWHM uncertainty for each diameter is the standard deviation of the data for that role, corrected by t-Student statistics, as follows:

$$\sigma_* = \sigma \frac{\mathcal{P}(0.683|\text{Dof})}{\sqrt{\text{Dof}+1}}, \tag{6.6}$$

where σ_* is the corrected standard deviation, σ is the classic standard deviation, Dof is the degree of freedom for each set (the number of values in the set minus one) and $\mathcal{P}(t|\nu)$ is the value for a two-sided t-distribution with ν degrees of freedom. The value 0.683 is approximately the significance level provided by the $\pm\sigma$ interval for a normal distribution. The FWHM used is the average over the set for each diameter.

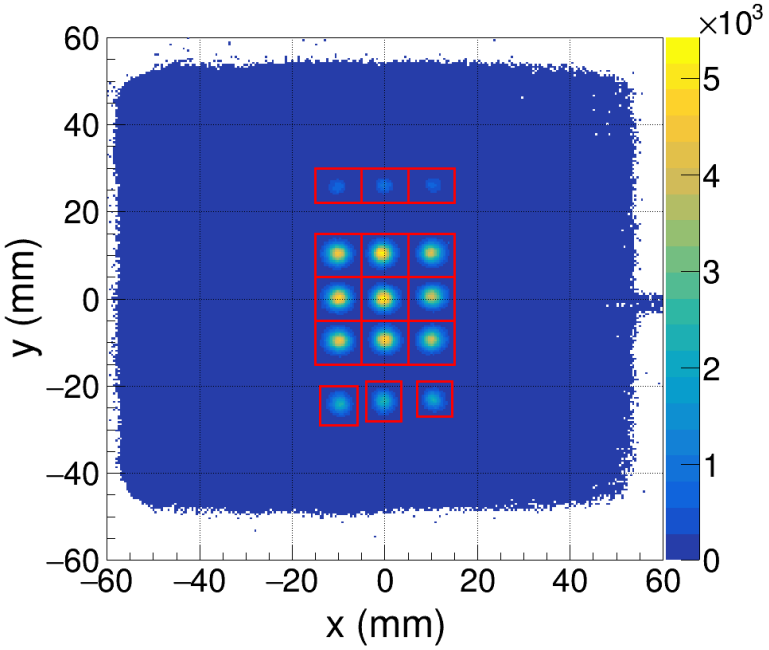

Figure 6.24: Neutron image of the cadmium mask A for a $2\,\text{h}\ 35\,\text{min}$ run, shown in Fig. 4.13, with the areas defined to project each hole in red.

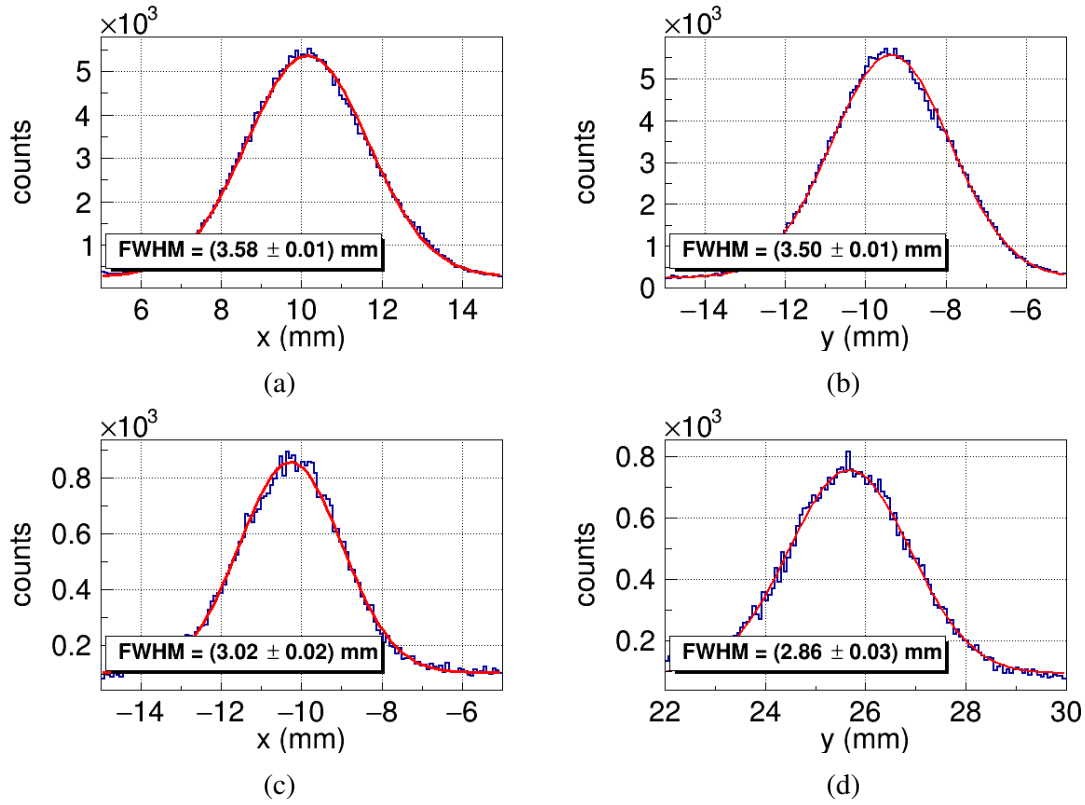

Figure 6.25: Example of projection for two holes of the cadmium mask presented in Fig. 6.24 with the fitted gaussian: X projection for a $3.5\,\mathrm{mm}$ hole (a), Y projection for the same hole (b), X projection for a $1.5\,\mathrm{mm}$ hole (c) and the Y projection for the same hole (d). It is noticeable that the FWHM for the smaller hole is closer to $3.0\,\mathrm{mm}$, the resolution obtained with the edges method.

Table 6.1: Number of data-sets used for each hole diameter.

ϕ (mm)	0.5	1.0	1.5	2.0	2.5	3.0	3.5	4.0
#	3	16	7	26	6	2	18	2
masks used	B	B,C,E	A,C	D,E	A	D	A	D

It is important to note that taking these data is a laborious process for several reasons, such as the choice we made to discard too marginal regions of the neutron beam or the long time needed to get enough counts for the small holes. The time required for imaging the small holes (tipically couple hours) was the reason why we just used the central holes of mask B for the $0.5\,\mathrm{mm}$ diameter case.

The masks B, C, and D (that are smaller than the detector's sensitive region) were used centered to the detector's sensitive area to use the more homogeneous region of the beam's profile (see Fig. 6.2), avoiding unwanted structures within the holes. We centralized the masks with the help of a printed pattern glued to the aluminum cover of the detector frame, shown in Fig. 6.26. Given the size of these masks (B, C and D), we added an

extra cadmium mask, with a 3 cm side square hole, shown in Fig. 6.27, to avoid detecting neutrons in the regions originally not covered with cadmium.

We used two runs for mask A acquired on distinct days to check if there was any difference between the results. As expected, they turned out compatible. Six runs were necessary to obtain data from all the regions of mask E, which did not present discrepancies between them.

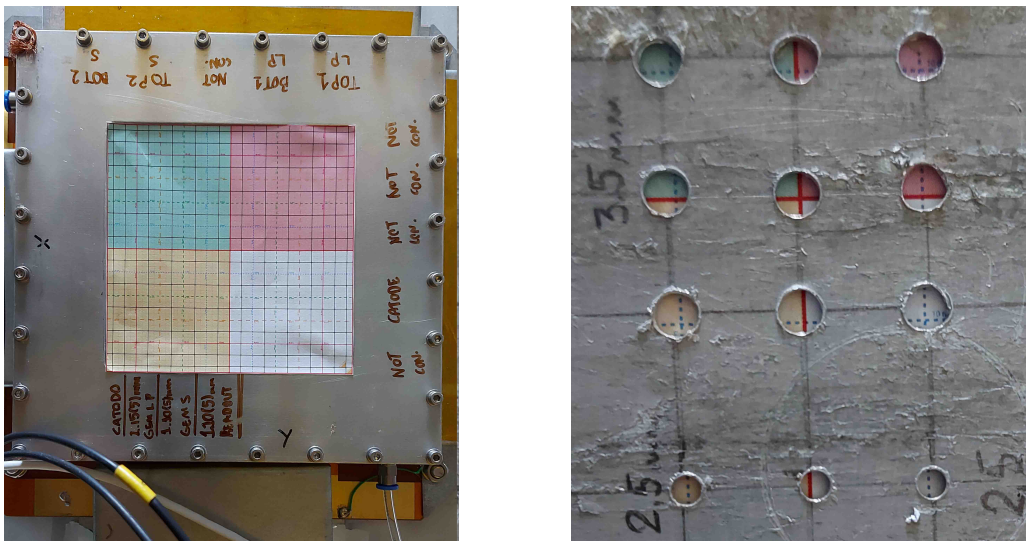

(a) (b)

Figure 6.26: The printed pattern glued on the alumin lid of the detector frame (a) and its use to visually centralize the cadmium masks (b).

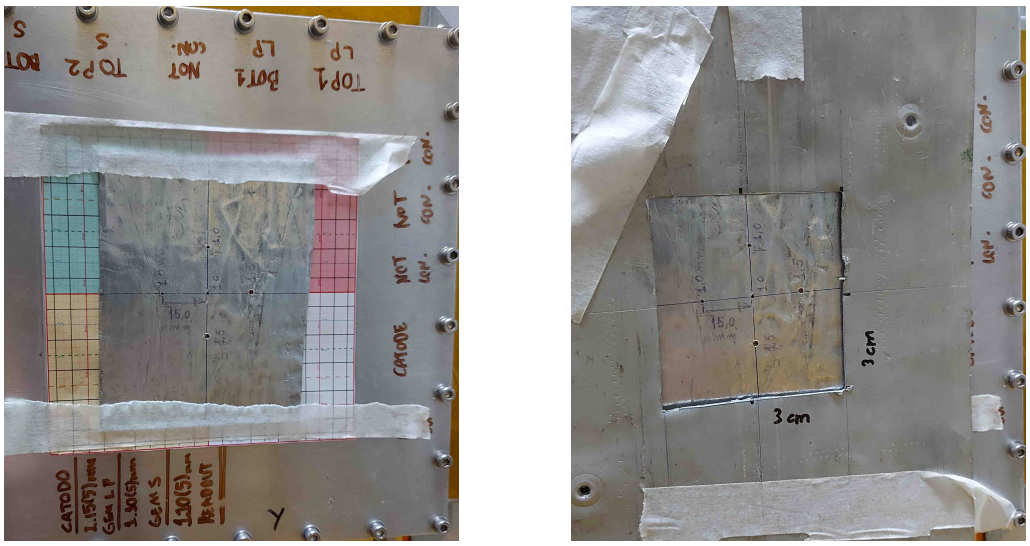

(a) (b)

Figure 6.27: Mask C without the extra mask (a) and with the extra mask (b) to remove unwanted events.

As we notice in the dependence fit for each direction, presented in Figs. 6.28 and 6.29, these data sets agree reasonable with what was expected, corroborating the previous results shown using the more robust edge method.

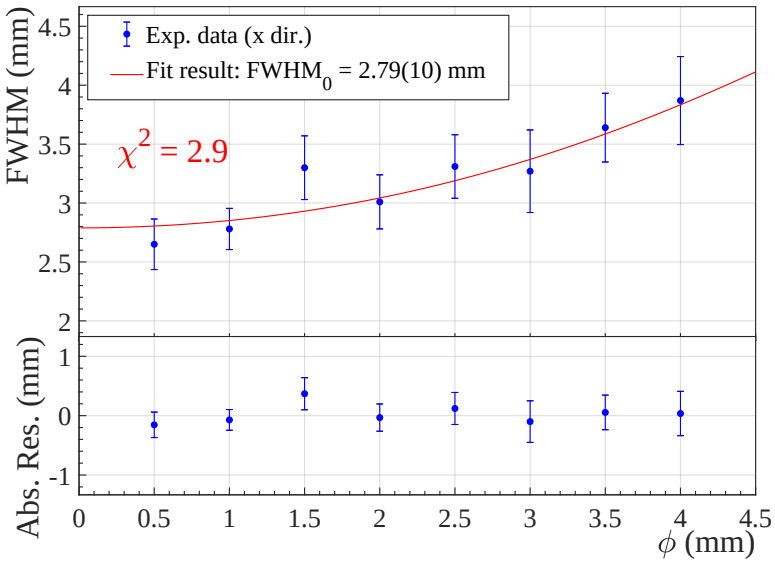

Figure 6.28: Fit of $P_{real}(x)$ function for holes with different diameter. The fitted parameter is the σ of the equivalent gaussian PSF function of the detector, which results in the FWHM_0 shown in the plot. We also present the χ^2 for the fit and the absolute residuals plot.

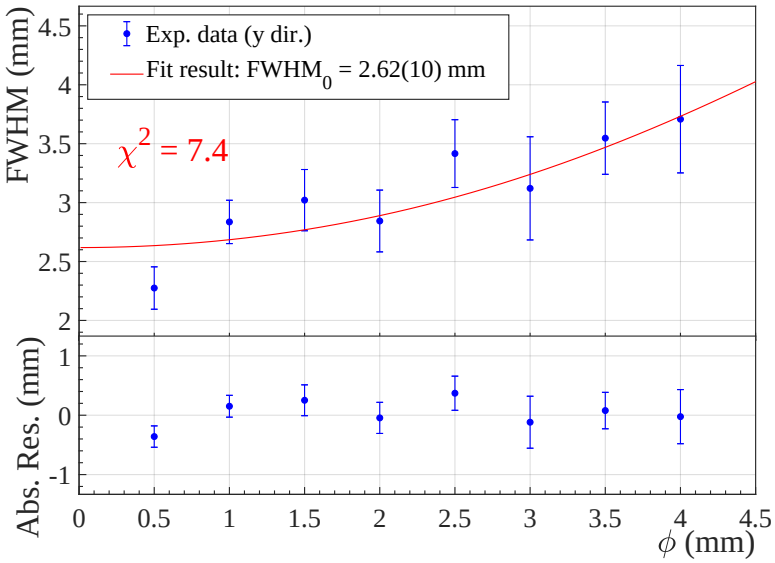

Figure 6.29: Fit of $P_{real}(y)$ function for holes with different diameter. The fitted parameter is the σ of the equivalent gaussian PSF function of the detector, which results in the FWHM_0 shown in the plot. We also present the χ^2 for the fit and the absolute residuals plot.

To verify the regularity of the detector regarding the spatial position, we fixed the adequately machined mask E shown in Fig 4.18 at the top of the detector. We scanned its holes with the neutron beam by changing the X-Y-Z table settings. As the machining precision is typically $0.1\,\mathrm{mm}$, unperceivable to our detector, the holes can be considered mutually equivalents. However, the comparison between equivalent holes at different detector regions has to use the same neutron flux and same beam profile within the hole area. This means one has to illuminate the holes under comparison with the same coordinate in the beam referential.

Starting from the neutron image with the mask at the original position of the detector, we defined the neutron beam coordinate system, shown in Fig. 6.30. The $2\,\mathrm{mm}$ diameter holes were labeled with numbers while the $1\,\mathrm{mm}$ diameter holes were labeled with letters. Each hole of the mask E (in Fig. 4.18) is illuminated by certain point of the neutron beam, as shown in Fig. 6.31.

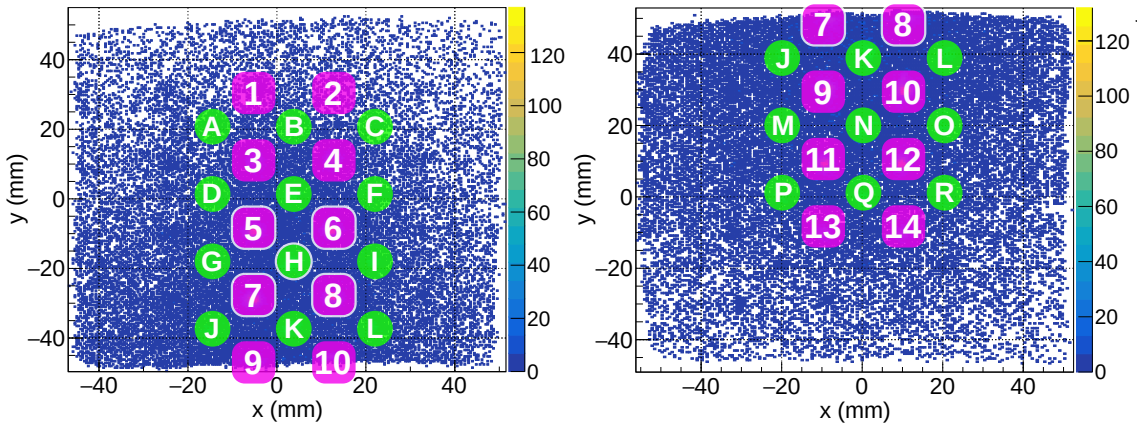

(a) (b)

Figure 6.30: Map of the coordinates in the neutron beam referential. The detector's displacements are multiples of $20\,\mathrm{mm}$. Therefore, a given coordinate in the neutron beam referential is seen to walk from hole to hole.

Moving the detector with respect to the beam in X or Y directions[4] by constant increments of $20\,\mathrm{mm}$ is equivalent to project the coordinates shown in Fig 6.30 through another set of holes. This can be used to illuminate several holes using a specific coordinate (in the beam reference frame), mapping the readout. As we show earlier, the projection of the neutron image of these holes is related to the spatial resolution. This method allows us to map spatial resolution of several spots of the detector-sensitive area quickly, at low counting rates.

[4]the same directions of the readout plane.

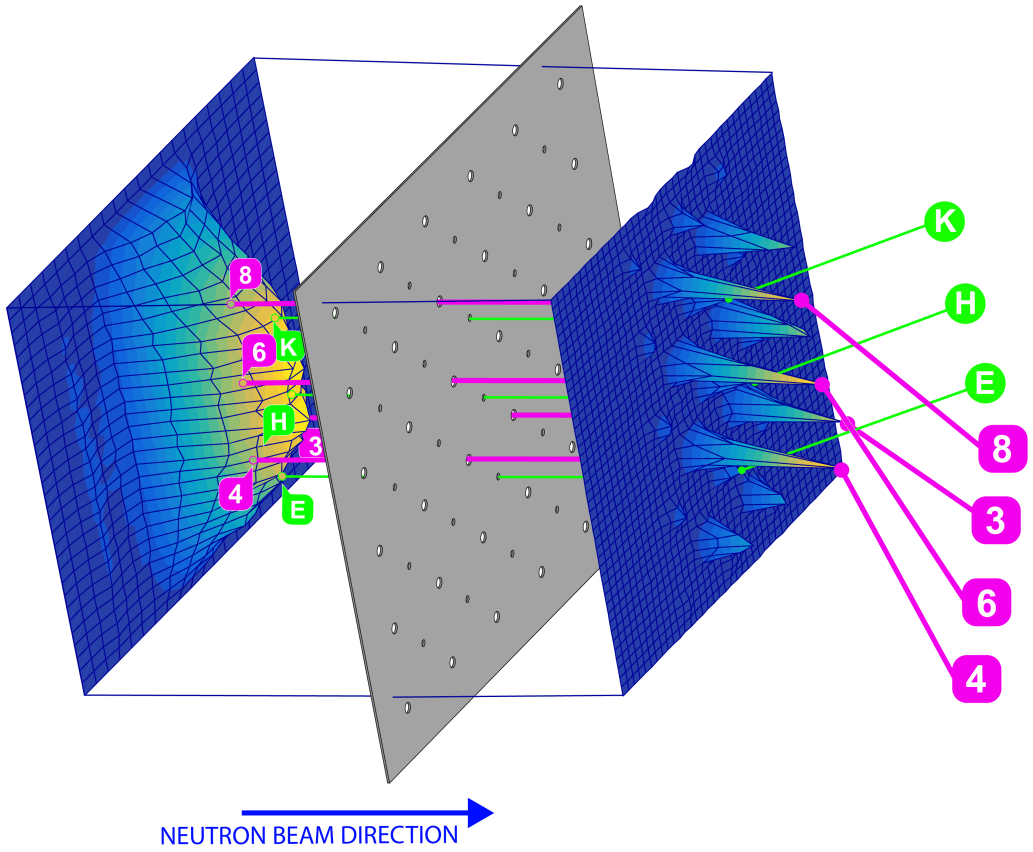

Figure 6.31: Neutron beam profile before and after the cadmium mask indicating some coordinates in the beam reference frame. The images are depicted in surface mode with a large mesh size to enhance visualization (even though the circular projections look spiky).

By mapping the FWHM in X and Y directions, as shown in Figs. 6.32 and 6.33 for different holes, we see a good agreement for different spots, which indicates that the detector's sensitive area is fairly homogen regarding the spatial resolution. For each set of measurements of a given diameter, the uncertainties were estimated as the standard deviation since the fit's uncertainty does not reflect the global behavior of the spatial resolution, underestimating the uncertainty. This result is summarized in Fig. 6.34. The FWHM is obtained using the same technique described earlier, from 9 runs of $10\,\mathrm{min}$ each, starting with the detector in the state shown in Fig. 6.30a, and moving in millimeters: (+20,0), (+20,0), (0,+40), (-20,0), (-20,0) to reach the state shown in Fig. 6.30b, (-20,0), (-20,0), (0,-40), (+20,0), and a final (+20,0), which brought it back to the state of 6.30a, whose results were equivalent to the ones obtained in the first run.

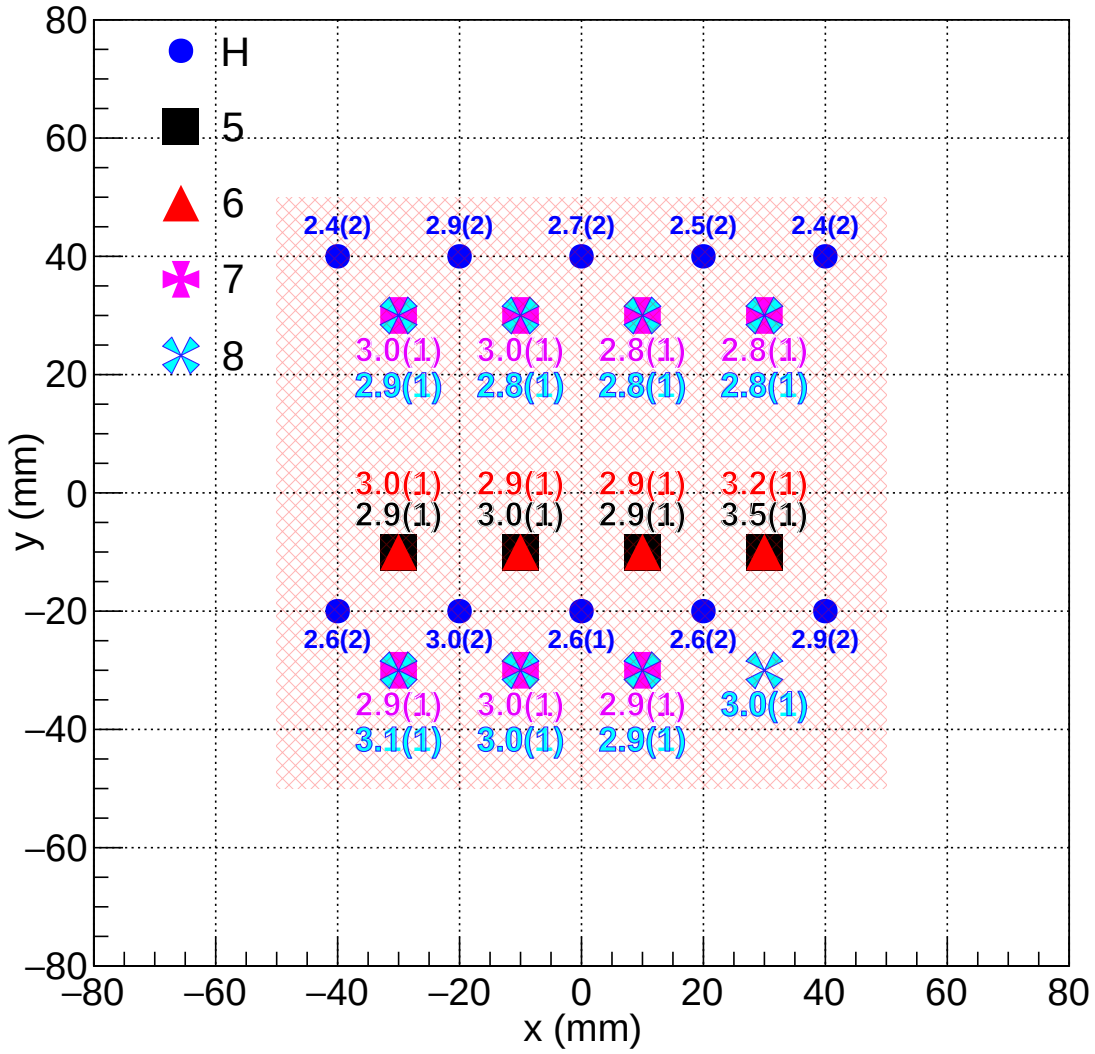

Figure 6.32: FWHM values for the holes projection obtained for different spots to 10 min runs, for the X direction, over the readout plane. Several values were measured twice. Markers identify the "beam position" following Fig. 6.30. The readout area is depicted as the red hatched area.

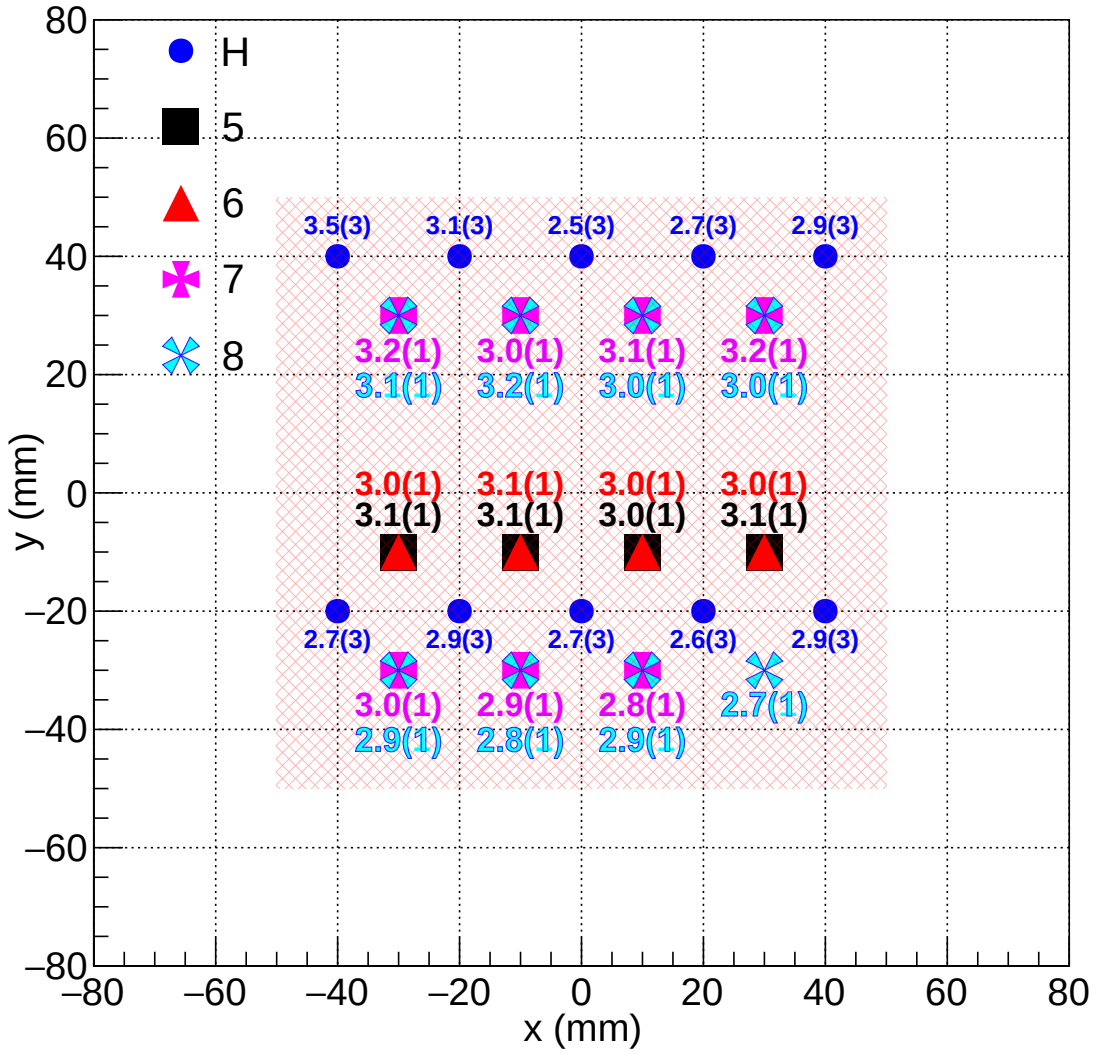

Figure 6.33: FWHM values for the holes projection obtained for different spots to 10 min runs, for the Y direction, over the readout plane. Several values were measured twice. Markers identify the "beam position" following Fig. 6.30. The readout area is depicted as the red hatched area.

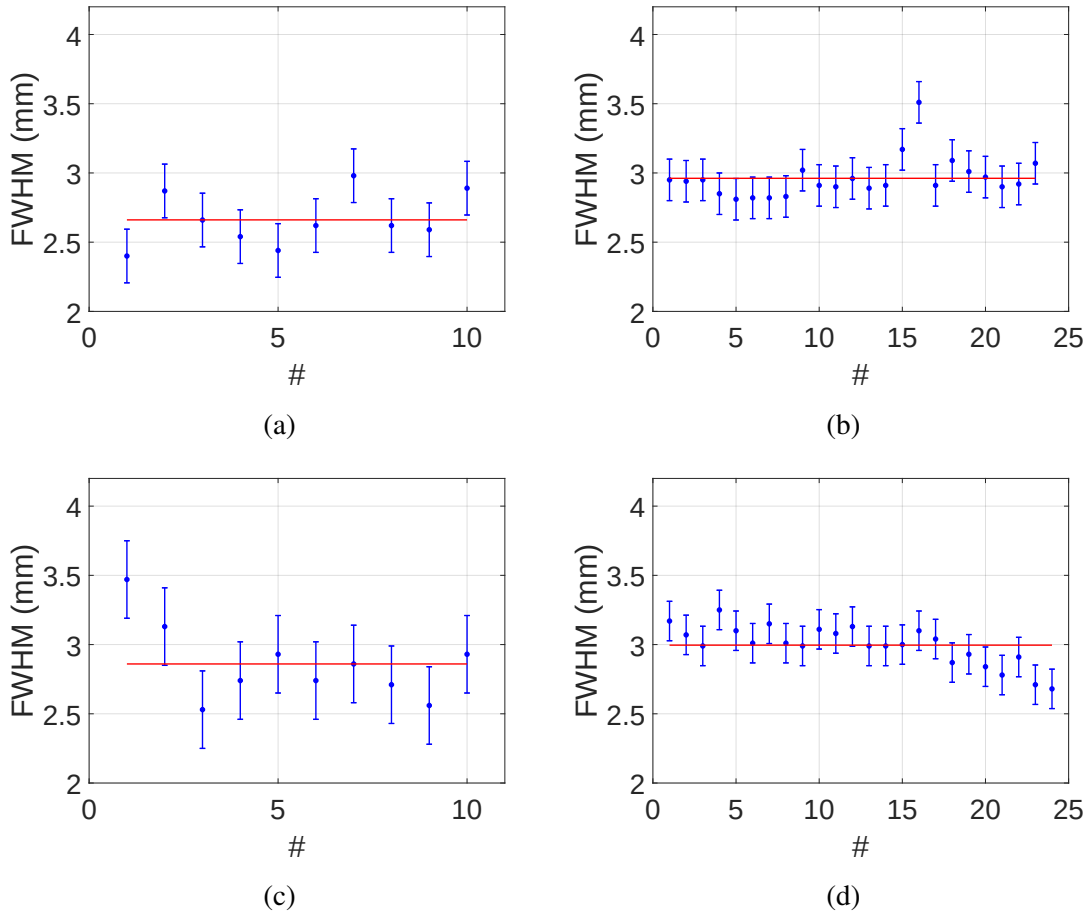

Figure 6.34: The distribution of the FWHM for the 1 mm holes (a) and 2 mm holes (b) in the X direction, and 1 mm holes (c) and 2 mm holes (d) in the Y direction shown in Figs. 6.32 and 6.33.

As mentioned, there is a good agreement between the points. We considered the standard deviation of the FWHMs obtained for each diameter (1 mm or 2 mm) as the uncertainty for this analysis. The uncertainties provided by the fit were too small and did not represent the variations expected in this experiment. Also, it is a fair assumption since there is no reason to believe that there are significant differences between different spots of the readout plane. In other words, there are no outliers points that would indicate deformations in any region.

From the results presented in this section, it is reasonable to state that our detector shown a spatial resolution of at least 3 mm, that was measured by the two methods presented. This spatial resolution holds throughout the central area of the readout, as expected.

6.5 Detection efficiency

The detector efficiency is the quantity that represents the fraction of detected neutrons out of the total number of neutrons that entered the sensitive area of the detector. Mathematically, one can write:

$$\varepsilon = \frac{N_{det}}{N_{tot}} = \frac{N_{det}}{\phi A \Delta t}, \tag{6.7}$$

where N_{det} is the number of detected neutrons[5] and N_{tot} the total number of neutrons that entered the detector. Note that is possible to express N_{tot} as the product of ϕ, the neutron beam flux, A, the area of the beam and the irradiation time Δt.

Since the beam we used to test the prototype was not developed for this application, it is necessary to know the actual flux of the beam. As discussed in sec. 4, the neutron beam monitor was calibrated with respect to the central region only, which means that one must use this region to perform any measurements regarding the detector's efficiency.

For assuring to select this central area, the efficiency measurements were done using the squared cadmium masks shown in Fig. 6.35b, with $6\,\mathrm{mm}$ and $12\,\mathrm{mm}$ side. We assembled them so the central hole coincides with the centre of the neutron beam outlet.

(a) (b)

Figure 6.35: Detail of the slit holder fixed at the neutron beam outlet (a) and the cadmium masks made from slits masks used for the neutron efficiency evaluation (b), the left one has a $6\,\mathrm{mm}\times 6\,\mathrm{mm}$ area, and the right one has a $12\,\mathrm{mm}\times 12\,\mathrm{mm}$ area. When put in the beam outlet, the squared area was located in the spot where the neutron beam flux was measured.

The resulting runs are shown in Fig 6.36, where it is possible to notice the Y direction

[5] measured by the NIM counter.

exacerbated length of the originally squared shapes. This happens due to the composition of two main effects: the first, briefly discussed in sec. 6.1, is that the detector is far from the mask, which results in a magnification of the divergence effect of the neutron beam. The second is concerning the composition of the beam: the monochromator is composed of cristal slabs (see Fig. 5.23) which diffracts the correct wavelength individually resulting in a non-trivial superposition of the 9 monochromatic beams.

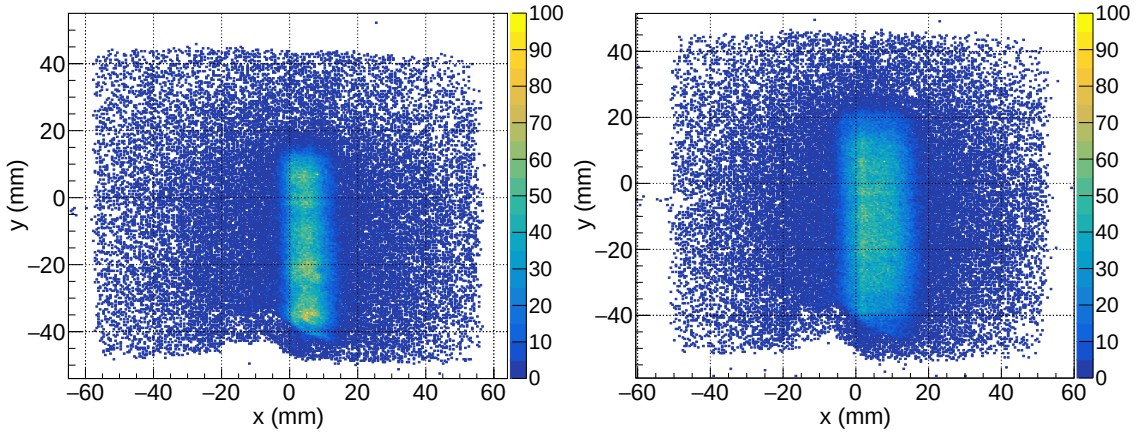

(a) (b)

Figure 6.36: Runs for measuring the efficiency using the $6\,\mathrm{mm} \times 6\,\mathrm{mm}$ square mask (a) and the $12\,\mathrm{mm} \times 12\,\mathrm{mm}$ square mask (b). The acquisition time for both runs is $5\,\mathrm{min}$.

The shape distortion is not a problem in the efficiency measurement since the selected part of the beam is totally inside the sensitive area of the detector. We could avoid distortion by reducing the detector distance from the beam outlet, which is not worth it since the difference would be aesthetic; moreover, the process for moving the whole set of the detector with the precision table could damage connections and electrical contacts. These connections will be more secure in further versions of this detector, with properly engineered pieces. As a prototype, we aim for the versatility of easy connection, inspection, and replacement of the assembled parts of the set.

In order to use Eq. 6.7 for computing the detection efficiency, it is necessary to correct the neutron flux using the following relation:

$$\phi = \phi_c \frac{f}{f_c} \tag{6.8}$$

where $\phi_c = 6.22(19) \times 10^4\,\mathrm{n\,cm^{-2}s^{-1}}$ was the neutron flux obtained (see sec. 5.4), f is the frequency of the beam monitor for the current run and $f_c = 767(3)\,\mathrm{Hz}$ is the frequency for the calibration run. This is a crucial procedure to account for any variations in the flux caused by the reactor's operation. Its uncertainty is given by standard error propagation, as it follows:

$$\sigma_\phi = \sqrt{\left(\frac{f}{f_c}\sigma_{\phi_c}\right)^2 + \left(\frac{\sigma_{\phi_c} f}{f_c^2}\sigma_{f_c}\right)^2 + \left(\frac{\sigma_{\phi_c}}{f_c}\sigma_f\right)^2}. \tag{6.9}$$

The uncertainty for N_{tot} is propagated using the same reasoning, which results in

$$\sigma_{N_{tot}} = \sqrt{\left(\Delta t A \sigma_\phi\right)^2 + \left(\phi A \sigma_{\Delta_t}\right)^2 + \left(\sigma_\phi \Delta t \sigma_A\right)^2}, \tag{6.10}$$

where $\sigma_{\Delta_t} = 5\,\mathrm{s}$ (since the start/stop of the NIM counter is manually activated), σ_ϕ is given by Eq. 6.9 and σ_A is given by the mask calibration (see Eq. 4.14). The calculation of the final uncertainty considers $\sigma_{N_{det}} = \sqrt{N_{det}}$ and the Eq. 6.10, resulting in

$$\sigma_\varepsilon = \sqrt{\left(\frac{1}{N_{tot}}\sigma_{N_{det}}\right)^2 + \left(\frac{N_{det}}{N_{tot}^2}\sigma_{N_{tot}}\right)^2}. \tag{6.11}$$

The resulting efficiency for the $6\,\mathrm{mm}$ side mask was $2.75(26)\,\%$ and for the $12\,\mathrm{mm}$ side mask was $2.57(15)\,\%$, as shown in Table 6.2. It is interesting to note that the $6\,\mathrm{mm}$ side square area fits inside the $12\,\mathrm{mm}$ diameter area in which the neutron flux was measured, since the diagonal of the l side square equals $l\sqrt{2}$, that corresponds to the diameter of the circle that contains it. Even though the area of the 12 mm side square mask is not entirely contained within the calibrated region, the inhomogeneity of the beam is not pronounced enough to cause incompatible results.

Table 6.2: Data used to evaluate the detection efficiency for the $6\,\mathrm{mm}$ side (S) and $12\,\mathrm{mm}$ side (L) cadmium masks. The units for flux and its uncertainty are $\mathrm{n\,cm^{-2}s^{-1}}$ and N_{mon} stands for the counts obtained in the neutron monitor.

mask	N_{det}	$\sigma_{N_{det}}$	Δt (s)	N_{mon}	f (Hz)	σ_f (Hz)	A (mm^2)
S	191108	437	300	244780	816	14	35
L	749362	866	300	243892	813	14	148

mask	σ_A (mm^2)	ϕ	σ_ϕ	N_{tot}	$\sigma_{N_{tot}}$	ε (%)	σ_ε (%)
S	3	66.2E+03	2.3E+03	69.4E+05	6.5E+05	2.75	0.26
L	6	65.9E+03	2.3E+03	292E+05	17E+05	2.57	0.15

Regarding the complex geometrical composition of the beam; this hypothesis is corroborated by observing the X and Y projections of Fig. 6.36a, shown in Fig. 6.37. The red arrows in Fig. 6.37b points to periodic structures in the neutron beam that are not observable in the X projection. The 6 mm square hole acts like a pinhole when compared with the dimensions of the monochromator cristals, besides that we also know there is an intentional focusing effect obtained by bending the silicon slabs.

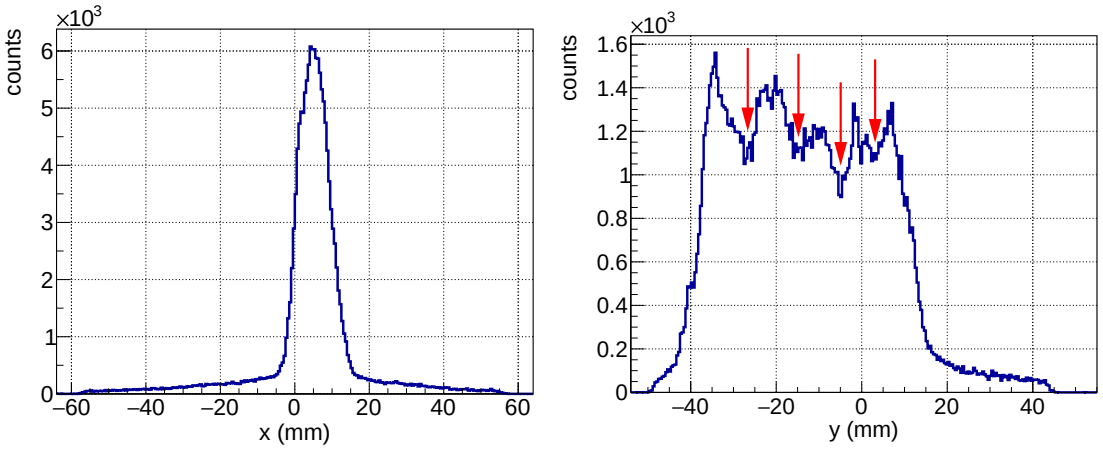

(a) (b)

Figure 6.37: X profile (a) and Y profile (b) of the Fig. 6.36a with possible structures signaled by red arrows.

We performed the actual pinhole experiment, measuring the neutron image for some hours of a cadmium mask where a tiny hole ($\phi \sim 0.3\,\mathrm{mm}$) was made in its center by a nail. This mask was positioned at the neutron beam outlet slit holder. The image is presented in Fig. 6.38 and the projections in Fig. 6.39. As expected, is possible to see some structures in Y directio=n.

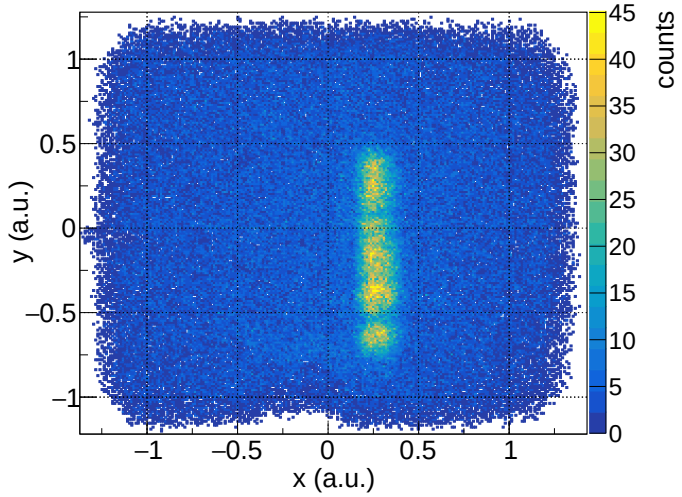

Figure 6.38: Neutron image produced in the detector by placing a pinhole at the beam outlet. The differences in intensity indicate complex structures of the neutron beam. The acquisition time was $1\,\mathrm{h}\ 47\,\mathrm{min}$ because of the $\sim 30\,\mathrm{Hz}$ rate.

As the structures are not simple, select periodic points is a challenge. However, they are very apparent, and some of their factors are modified by customizing the selected area of the beam. Further studies can be performed in order to understand how it can affect the image, but it is out of the scope of our work that focuses on the detector itself.

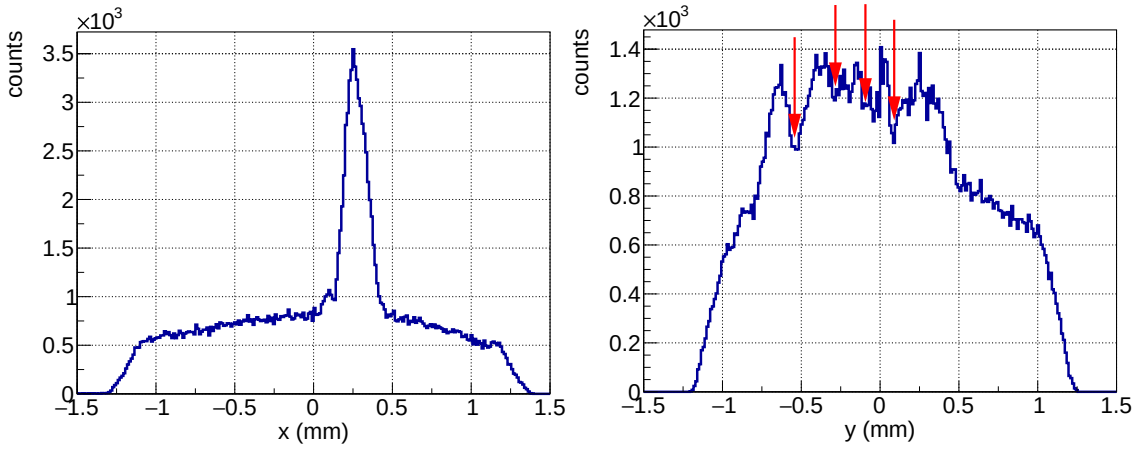

(a) (b)

Figure 6.39: X profile (a) and Y profile (b) of the Fig. 6.38 with possible structures signaled by red arrows.

It is also interesting to verify if the detector behaves as expected regarding the efficiency in different regions. From what we presented, the obtained efficiency is the mean efficiency over a particular deposition area. We applied the same mapping process used for the resolution (sec. 6.4) for this analysis and used the same runs.

Measuring runs using the same duration, $10\,\mathrm{min}$, it is expected that the holes illuminated by the same coordinate in the neutron beam referential at different spots of the sensitive area present a compatible number of counts. Nevertheless, it is necessary to normalize the counts with the neutron monitor (fission chamber shown in Figure 5.22).

We analyzed the counts over a small region that contains the beam position labelled as “H” in Fig. 6.30 for several detector spots and corrected these counts proportionally to the neutron flux. This procedure helps in checking the homogeneity of response regarding efficiency. Fig. 6.40a shows the region around the“H” hole. These spots are the same as the blue markers in Fig. 6.32 and depicted as the red dots in the Fig. 6.40a.

The counts are corrected to the average neutron flux so that they can be compared, as shown in Fig. 6.40b. This correction consists of multiplying the counts in the hole by a factor. For each run, this factor is calculated as the number of counts measured by the neutron monitor for that run, divided by the average number of counts measured by the neutron monitor for all runs considered for this procedure. The uncertainty was considered equal to the standard deviation for the whole set of counts to all spots.

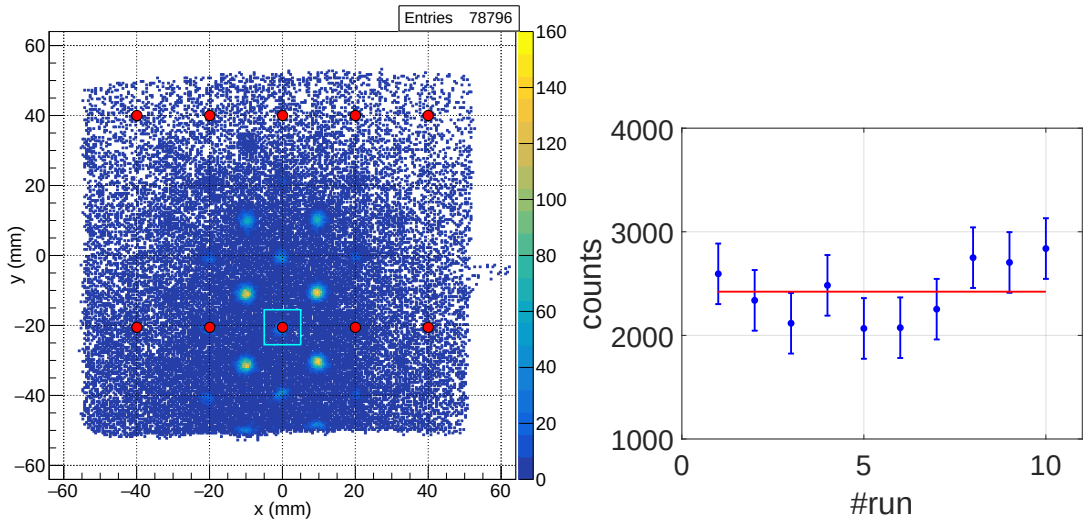

(a) (b)

Figure 6.40: Region selected around the "H" hole to count the entries (a) and the comparison results (b) for the spots identified by blue dots in Fig. 6.32, for $10\,\mathrm{min}$ runs.

The results indicate that the detector responds homogeneously. The average (red line) presented in Fig. 6.40b is $2421(92)$ counts. Differences in the efficiency would appear as significant differences in the number of counts since the neutron beam coordinate that illuminates these points are the same. We expect two critical factors to cause sensitive differences: the inhomogeneity in the $^{10}B_4C$ deposition and defects in the readout+resistive chain set. The gain of the GEM foil was considered constant given its low voltage operation and the results obtained by Geovane Grossi, who presented a careful study of the GEM detectors used at our laboratory [79].

From the results obtained for the detection efficiency, it is possible to state that our detector presented about $2.66(30)\,\%$ detection efficiency (average of the two values shown in Table 6.2 that are compatible with each other). No sensitive irregularity was measured, which means it is reasonable to expect homogeneity regarding efficiency, at least in the central area mapped.

Chapter 7

Final Considerations

This work presented the feasibility of detecting thermal neutrons using MPGDs with a single $^{10}B_4C$ layer with position sensitivity obtained using a 256×256 strip plane read via resistive chains.

Several aspects were taken into account during the construction of this prototype. When compared with gamma rays, the products of the ^{10}B (n,α)^{7}Li reaction produce a reasonable amount of ionization. As is still necessary to multiply these charges, dividing the multiplication stages between the two GEMs contributes to the stable operation of the detector, strongly minimizing the discharge probability. The choice for using a large pitch GEM on top was also crucial for this aspect. Using $10\,\%$ quenching gas also enhances the gain for low voltages.

Another essential feature of the prototype is the non-sensibility to gamma-ray background. It was possible by choosing a proper drift zone size based on the preliminary simulations. These simulations presented significant results to understand how the detector's geometry affects its operation, allowing to obtain an initial spectrum that resulted compatible with the Geant4 simulation and the experimental measurements. The advantage of using these simulations is that they demand a shorter computational time than the most elaborated ones. Therefore, the result of any further geometric modification in the boron carbide deposition or the drift zone of the detector can be quickly simulated, providing versatility to operate the prototype.

The operation at relatively low voltages also contributes to the versatility of the detector. In our case, the detector operates as $1400\,\mathrm{V}$, lower than standard triple GEM assemblies used for several applications [82] or even the ALICE's 4-GEM TPC detector [63] that needs a couple of thousands of volts. The prototype also provides neutron images using only five electronic channels. It is possible to adapt this to only four electronic channels if required, but in this case, some changes in the electronic are necessary to the trigger system.

We succeeded in characterizing some detector's essential parameters, such as the spatial resolution and detection efficiency. The spatial resolution was measured using two different methods that utilized edges and holes, respectively. The edge method allows mapping the sensitive area of the prototype efficiently since the resolution measurement can be obtained from fitting regions from neutron images of masks with sharp edges since there are enough counts in those regions. The mapping indicated that our prototype has a homogeneous spatial resolution over the mapped area. The second method uses neutron images produced with masks with holes of several diameters. Both methods were compatible and resulted in a spatial resolution equal to at least $3\,\mathrm{mm}$.

The detection efficiency was obtained by two runs, selecting specific areas of the neutron beam centered at the spot where the neutron flux was measured. The flux was correlated with a beam monitor allowing us to correct it for possible variations over time. Despite using slightly different areas, the measurements were compatible within the neutron beam's quasi-homogeneous region, and our thermal neutron detection efficiency was $2.66(30)\,\%$.

It was possible to map the counts over most parts of the sensitive area of our detector using the same neutron beam coordinate (i.e., same illumination). There were no signs of inhomogeneity regarding the efficiency, which means our prototype proved to be trustworthy also regarding detection efficiency. These results also give us information about the excellent quality of the boron carbide deposition, sputtered by the European Spallation Source.

Further applications

There are several applications for this work. The construction of this prototype detector provided us with the know-how for production (jointly with ESS), assembly, and operation of these kinds of detectors. One can explore the versatility of the prototype in different ways. One example is the production of more portable devices with various areas since the sensitive gaseous volume of the detector presents a small thickness (smaller than $1\,\mathrm{cm}$). Applications that demand better resolution could also be fulfilled using an enhanced electronic acquisition such as the SRS [104].

The GEMs can also be switched to thick-GEMs [27], which are thicker versions of the GEMs made out of PCB, using the national industry, which provides viability of quick production and lower costs.

The detector can be explored in applications that demand different detection efficiency. A thinner deposition will reduce the efficiency, which is interesting for beam monitors. The rise of the detection efficiency is feasible by using several deposition lay-

ers, as in the CASCADE detector [66]. One variation of this idea is using thick-GEMs for this application.

As the GEMs can be produced in curved geometries [105], it is also possible to make long arc detectors covering big angles ($\sim 180°$) for neutron diffraction experiments. Its low sensitivity to gamma rays and fair spatial resolution are promising for this application.

Given the detector's stability, efficiency[1], and the possibility of monitoring, it can also be used as area neutron monitors applications for research facilities.

Finally, it is possible to adapt it to work in time projection chamber (TPC) mode, using a bigger drift zone. For this case, one has to waive the gamma low-sensitive requirement since the large volume of gas will be sensitive to gammas. However, it allows obtaining a resolution of the magnitude of fractions of millimeters [106].

[1]The efficiency of the detector change for gains change, since the energy spectrum is drifted regarding the threshold.

Bibliography

[1] Nobel Prize Outreach AB 2021. *The structure and dynamics of matter revealed*. Last visited on 25/11/2021. URL: https://www.nobelprize.org/prizes/physics/1994/press-release/.

[2] James Chadwick. "The existence of a neutron". In: *Proceedings of the Royal Society of London. Series A, Containing Papers of a Mathematical and Physical Character* 136.830 (1932), pp. 692–708. DOI: 10.1098/rspa.1932.0112. eprint: https://royalsocietypublishing.org/doi/pdf/10.1098/rspa.1932.0112. URL: https://royalsocietypublishing.org/doi/abs/10.1098/rspa.1932.0112.

[3] K. Prokeš and F. Yokaichiya. "Chapter 2 - Elastic Neutron Diffraction on Magnetic Materials". In: ed. by Ekkes Brück. Vol. 25. Handbook of Magnetic Materials. Elsevier, 2016, pp. 67–143. DOI: https://doi.org/10.1016/bs.hmm.2016.09.001. URL: https://www.sciencedirect.com/science/article/pii/S1567271916300026.

[4] Antony Joseph. "Chapter 13 - Neutron spectroscopy techniques". In: *Micro and Nanostructured Composite Materials for Neutron Shielding Applications*. Ed. by Sajith Thottathil Abdulrahman, Sabu Thomas, and Zakiah Ahmad. Woodhead Publishing Series in Composites Science and Engineering. Woodhead Publishing, 2020, pp. 355–378. ISBN: 978-0-12-819459-1. DOI: https://doi.org/10.1016/B978-0-12-819459-1.00013-1. URL: https://www.sciencedirect.com/science/article/pii/B9780128194591000131.

[5] J. W. White and C. G. Windsor. "Neutron-scattering - modern techniques and their scientific impact". In: *Reports On Progress In Physics* 47.6 (1984), 707–765. ISSN: 0034-4885. DOI: {10.1088/0034-4885/47/6/003}.

[6] G. E. Bacon and K. Lonsdale. "Neutron Diffraction". In: *Reports On Progress In Physics* 16 (1953), 1–61. ISSN: 0034-4885. DOI: {10.1088/0034-4885/16/1/301}.

[7] Frank Gabel. "Chapter Thirteen - Small-Angle Neutron Scattering for Structural Biology of Protein–RNA Complexes". In: *Structures of Large RNA Molecules and Their Complexes*. Ed. by Sarah A. Woodson and Frédéric H.T. Allain. Vol. 558. Methods in Enzymology. Academic Press, 2015, pp. 391–415. DOI: https://doi.org/10.1016/bs.mie.2015.02.003. URL: https://www.sciencedirect.com/science/article/pii/S0076687915000786.

[8] M.A. Fedorin and B.G. Titov. “Method of radial sounding and elemental analysis of formations during well logging using neutron inelastic scattering gamma time-of-flight spectrometry”. In: *Russian Geology and Geophysics* 51.12 (2010), pp. 1295–1303. ISSN: 1068-7971. DOI: https://doi.org/10.1016/j.rgg.2010.11.009. URL: https://www.sciencedirect.com/science/article/pii/S1068797110002075.

[9] R. T. Kouzes. *The ^{3}He Supply Problem*. Tech. rep. PNNL-18388. Prepared for the U.S. Department of Energy under contract DE-AC05-76RL01830. P.O. Box 62, Oak Ridge, TN 37831-0062: U. S. Department of Energy, Apr. 2009. URL: https://www.pnnl.gov/main/publications/external/technical_reports/PNNL-18388.pdf.

[10] Richard T. Kouzes et al. “Passive neutron detection for interdiction of nuclear material at borders”. In: *Nuclear Instruments and Methods in Physics Research Section A: Accelerators, Spectrometers, Detectors and Associated Equipment* 584.2 (2008), pp. 383–400. ISSN: 0168-9002. DOI: https://doi.org/10.1016/j.nima.2007.10.026. URL: https://www.sciencedirect.com/science/article/pii/S0168900207022085.

[11] Paolo Peerani et al. “Testing on novel neutron detectors as alternative to ^{3}He for security applications”. In: *Nucl. Instr. Meth. A* 696.0 (2012), pp. 110–120. ISSN: 0168-9002. DOI: http://dx.doi.org/10.1016/j.nima.2012.07.025. URL: http://www.sciencedirect.com/science/article/pii/S0168900212007929.

[12] Kyriakos Tsorbatzoglou and Robert D. McKeag. “Novel and efficient ^{10}B lined tubelet detector as a replacement for ^{3}He neutron proportional counters”. In: *Nucl. Instr. Meth. A* 652.1 (2011), pp. 381–383. ISSN: 0168-9002. DOI: http://dx.doi.org/10.1016/j.nima.2010.08.102. URL: http://www.sciencedirect.com/science/article/pii/S0168900210018899.

[13] A. Pietropaolo et al. “A new ^{3}He-free thermal neutrons detector concept based on the GEM technology”. In: *Nucl. Instr. Meth. A* 729.0 (2013), pp. 117–126. ISSN: 0168-9002. DOI: http://dx.doi.org/10.1016/j.nima.2013.06.058. URL: http://www.sciencedirect.com/science/article/pii/S0168900213008917.

[14] X. Ledoux et al. “First beams at neutrons for science”. In: *The European Physical Journal A* 57.8 (Aug. 2021), p. 257. ISSN: 1434-601X. DOI: 10.1140/epja/s10050-021-00565-x. URL: https://doi.org/10.1140/epja/s10050-021-00565-x.

[15] A.P. Serebrov et al. “Ultracold-neutron infrastructure for the PNPI/ILL neutron EDM experiment”. In: *Nuclear Instruments and Methods in Physics Research Section A: Accelerators, Spectrometers, Detectors and Associated Equipment* 611.2 (2009). Particle Physics with Slow Neutrons, pp. 263–266. ISSN: 0168-9002. DOI: https://doi.org/10.1016/j.nima.2009.07.084. URL: https://www.sciencedirect.com/science/article/pii/S016890020901540X.

[16] Alessandro Tengattini et al. "NeXT-Grenoble, the Neutron and X-ray tomograph in Grenoble". In: *Nuclear Instruments and Methods in Physics Research Section A: Accelerators, Spectrometers, Detectors and Associated Equipment* 968 (2020), p. 163939. ISSN: 0168-9002. DOI: https://doi.org/10.1016/j.nima.2020.163939. URL: https://www.sciencedirect.com/science/article/pii/S0168900220304198.

[17] A. Pietropaolo et al. "Neutron detection techniques from μeV to GeV". In: *Physics Reports* 875 (2020). Neutron detection techniques from μeV to GeV, pp. 1–65. ISSN: 0370-1573. DOI: https://doi.org/10.1016/j.physrep.2020.06.003. URL: https://www.sciencedirect.com/science/article/pii/S0370157320302490.

[18] F. Sordo et al. "Neutronic design for ESS-Bilbao neutron source". In: *Nuclear Instruments and Methods in Physics Research Section A: Accelerators, Spectrometers, Detectors and Associated Equipment* 707 (2013), pp. 1–8. ISSN: 0168-9002. DOI: https://doi.org/10.1016/j.nima.2012.12.092. URL: https://www.sciencedirect.com/science/article/pii/S0168900212016488.

[19] Giorgia Albani et al. "High-rate measurements of the novel BAND-GEM technology for thermal neutron detection at spallation sources". In: *Nuclear Instruments and Methods in Physics Research Section A: Accelerators, Spectrometers, Detectors and Associated Equipment* 957 (2020), p. 163389. ISSN: 0168-9002. DOI: https://doi.org/10.1016/j.nima.2020.163389. URL: https://www.sciencedirect.com/science/article/pii/S0168900220300036.

[20] L.M.S. Margato et al. "Towards high-rate RPC-based thermal neutron detectors using low-resistivity electrodes". In: *Journal of Instrumentation* 16.07 (July 2021), P07009. DOI: 10.1088/1748-0221/16/07/p07009. URL: https://doi.org/10.1088/1748-0221/16/07/p07009.

[21] A. Muraro et al. "MBGEM: a stack of borated GEM detector for high efficiency thermal neutron detection". In: *The European Physical Journal Plus* 136.7 (July 2021), p. 742. ISSN: 2190-5444. DOI: 10.1140/epjp/s13360-021-01707-2. URL: https://doi.org/10.1140/epjp/s13360-021-01707-2.

[22] D. Pfeiffer et al. "First measurements with new high-resolution gadolinium-GEM neutron detectors". In: *Journal of Instrumentation* 11.05 (May 2016), P05011–P05011. DOI: 10.1088/1748-0221/11/05/p05011. URL: https://doi.org/10.1088/1748-0221/11/05/p05011.

[23] K. Kanaki et al. "Detector rates for the Small Angle Neutron Scattering instruments at the European Spallation Source". In: *Journal of Instrumentation* 13.07 (July 2018), P07016–P07016. DOI: 10.1088/1748-0221/13/07/p07016. URL: https://doi.org/10.1088/1748-0221/13/07/p07016.

[24] Nobel Prize Outreach AB 2021. *A breakthrough in the technique for exploring the innermost parts of matter*. Last visited on 26/11/2021. URL: https://www.nobelprize.org/prizes/physics/1992/press-release/.

[25] G. Charpak et al. “The use of multiwire proportional counters to select and localize charged particles”. In: *Nuclear Instruments and Methods* 62.3 (1968), pp. 262–268. ISSN: 0029-554X. DOI: https://doi.org/10.1016/0029-554X(68)90371-6. URL: https://www.sciencedirect.com/science/article/pii/0029554X68903716.

[26] F. Sauli. “GEM: A new concept for electron amplification in gas detectors”. In: *Nuclear Instruments and Methods in Physics Research Section A: Accelerators, Spectrometers, Detectors and Associated Equipment* 386.2 (1997), pp. 531–534. ISSN: 0168-9002. DOI: https://doi.org/10.1016/S0168-9002(96)01172-2. URL: https://www.sciencedirect.com/science/article/pii/S0168900296011722.

[27] R. Chechik et al. “Thick GEM-like hole multipliers: properties and possible applications”. In: *Nuclear Instruments and Methods in Physics Research Section A: Accelerators, Spectrometers, Detectors and Associated Equipment* 535.1 (2004). Proceedings of the 10th International Vienna Conference on Instrumentation, pp. 303–308. ISSN: 0168-9002. DOI: https://doi.org/10.1016/j.nima.2004.07.138. URL: https://www.sciencedirect.com/science/article/pii/S0168900204016663.

[28] Y. Giomataris et al. “MICROMEGAS: a high-granularity position-sensitive gaseous detector for high particle-flux environments”. In: *Nuclear Instruments and Methods in Physics Research Section A: Accelerators, Spectrometers, Detectors and Associated Equipment* 376.1 (1996), pp. 29–35. ISSN: 0168-9002. DOI: https://doi.org/10.1016/0168-9002(96)00175-1. URL: https://www.sciencedirect.com/science/article/pii/0168900296001751.

[29] J. F. C. A. Veloso, J. M. F. dos Santos, and C. A. N. Conde. “A proposed new microstructure for gas radiation detectors: The microhole and strip plate”. In: *Review of Scientific Instruments* 71.6 (2000), pp. 2371–2376. DOI: 10.1063/1.1150623. eprint: https://doi.org/10.1063/1.1150623. URL: https://doi.org/10.1063/1.1150623.

[30] M. J. Berger et al. *XCOM: Photon Cross Section Database (version 1.5)*. 2010. URL: http://physics.nist.gov/xcom.

[31] R. Jenkins et al. “Nomenclature, symbols, units and their usage in spectrochemical analysis - VIII. Nomenclature system for X-ray spectroscopy (Recommendations 1991)”. In: *Pure and Applied Chemistry* 63.5 (1991), pp. 735–746. DOI: doi:10.1351/pac199163050735. URL: https://doi.org/10.1351/pac199163050735.

[32] Marie Hansson, Gertrud Berg, and Mats Isaksson. “Chapter 3 - Determination of Iodine In Vivo and In Vitro by X-Ray Fluorescence Analysis: Methodology and Applications”. In: *Comprehensive Handbook of Iodine*. Ed. by Victor R. Preedy, Gerard N. Burrow, and Ronald Watson. San Diego: Academic Press, 2009, pp. 29–37. ISBN: 978-0-12-374135-6. DOI: https://doi.org/10.1016/B978-0-12-374135-6.00003-0. URL: https://www.sciencedirect.com/science/article/pii/B9780123741356000030.

[33] S.N. Ahmed. *Physics and Engineering of Radiation Detection*. Elsevier Science, 2014. ISBN: 9780128016442. URL: https://books.google.com.br/books?id=lyNzAwAAQBAJ.

[34] G.F. Knoll. *Radiation Detection and Measurement*. Wiley, 2010. ISBN: 9780470131480. URL: https://books.google.com.br/books?id=4vTJ7UDel5IC.

[35] James F. Ziegler, M.D. Ziegler, and J.P. Biersack. "SRIM – The stopping and range of ions in matter (2010)". In: *Nuclear Instruments and Methods in Physics Research Section B: Beam Interactions with Materials and Atoms* 268.11 (2010). 19th International Conference on Ion Beam Analysis, pp. 1818–1823. ISSN: 0168-583X. DOI: https://doi.org/10.1016/j.nimb.2010.02.091. URL: https://www.sciencedirect.com/science/article/pii/S0168583X10001862.

[36] Professor E. Rutherford F.R.S. "LXXIX. The scattering of and particles by matter and the structure of the atom". In: *The London, Edinburgh, and Dublin Philosophical Magazine and Journal of Science* 21.125 (1911), pp. 669–688. DOI: 10.1080/14786440508637080. eprint: https://doi.org/10.1080/14786440508637080. URL: https://doi.org/10.1080/14786440508637080.

[37] J.K. Shultis and R.E. Faw. *Fundamentals of Nuclear Science and Engineering*. CRC Press, 2017. ISBN: 9781498769297. URL: https://books.google.com.br/books?id=Kw0DDQEACAAJ.

[38] M.J. Joyce and Elsevier. *Nuclear Engineering: A Conceptual Introduction to Nuclear Power*. Elsevier, 2018. URL: https://books.google.com.br/books?id=8UZVzAEACAAJ.

[39] P. Rinard. "Neutron Interactions with Matter". In: 1997.

[40] J.R. Lamarsh and A.J. Baratta. *Introduction to Nuclear Engineering*. Addison-Wesley series in nuclear science and engineering. Prentice Hall, 2001. ISBN: 9780201824988. URL: https://books.google.com.br/books?id=xSNnQgAACAAJ.

[41] R. Eisberg et al. *Quantum Physics of Atoms, Molecules, Solids, Nuclei, and Particles*. Quantum Physics of Atoms, Molecules, Solids, Nuclei and Particles. Wiley, 1985. ISBN: 9780471873730. URL: https://books.google.com.br/books?id=mv5QAAAAMAAJ.

[42] N.J. Carron. *An Introduction to the Passage of Energetic Particles through Matter*. Taylor & Francis, 2006. ISBN: 9780750309356. URL: https://books.google.co.uk/books?id=qc6GngEACAAJ.

[43] Francesco Piscitelli. "Boron-10 layers, neutron reflectometry and thermal neutron gaseous detectors". PhD thesis. Instit Laue-Langevin and Università degli Studi di Perugia, 2014. URL: https://www.ill.eu/fileadmin/user_upload/ILL/1_About_ILL/List_of_PhD_thesis/Piscitelli_PhDthesis_c.pdf.

[44] A.J. Koning et al. “TENDL: Complete Nuclear Data Library for Innovative Nuclear Science and Technology”. In: *Nuclear Data Sheets* 155 (2019). Special Issue on Nuclear Reaction Data, pp. 1–55. ISSN: 0090-3752. DOI: https://doi.org/10.1016/j.nds.2019.01.002. URL: https://www.sciencedirect.com/science/article/pii/S009037521930002X.

[45] Carina Höglund et al. “B4C thin films for neutron detection”. In: *Journal of Applied Physics* 111.10 (2012), p. 104908. DOI: 10.1063/1.4718573.

[46] Fabio Sauli. “Principles of operation of multiwire proportional and drift chambers”. In: CERN, Geneva, 1975 - 1976. CERN. Geneva: CERN, 1977, 92 p. DOI: 10.5170/CERN-1977-009. URL: https://cds.cern.ch/record/117989.

[47] Fabio Sauli. *Gaseous Radiation Detectors: Fundamentals and Applications*. Cambridge Monographs on Particle Physics, Nuclear Physics and Cosmology. Cambridge University Press, 2014. DOI: 10.1017/CBO9781107337701.

[48] H.W. Ellis et al. “Transport properties of gaseous ions over a wide energy range”. In: *Atomic Data and Nuclear Data Tables* 17.3 (1976), pp. 177–210. ISSN: 0092-640X. DOI: https://doi.org/10.1016/0092-640X(76)90001-2. URL: https://www.sciencedirect.com/science/article/pii/0092640X76900012.

[49] E. W. McDaniel and E. A. Mason. *Mobility and diffusion of ions in gases*. United States: John Wiley and Sons, Inc, 1973. ISBN: 0-471-58387-1. URL: http://inis.iaea.org/search/search.aspx?orig_q=RN:07253746.

[50] Earl W. McDaniel and Edward A. Mason. *The mobility and diffusion of ions in gases [by] Earl W. McDaniel [and] Edward A. Mason*. English. Wiley New York, 1973, xi, 372 p. ISBN: 0471583871.

[51] P Rice-Evans. *Spark, streamer, proportional and drift chambers*. United Kingdom: Richelieu Press, 1974.

[52] Michael F L’Annunziata. “Radionuclide tracers”. In: (1987).

[53] A. Oed. “Position-sensitive detector with microstrip anode for electron multiplication with gases”. In: *Nuclear Instruments and Methods in Physics Research Section A: Accelerators, Spectrometers, Detectors and Associated Equipment* 263.2 (1988), pp. 351–359. ISSN: 0168-9002. DOI: https://doi.org/10.1016/0168-9002(88)90970-9. URL: https://www.sciencedirect.com/science/article/pii/0168900288909709.

[54] Carlos A. Colmenares. “Bakeable ionization chamber for low-level tritium counting”. In: *Nuclear Instruments and Methods* 114.2 (1974), pp. 269–275. ISSN: 0029-554X. DOI: https://doi.org/10.1016/0029-554X(74)90544-8. URL: https://www.sciencedirect.com/science/article/pii/0029554X74905448.

[55] M. Matoba et al. “Three Dimensional Monte Carlo Simulation of the Electron Avalanche Around an Anode Wire of a Proportional Counter”. In: *IEEE Transactions on Nuclear Science* 32.1 (1985), pp. 541–544. DOI: 10.1109/TNS.1985.4336890.

[56] F. Sauli. "Potentials of advanced gas detectors for health physics". In: *Radiation Protection Dosimetry* 61.1-3 (1995), pp. 29–38. ISSN: 0144-8420. URL: http://inis.iaea.org/search/search.aspx?orig_q=RN:28005946.

[57] A. Breskin. "A subnanosecond, low pressure MWPC for heavily ionizing particles". In: *Nuclear Instruments and Methods* 141.3 (1977), pp. 505–509. ISSN: 0029-554X. DOI: https://doi.org/10.1016/0029-554X(77)90644-9. URL: https://www.sciencedirect.com/science/article/pii/0029554X77906449.

[58] Toru Tanimori et al. "Development of a MicroStrip Gas Chamber as a Time-Resolved Area Detector". In: *Journal of synchrotron radiation* 5 (June 1998), pp. 256–62. DOI: 10.1107/S0909049598000776.

[59] J. Manjarres et al. "Performances of Anode-resistive Micromegas for HL-LHC". In: *Journal of Instrumentation - J INSTRUM* 7 (Feb. 2012). DOI: 10.1088/1748-0221/7/03/C03040.

[60] Joost Melai et al. "A UV sensitive integrated Micromegas with Timepix readout". In: *Nuclear Instruments and Methods in Physics Research Section A: Accelerators, Spectrometers, Detectors and Associated Equipment* 628.1 (2011). VCI 2010, pp. 133–137. ISSN: 0168-9002. DOI: https://doi.org/10.1016/j.nima.2010.06.301. URL: https://www.sciencedirect.com/science/article/pii/S0168900210014919.

[61] Fabio Sauli. "The gas electron multiplier (GEM): Operating principles and applications". In: *Nuclear Instruments and Methods in Physics Research Section A: Accelerators, Spectrometers, Detectors and Associated Equipment* 805 (2016). Special Issue in memory of Glenn F. Knoll, pp. 2–24. ISSN: 0168-9002. DOI: https://doi.org/10.1016/j.nima.2015.07.060. URL: https://www.sciencedirect.com/science/article/pii/S0168900215008980.

[62] S Biswas et al. "Development of a GEM based detector for the CBM Muon Chamber (MUCH)". In: *Journal of Instrumentation* 8.12 (Dec. 2013), pp. C12002–C12002. DOI: 10.1088/1748-0221/8/12/c12002. URL: https://doi.org/10.1088/1748-0221/8/12/c12002.

[63] M.M. Aggarwal et al. "Particle identification studies with a full-size 4-GEM prototype for the ALICE TPC upgrade". In: *Nuclear Instruments and Methods in Physics Research Section A: Accelerators, Spectrometers, Detectors and Associated Equipment* 903 (2018), pp. 215–223. ISSN: 0168-9002. DOI: https://doi.org/10.1016/j.nima.2018.06.084. URL: https://www.sciencedirect.com/science/article/pii/S0168900218308222.

[64] R. Venditti. "Production and quality control of the new chambers with GEM technology in the CMS Muon System". In: *Nuclear Instruments and Methods in Physics Research Section A: Accelerators, Spectrometers, Detectors and Associated Equipment* 936 (2019). Frontier Detectors for Frontier Physics: 14th Pisa Meeting on Advanced Detectors, pp. 476–478. ISSN: 0168-9002. DOI: https://doi.org/10.1016/j.nima.2018.11.035. URL: https://www.sciencedirect.com/science/article/pii/S016890021831581X.

[65] B. Ketzer et al. “Performance of triple GEM tracking detectors in the COMPASS experiment”. In: *Nuclear Instruments and Methods in Physics Research Section A: Accelerators, Spectrometers, Detectors and Associated Equipment* 535.1 (2004). Proceedings of the 10th International Vienna Conference on Instrumentation, pp. 314–318. ISSN: 0168-9002. DOI: https://doi.org/10.1016/j.nima.2004.07.146. URL: https://www.sciencedirect.com/science/article/pii/S0168900204016687.

[66] Martin Klein and Christian J. Schmidt. “CASCADE, neutron detectors for highest count rates in combination with ASIC/FPGA based readout electronics”. In: *Nuclear Instruments and Methods in Physics Research Section A: Accelerators, Spectrometers, Detectors and Associated Equipment* 628.1 (2011). VCI 2010, pp. 9–18. ISSN: 0168-9002. DOI: https://doi.org/10.1016/j.nima.2010.06.278. URL: https://www.sciencedirect.com/science/article/pii/S0168900210014683.

[67] Jianjin Zhou et al. “A sealed ceramic GEM-based neutron detector”. In: *Nuclear Instruments and Methods in Physics Research Section A: Accelerators, Spectrometers, Detectors and Associated Equipment* 995 (2021), p. 165129. ISSN: 0168-9002. DOI: https://doi.org/10.1016/j.nima.2021.165129. URL: https://www.sciencedirect.com/science/article/pii/S0168900221001133.

[68] Kondo Gnanvo et al. “Imaging of high-Z material for nuclear contraband detection with a minimal prototype of a muon tomography station based on GEM detectors”. In: *Nuclear Instruments and Methods in Physics Research Section A: Accelerators, Spectrometers, Detectors and Associated Equipment* 652.1 (2011). Symposium on Radiation Measurements and Applications (SORMA) XII 2010, pp. 16–20. ISSN: 0168-9002. DOI: https://doi.org/10.1016/j.nima.2011.01.163. URL: https://www.sciencedirect.com/science/article/pii/S0168900211002658.

[69] Andrea Velásquez Moros and Héctor Fabio Castro Serrato. “Characterization and calibration of a triple-GEM detector for medical dosimetry”. In: *Nuclear Instruments and Methods in Physics Research Section A: Accelerators, Spectrometers, Detectors and Associated Equipment* 1000 (2021), p. 165241. ISSN: 0168-9002. DOI: https://doi.org/10.1016/j.nima.2021.165241. URL: https://www.sciencedirect.com/science/article/pii/S0168900221002254.

[70] W.R. Hendee and E.R. Ritenour. *Medical Imaging Physics*. Wiley, 2003. ISBN: 9780471461135. URL: https://books.google.com.br/books?id=55lh1B82SLsC.

[71] Susann Schmidt et al. “Low-temperature growth of boron carbide coatings by direct current magnetron sputtering and high-power impulse magnetron sputtering”. In: *Journal of Materials Science* 51.23 (Dec. 2016), pp. 10418–10428. ISSN: 1573-4803. DOI: 10.1007/s10853-016-0262-4. URL: https://doi.org/10.1007/s10853-016-0262-4.

[72] Carina Höglund et al. “Stability of 10B4C thin films under neutron radiation”. In: *Radiation Physics and Chemistry* 113 (2015), pp. 14–19. ISSN: 0969-806X. DOI: https://doi.org/10.1016/j.radphyschem.2015.04.006. URL: https://www.sciencedirect.com/science/article/pii/S0969806X15001449.

[73] Caroline A. Schneider, Wayne S. Rasband, and Kevin W. Eliceiri. “NIH Image to ImageJ: 25 years of image analysis”. In: *Nature Methods* 9.7 (July 2012), pp. 671–675. ISSN: 1548-7105. DOI: 10.1038/nmeth.2089. URL: https://doi.org/10.1038/nmeth.2089.

[74] Carina Höglund et al. “B4C thin films for neutron detection”. In: *Journal of Applied Physics* 111.10 (2012), p. 104908. DOI: 10.1063/1.4718573. eprint: https://doi.org/10.1063/1.4718573. URL: https://doi.org/10.1063/1.4718573.

[75] Carina Höglund et al. “Stability of 10B4C thin films under neutron radiation”. In: *Radiation Physics and Chemistry* 113 (2015), pp. 14–19. ISSN: 0969-806X. DOI: https://doi.org/10.1016/j.radphyschem.2015.04.006. URL: https://www.sciencedirect.com/science/article/pii/S0969806X15001449.

[76] Susann Schmidt et al. “Low-temperature growth of boron carbide coatings by direct current magnetron sputtering and high-power impulse magnetron sputtering”. In: *Journal of Materials Science* 51.23 (Dec. 2016), pp. 10418–10428. ISSN: 1573-4803. DOI: 10.1007/s10853-016-0262-4. URL: https://doi.org/10.1007/s10853-016-0262-4.

[77] J Hubbell and Stephen Seltzer. *Tables of X-Ray Mass Attenuation Coefficients and Mass Energy-Absorption Coefficients 1 keV to 20 MeV for Elements Z = 1 to 92 and 48 Additional Substances of Dosimetric Interest*. en. 1995-01-01 1995.

[78] P. Gasik et al. “Charge density as a driving factor of discharge formation in GEM-based detectors”. In: *Nuclear Instruments and Methods in Physics Research Section A: Accelerators, Spectrometers, Detectors and Associated Equipment* 870 (2017), pp. 116–122. ISSN: 0168-9002. DOI: https://doi.org/10.1016/j.nima.2017.07.042. URL: https://www.sciencedirect.com/science/article/pii/S0168900217307878.

[79] Geovane Grossi Araújo de Souza and Pedro Hugo Ferreira Natal da Luz. “Sistema de imagem de fluorescência de raios-X baseado em detectores Thick-GEM”. MA thesis. Universidade de São Paulo, 2019. DOI: https://doi.org/10.11606/D.43.2019.tde-21032019-233121.

[80] A Bressan et al. “Two-dimensional readout of GEM detectors”. In: *Nuclear Instruments and Methods in Physics Research Section A: Accelerators, Spectrometers, Detectors and Associated Equipment* 425.1 (1999), pp. 254–261. ISSN: 0168-9002. DOI: https://doi.org/10.1016/S0168-9002(98)01405-3. URL: https://www.sciencedirect.com/science/article/pii/S0168900298014053.

[81] Fabio Sauli. "The gas electron multiplier (GEM): Operating principles and applications". In: *Nuclear Instruments and Methods in Physics Research Section A: Accelerators, Spectrometers, Detectors and Associated Equipment* 805 (2016). Special Issue in memory of Glenn F. Knoll, pp. 2–24. ISSN: 0168-9002. DOI: https://doi.org/10.1016/j.nima.2015.07.060. URL: https://www.sciencedirect.com/science/article/pii/S0168900215008980.

[82] Geovane G.A. de Souza and Hugo Natal da Luz. "XRF element localization with a triple GEM detector using resistive charge division". In: *Nuclear Instruments and Methods in Physics Research Section A: Accelerators, Spectrometers, Detectors and Associated Equipment* 937 (2019), pp. 141–147. ISSN: 0168-9002. DOI: https://doi.org/10.1016/j.nima.2019.05.058. URL: https://www.sciencedirect.com/science/article/pii/S0168900219307144.

[83] Pedro Hugo Ferreira Natal da Luz. "Development of neutron and X-ray imaging detectors based on MHSP". PhD thesis. Universidade de Aveiro, 2009.

[84] Rita Joana da Cruz Roque. "X-ray imaging using 100 μm thick Gas Electron Multipliers operating in Kr-CO2 mixtures". MA thesis. Universidade de Coimbra, 2018.

[85] L. A. S. Filho. *Construção de sistema de controle de qualidade de estruturas do tipo thick-GEM*. Tech. rep. Scientific Iniciation Final Report, FAPESP, 2017.

[86] L. A. S. Filho et al. "Double-GEM based thermal neutron detector prototype". In: *Journal of Instrumentation* (2017).

[87] *CAMAC Model 7164(H) PEAK ADC Manual*. Phillips Scientific.

[88] Eduardo Maprelian et al. "Total and partial loss of coolant experiments in an instrumented fuel assembly of IEA-R1 research reactor". In: *Nuclear Engineering and Design* 363 (2020), p. 110610. ISSN: 0029-5493. DOI: https://doi.org/10.1016/j.nucengdes.2020.110610. URL: https://www.sciencedirect.com/science/article/pii/S0029549318307301.

[89] C.B.R. Parente et al. "Aurora—A high-resolution powder diffractometer installed on the IEA-R1 research reactor at IPEN-CNEN/SP". In: *Nuclear Instruments and Methods in Physics Research Section A: Accelerators, Spectrometers, Detectors and Associated Equipment* 622.3 (2010), pp. 678–684. ISSN: 0168-9002. DOI: https://doi.org/10.1016/j.nima.2010.06.203. URL: http://www.sciencedirect.com/science/article/pii/S0168900210013938.

[90] *Research reactor*. URL: https://www.britannica.com/technology/research-reactor#/media/1/499039/160853.

[91] Eduardo Yoshio Toyoda. "Evolução das doses no ambiente do Reator IEA-R1 e tendências com base nos resultados atuais". MA thesis. Universidade de São Paulo, 2016. DOI: http://dx.doi.org/10.11606/D.85.2016.tde-07062016-091546.

[92] J. R. Maiorino. “The utilization and operational experience of IEA-R1 Brazilian research reactor”. In: Research reactor utilization, safety and management Proceedings. SPECIFIC NUCLEAR REACTORS AND ASSOCIATED PLANTS. International Atomic Energy Agency (IAEA), 2000, CD–ROM. URL: http://inis.iaea.org/search/search.aspx?orig_q=RN:31043003.

[93] S. Agostinelli et al. “Geant4—a simulation toolkit”. In: *Nuclear Instruments and Methods in Physics Research Section A: Accelerators, Spectrometers, Detectors and Associated Equipment* 506.3 (July 2003), pp. 250–303. ISSN: 0168-9002. DOI: 10.1016/S0168-9002(03)01368-8.

[94] Geant4 Collaboration. *Geant 4 - Physics Reference Manual*. 10.7. Rev. 5.0. Geant4 Collaboration. Dec. 2020. URL: https://geant4-userdoc.web.cern.ch/UsersGuides/PhysicsReferenceManual/html/index.html.

[95] M. M. M. Paulino, M. G. Munhoz, and R. F. dos Santos. “Simulation of Particle Detector Performance”. XLIII Reunião de Trabalho sobre Física Nuclear no Brasil. 2020. URL: https://sec.sbfisica.org.br/eventos/rtfnb/xliii/sys/resumos/R0005-1.pdf.

[96] M. Moralles R. F. Santos M. G. Munhoz. “Performance and optimization simulations of a GEM-based neutron detector”. XLIII Reunião de Trabalho sobre Física Nuclear no Brasil. 2020. URL: https://sec.sbfisica.org.br/eventos/rtfnb/xliii/sys/resumos/R0085-1.pdf.

[97] S. Roy et al. “Stability study of gain and energy resolution for GEM detector”. In: *Nuclear Instruments and Methods in Physics Research Section A: Accelerators, Spectrometers, Detectors and Associated Equipment* 936 (2019). Frontier Detectors for Frontier Physics: 14th Pisa Meeting on Advanced Detectors, pp. 485–487. ISSN: 0168-9002. DOI: https://doi.org/10.1016/j.nima.2018.10.060. URL: https://www.sciencedirect.com/science/article/pii/S0168900218313743.

[98] M.C. Altunbas et al. “Aging measurements with the Gas Electron Multiplier (GEM)”. In: *Nuclear Instruments and Methods in Physics Research Section A: Accelerators, Spectrometers, Detectors and Associated Equipment* 515.1 (2003). Proceedings of the International Workshop on Aging Phenomena in Gaseous Detectors, pp. 249–254. ISSN: 0168-9002. DOI: https://doi.org/10.1016/j.nima.2003.09.006. URL: https://www.sciencedirect.com/science/article/pii/S016890020302477X.

[99] Z.K. Silagadze. “A new algorithm for automatic photopeak searches”. In: *Nuclear Instruments and Methods in Physics Research Section A: Accelerators, Spectrometers, Detectors and Associated Equipment* 376.3 (1996), pp. 451–454. ISSN: 0168-9002. DOI: https://doi.org/10.1016/0168-9002(96)00230-6. URL: https://www.sciencedirect.com/science/article/pii/0168900296002306.

[100] Miroslav Morháč et al. “Identification of peaks in multidimensional coincidence gamma-ray spectra”. In: *Nuclear Instruments and Methods in Physics Research Section A: Accelerators, Spectrometers, Detectors and Associated Equipment* 443.1 (2000), pp. 108–125. ISSN: 0168-9002. DOI: https://doi.org/10.1016/S0168-9002(99)01005-0. URL: https://www.sciencedirect.com/science/article/pii/S0168900299010050.

[101] M.A. Mariscotti. “A method for automatic identification of peaks in the presence of background and its application to spectrum analysis”. In: *Nuclear Instruments and Methods* 50.2 (1967), pp. 309–320. ISSN: 0029-554X. DOI: https://doi.org/10.1016/0029-554X(67)90058-4. URL: https://www.sciencedirect.com/science/article/pii/0029554X67900584.

[102] R. Brun and F. Rademakers. “ROOT: An object oriented data analysis framework”. In: *Nucl. Instrum. Meth. A* 389 (1997). Ed. by M. Werlen and D. Perret-Gallix, pp. 81–86. DOI: 10.1016/S0168-9002(97)00048-X.

[103] Eric W. Weisstein. *Erf. From MathWorld—A Wolfram Web Resource*. Last visited on 20/11/2021. URL: https://mathworld.wolfram.com/Erf.html.

[104] S Martoiu et al. “Development of the scalable readout system for micro-pattern gas detectors and other applications”. In: *Journal of Instrumentation* 8.03 (Mar. 2013), pp. C03015–C03015. DOI: 10.1088/1748-0221/8/03/c03015. URL: https://doi.org/10.1088/1748-0221/8/03/c03015.

[105] H. Fenker et al. “BoNus: Development and use of a radial TPC using cylindrical GEMs”. In: *Nuclear Instruments and Methods in Physics Research Section A: Accelerators, Spectrometers, Detectors and Associated Equipment* 592.3 (2008), pp. 273–286. ISSN: 0168-9002. DOI: https://doi.org/10.1016/j.nima.2008.04.047. URL: https://www.sciencedirect.com/science/article/pii/S0168900208006700.

[106] B. Flierl et al. “TPC-like readout for thermal neutron detection using a GEM-detector”. In: *Nuclear Instruments and Methods in Physics Research Section A: Accelerators, Spectrometers, Detectors and Associated Equipment* 824 (2016). Frontier Detectors for Frontier Physics: Proceedings of the 13th Pisa Meeting on Advanced Detectors, pp. 528–531. ISSN: 0168-9002. DOI: https://doi.org/10.1016/j.nima.2015.11.094. URL: https://www.sciencedirect.com/science/article/pii/S0168900215014680.